Modelling the contact-line dynamics of an evaporating drop

Matthew Saxton

Jesus College

University of Oxford

A thesis submitted for the degree of

Doctor of Philosophy

Trinity 2016

Acknowledgements

I would like to thank my supervisors Professor James Oliver, Professor Jonathan Whiteley, and Professor Dominic Vella for their help and guidance throughout my D.Phil studies. I am also grateful to Professor I. David Abrahams, Professor S. Jon Chapman, Professor Pierre Colinet, Professor Peter D. Howell, Dr Erqiang Li, Professor Sigurdur D. Thoroddsen, and Professor John S. Wettlaufer for useful discussions relating to this work. This work was funded by the Engineering and Physical Sciences Research Council (EPSRC).

Abstract

We study the evolution of a thin, axisymmetric, partially wetting drop as it evaporates. The effects of viscous dissipation, capillarity, slip, gravity, surface-tension gradients, and contact-angle hysteresis are taken into account in the regime in which the transport of vapour is dominated by diffusion. We find a criterion for when the contact-set radius close to extinction evolves as the square-root of the time remaining until extinction — the famous d^2-law. However, for a sufficiently large rate of evaporation, our analysis predicts that a '$d^{13/7}$-law' is more appropriate. We also determine how each of the physical effects in our model influences the evolution of the drop and hence its extinction time. Our asymptotic results are validated by comparison with numerical simulations.

We then revisit our model for the vapour phase and take kinetic effects into account through a linear constitutive law that states that the mass flux through the drop surface is proportional to the difference between the vapour concentration in equilibrium and that at the interface. We perform a local analysis near the contact line to investigate the way in which kinetic effects regularize the mass-flux singularity at the contact line. The problem is further analysed via a matched asymptotic analysis in the physically relevant regime in which the kinetic timescale is much smaller than the diffusive one. We find that the effect of kinetics is limited to an inner region near the contact line, in which kinetic effects enter at leading order and cause the vapour concentration at the free surface to deviate from its equilibrium value. We also derive an explicit expression for the mass flux through the free surface of the drop.

Contents

1 Introduction **1**

1.1 Motivation 1

1.2 The d^2-law 2

1.3 Literature review 2

1.3.1 Modelling mass transfer 3

1.3.2 Contact-line motion in the absence of mass transfer 6

1.3.3 Contact-line motion with mass transfer 7

1.4 Outline 9

1.5 Statement of authorship 9

2 Theoretical Formulation **11**

2.1 Dimensional governing equations 11

2.1.1 Thin-film equation 11

2.1.2 Surface tension 14

2.1.3 Mass flux 15

2.2 Non-dimensionalization 16

2.2.1 Timescales 16

2.2.2 Dimensionless model 17

2.3 Local analysis 19

2.A Finite-element simulations 21

3 When is the d^2-law valid? **23**

3.1 Motivation 23

3.2 Three timescales 24

3.3 Timescale of capillary action 24

3.3.1 Asymptotic structure 24

3.3.2 Outer region 24

3.3.3 Inner region 26

3.3.4 Intermediate region and matching 29
3.4 Timescale of contact-line motion 30
3.5 Timescale of mass loss 34
3.6 Small-$\mathcal{E}$ sub-limit 37
3.7 Comparison to numerical results 39
3.8 Extinction time of the drop 40
3.9 Summary 43
3.A Details of the inner region 44
3.A.1 Local and far-field analysis 45
3.A.2 Numerical solution of the boundary-value problem 45
3.A.3 Small-$\mathcal{E}$ limit 46
3.A.4 Large-$\mathcal{E}$ limit 46

4 The effects of gravity, surface-tension gradients, and contact-angle hysteresis 50
4.1 Motivation 50
4.2 Temporal and spatial asymptotic structure 50
4.3 Timescale of capillary action 51
4.3.1 Outer region 51
4.3.2 Inner region 57
4.3.3 Intermediate region and matching 58
4.3.4 Three evolution regimes 58
4.4 Timescale of contact-line motion 61
4.5 Timescale of mass loss 63
4.5.1 Outer region 63
4.5.2 Evolution on the timescale of mass loss 68
4.6 Comparison to finite-element simulations 71
4.7 Dependence of s_e, T_d, and T_e on parameters 73
4.8 Behaviour close to extinction 76
4.8.1 $\mathrm{Bo}, \mathrm{Ma}, \mathcal{E} = \mathrm{O}(1)$ 76
4.8.2 $\mathrm{Bo}, \mathrm{Ma}, \mathcal{E} \ll 1$ 76
4.9 Summary 77
4.A Numerical solution of the boundary-value problems for $\overline{\theta}(\mathcal{B}, \mathcal{M})$ and $\overline{V}(\mathcal{B}, \mathcal{M})$ 80
4.B Asymptotic analysis of the mass-loss boundary-value problem 81
4.B.1 $\mathcal{B} \to \infty$ with $\mathcal{M} = \mathrm{O}(1)$ 81

4.B.2 $\mathcal{M} \to \infty$ with $\mathcal{B} = \mathrm{O}(1)$ 81
4.B.3 $\mathcal{B}, \mathcal{M} \to \infty$ with $\mathcal{M}/\mathcal{B}^{1/2} = \mathrm{O}(1)$ 83
4.B.4 Implications for the timescale of contact-line motion 86

5 Kinetic effects regularize the mass-flux singularity 88
5.1 Motivation 88
5.2 Formulation 88
5.3 Local analysis near the contact line 91
5.3.1 Lens model 91
5.3.2 Kinetics-based model 92
5.3.3 Thick drops 93
5.4 Explicit expression for the evaporation rate 94
5.4.1 Solution of the mixed-boundary-value problem 94
5.4.2 Computing the evaporation rate 95
5.5 Asymptotic analysis in the limit of large kinetic Péclet number 98
5.5.1 Outer region 98
5.5.2 Inner region 98
5.5.2.1 The leading-order-inner problem 98
5.5.2.2 Regularized inner problem 99
5.5.2.3 Wiener-Hopf method 102
5.5.2.4 Inversion to find the inner evaporation rate 104
5.5.3 Conclusions from the matched-asymptotic analysis 105
5.5.4 Validation of asymptotic results 106
5.6 Summary 108
5.7 The liquid phase 110
5.7.1 Formulation 110
5.7.2 Local analysis 110
5.7.3 Evolution of the drop 111
5.A Evaporation rate at the contact line 112
5.B Details of the Wiener-Hopf calculation 113
5.B.1 An Abelian Theorem 113
5.B.2 Wiener-Hopf product factorization 114
5.B.3 Inversion to find $C(X, Y)$ 115

6 Discussion **117**
6.1 Summary 117
6.2 Future work 118
6.2.1 Major questions 118
6.2.2 Additional questions 119

References **122**

Chapter 1

Introduction

1.1 Motivation

The evaporation of a sessile liquid drop has many important practical applications in areas including biomedicine, geophysics, and industry. Such applications include DNA mapping and gene-expression analysis, the water cycle, and the manufacturing of semiconductor and micro-fluidic devices (Bonn *et al.*, 2009; Cazabat and Guéna, 2010; Erbil, 2012; Myers, 1998; Oron *et al.*, 1997; Plawsky *et al.*, 2008; Poulard *et al.*, 2003; Sefiane *et al.*, 2008; Semenov *et al.*, 2014). In many of these applications, the extinction time of the drop (*i.e.* the time at which the drop has fully evaporated) is a key quantity of interest.

Modelling mass transfer from a liquid drop or film that wets a solid substrate is a complicated problem because one must consider the transport of mass, momentum, and energy within and between three phases: the solid substrate, the liquid, and the surrounding atmosphere. If the contact line (where the solid, liquid, and gas phases all meet) is allowed to move, the problem is complicated further since the usual no-slip boundary condition at the solid–liquid boundary is incompatible with the kinematic boundary condition at the liquid–vapour interface.

The literature is largely lacking the simplifications and insights that would be gained from a systematic asymptotic analysis. Indeed, Murisic and Kondic (2011) state that "*Future work should include much more careful treatment of evaporation next to the contact line in the presence of a vapour/inert gas mixture. New asymptotic methods will also need to be developed to connect the nano-scale of relevance to the contact line physics and the macro-scale of a drop*". In this thesis, we shall apply a systematic asymptotic analysis to the problem of an evaporating drop with a moving contact line with the aim of gaining an understanding of the dynamics that determine the dynamics of the drop's evolution, and thus its extinction time.

1.2 The d^2-law

Experimental studies (Cachile *et al.*, 2002; Poulard *et al.*, 2003) have found that, for various liquids, the drop is axisymmetric with a circular contact set whose radius near to extinction is approximately proportional to the square-root of the time remaining until extinction. In other words, the time remaining until extinction is proportional to the square of the diameter d of the circular contact set (between the drop and the substrate). This 'd^2-law' may therefore be used to determine the extinction time of a very small drop.

The d^2-law is usually attributed to diffusion-limited kinetics (Erbil *et al.*, 2002) and may be understood using a scaling argument as follows. We assume that the timescale of mass loss is much longer than the timescale of spreading in the absence of mass transfer. We also assume that the microscopic contact angle is constant. A sufficiently small drop will then quickly relax under surface tension to have a constant-curvature profile with a macroscopic contact angle equal to the microscopic contact angle. After this initial transient, on a longer timescale, the drop will lose mass. Assuming that the mass loss is sufficiently small that it does not affect the droplet profile established on the spreading timescale, the volume of the drop scales with d^3. For a diffusion-dominated model (such as the lens model), the typical vertical scale over which the concentration of vapour decays is the same as the typical radial scale, namely d, because this decay is governed by Laplace's equation. For a thin drop, the local flux of vapour out of the drop, which is proportional to the normal derivative of the vapour concentration, then scales with $1/d$ (Ledesma-Aguilar *et al.*, 2014), so that the total mass flux out of the drop (obtained by integrating the local flux over the drop surface) scales linearly with d (Deegan *et al.*, 2000). Equating the rate of change of the drop volume with the total mass flux out of the drop therefore gives us the d^2-law.

Near-extinction behaviour differing slightly from the d^2-law has also been observed (Shahidzadeh-Bonn *et al.*, 2006). However, it is not clear whether such behaviour is systematic, or an artefact of experiment. An objective of this thesis will be to answer the question of when the d^2-law is valid.

1.3 Literature review

In this section, we begin by presenting a brief review of the most relevant literature on modelling mass transfer from a liquid drop or film that wets a solid substrate.

We shall then move on to discuss the separate problem of contact-line motion in the absence of the mass transfer. Finally, we review the literature on the combination of these two problems: the contact-line motion of an evaporating drop. Particular attention will be paid to how gravity, surface-tension gradients, and contact-angle hysteresis affect the problem.

1.3.1 Modelling mass transfer

Models involving a 'full' treatment of both the liquid and gas phases, *i.e.* the Navier-Stokes and energy equations for the density, pressure, velocity, and temperature fields, are often referred to as 'two-sided' models (Dondlinger *et al.*, 2005; Margerit *et al.*, 2005). To make analytical progress, it is necessary to simplify such a model.

One way to obtain a simpler model is to assume that the gas phase has a negligible influence on the evaporative flux so that we may concentrate solely on the liquid phase. Such models are often referred to as 'one-sided' models (Burelbach *et al.*, 1988; Cazabat and Guéna, 2010; Murisic and Kondic, 2011). A particular one-sided model that is often used in the literature is the non-equilibrium one-sided (NEOS) model (Cazabat and Guéna, 2010; Murisic and Kondic, 2011). The NEOS model is based on the assumption that the liquid–gas interface is not at equilibrium and that evaporation is limited by the transfer of molecules across the interface or the conduction of heat through the drop or substrate. The mass flux E^* across the interface per unit area per unit time in the NEOS model has the form

$$E^* \propto \frac{1}{h^* + K}, \tag{1.1}$$

where h^* is the drop thickness and K is a constant. The NEOS model is usually appropriate for the case when the gas phase consists purely of the liquid vapour. Cazabat and Guéna (2010) noted that the NEOS model may also be appropriate for water drops evaporating into an inert gas; the water–gas interface is susceptible to contamination (so that transfer of molecules across the interface is the rate-limiting step).

If the gas phase is assumed to be composed of a mixture of the liquid vapour and an inert gas (such as air), the following simplification of the two-sided model is available. If the gas phase is convection-free and its density, viscosity, and thermal conductivity are small compared to those of the liquid phase, it is possible to reduce the dynamics of the gas phase to a diffusion equation for the vapour concentration. Such models are often referred to as '1.5-sided' models (Dondlinger *et al.*, 2005; Haut

and Colinet, 2005; Margerit *et al.*, 2005; Sultan *et al.*, 2005). In these models, the transport of vapour is coupled to the Navier-Stokes equations within the liquid via appropriate boundary conditions (Oron *et al.*, 1997).

A 1.5-sided model may be simplified by assuming that the timescale of interest is much longer than that of diffusive vapour transport; the diffusion equation for the vapour then reduces to Laplace's equation. If the liquid–gas interface in the 1.5-sided model is assumed to be at equilibrium, then the boundary-value problem for the vapour concentration is mathematically equivalent to that of determining the electrical potential around a lens-shaped conductor; such models are therefore often referred to as 'lens' models in the literature (Cazabat and Guéna, 2010; Murisic and Kondic, 2011). The assumptions leading to the lens model imply that the process limiting evaporation is the diffusion of vapour away from the liquid–gas interface. The equivalent electrostatic problem has been solved by Deegan *et al.* (2000) and Popov (2005); Hu and Larson (2002) showed that an approximation for the resulting mass flux per unit area per unit time has the form

$$E^* \propto \frac{1}{(s^{*2} - r^{*2})^a}, \quad a = \frac{1}{2} - \frac{\Psi}{\pi}, \quad \text{for } 0 < \Psi < \frac{\pi}{2}, \tag{1.2}$$

where s^* is the radius of the circular contact set, r^* is the distance from the axis of symmetry of the drop, and Ψ is the microscopic contact angle. Upon making the lubrication approximation for the liquid drop, this expression reduces to

$$E^* \propto \frac{1}{(s^{*2} - r^{*2})^{1/2}}. \tag{1.3}$$

In fact, as we shall see in chapter 2, the mass flux in the thin-film limit may be found exactly, and has the form (1.3). The expression (1.3) is common in the literature (Deegan *et al.*, 1997, 2000). There is an inverse-square-root singularity at the contact line, but since this singularity is integrable, the total mass flux out of the drop is not singular and physically reasonable predictions for the evolution of the drop volume are obtained even without regularization of the evaporative singularity (Deegan *et al.*, 2000). The lens model is usually appropriate for a gas phase that is a mixture of the liquid vapour and an inert gas (with the notable exception of water, as already discussed).

Although the mass flux (1.3) is integrable, the divergence is still undesirable as it leads to a divergent velocity at the contact line, which is unphysical. One way to regularize the mass-flux singularity at the contact line in the lens model is to apply Kelvin's equation on the liquid–gas interface; this takes into account the variation in

vapour pressure due to the curvature of the interface (Skinner and Sambles, 1972). This approach has been used to model the evaporation of liquid drops in the presence of an ultra-thin precursor film that wets the substrate ahead of the drop (Cachile *et al.*, 2002; Eggers and Pismen, 2010). In the bulk of the drop (away from the contact line) the dominant term in a linearized version of Kelvin's equation is independent of the drop thickness. As a result, in an outer region away from the contact line, a constant vapour concentration is prescribed on the liquid–gas interface and the mass flux appears to have a singularity at the contact line (Eggers and Pismen, 2010). This singularity is in fact regularized in an inner region in the vicinity of the contact line, in which the other terms in Kelvin's equation become important (Morris, 2001; Rednikov and Colinet, 2013). In problems with a moving contact line, this evaporation model has the significant advantage that it also regularizes the stress singularity at the contact line (Janeček *et al.*, 2013; Rednikov and Colinet, 2013). Another advantage is the compatibility of the model with a precursor film. A model based on the Kelvin effect has the complexity that the mass flux depends on the liquid film thickness, so that the vapour transport problem is coupled to the liquid flow problem. However, it is reasonable to neglect the Kelvin effect when the curvature of the drop profile in the vicinity of the contact line is small.

If the gas phase surrounding the drop instead consists of its vapour only (and no inert gas), an alternative constitutive law to apply on the liquid–gas interface is the Hertz-Knudsen relation, derived from the kinetic theory of gases (Cercignani, 2000). The Hertz-Knudsen relation states that the mass flux across the drop surface per unit area per unit time is proportional to the difference between the equilibrium vapour density and the density of the vapour immediately above the drop. Formulated in terms of the vapour concentration (rather than the vapour density), on the free surface of the drop we have

$$E^* = M v_k (c_e - c^*), \tag{1.4}$$

where M is the molar mass of the liquid vapour, v_k is a typical kinetic velocity (which we define formally in chapter 5), c_e is the equilibrium vapour concentration, and c^* is the vapour concentration at the interface. It is immediately apparent from the expression (1.4) that, provided the vapour concentration c^* is finite, the mass flux is non-singular. The Hertz-Knudsen relation, or modified versions formulated in terms of vapour pressure, density, or temperature, have previously been used to model the evaporation of thin films (Prosperetti and Plesset, 1984), vapour bubbles in microchannels (Ajaev and Homsy, 2001), and droplet evaporation on a precursor film (Ajaev, 2005). A major advantage of the Hertz-Knudsen relation is that if the

equilibrium vapour concentration is assumed to be constant then, in the thin-film limit, the vapour transport problem depends on the liquid flow solely through the geometry of the contact set (instead of through the drop thickness as in the case of the Kelvin regularization mentioned above). While the assumptions required to derive the Hertz-Knudsen relation are not strictly satisfied when an inert gas is present, there is some experimental evidence that the Hertz-Knudsen relation is valid in such situations (Preston, 1933). A possible explanation for this is that immediately above the drop, the gas phase is almost entirely vapour. It may therefore be reasonable to use the Hertz-Knudsen relation to model evaporation into an inert gas (Janeček *et al.*, 2015; Sultan *et al.*, 2005).

1.3.2 Contact-line motion in the absence of mass transfer

The incompatibility between the usual no-slip boundary condition on the solid–liquid boundary and the kinematic boundary condition at the liquid–vapour interface results in a stress singularity at a moving contact line (Huh and Scriven, 1971). There are various approaches that regularize the stress singularity whilst remaining compatible with a continuum approach (Snoeijer and Andreotti, 2013). Remarkably, for small values of the regularization parameter, the choice of regularization does not affect the leading-order relationship between the macroscopic and microscopic contact angles (King, 2001). We discuss here two of the most commonly used approaches: precursor films and a finite slip length.

The first approach assumes that the liquid has an ultra-thin 'precursor film' that wets the substrate ahead of the contact line (Brochard-Wyart *et al.*, 1991; Colinet and Rednikov, 2011; de Gennes, 1985; Hervet and de Gennes, 1984). A disjoining pressure provides the physical mechanism for the formation of such a layer and for the prescription of an effective microscopic contact angle. This approach essentially removes the contact line, and in so doing regularizes the stress singularity. It is also advantageous since it is easily implemented in numerical simulations; the computational domain can be truncated at a finite distance from the drop, where the precursor film does not feel the effects of the drop. Finally, there is experimental evidence that such films exist in at least some parameter regimes (Bascom *et al.*, 1963; Iwamoto and Tanaka, 2002).

An alternative approach is to resolve the incompatibility between the no-slip and kinematic boundary conditions by allowing some slip on the solid surface. A commonly used slip law is the Navier slip law (Hocking, 1976; Voinov, 1976). This states that the tangential velocity vanishes at some small depth (the slip length) within the

substrate, with the component of the liquid velocity at the solid-liquid boundary that is tangential to the substrate is being proportional to the shear stress. It has been shown that the flow over a rough surface is equivalent to flow over a smooth surface with slip; the effective slip length is then given by the wavelength of the corrugations of the rough surface (Hocking, 1976). It is therefore plausible that the molecular effects governing contact-line motion have a macroscopic effect that can be modelled by a continuum model in which the slip length is on the molecular scale (Hocking and Rivers, 1982). While being based on hypothesis, rather than experimental observation, slip regularizations do have the advantage that the asymptotic structure in the small-slip limit is usually simpler than that of the small-precursor-thickness limit (in part because there is no extra 'precursor region'). Another advantage of the slip regularization is that the contact line is well-defined (a precursor regularization, on the other hand, essentially removes the contact line).

The effects of gravity on the spreading of a thin drop in the absence of mass transfer have been considered by Hocking (1983). In the limit of small slip, there is an exact solution for the leading-order drop profile in terms of modified Bessel functions. This is a modification to the classical spherical-cap profile that is seen when capillarity dominates.

1.3.3 Contact-line motion with mass transfer

We now consider the motion of a partially wetting drop as it evaporates. The focus of most theoretical efforts has been numerical simulations in the thin-film regime (Ajaev, 2005; Anderson and Davis, 1995; Dunn *et al.*, 2008, 2009c; Fried and Jabbour, 2012; Hocking, 1995; Murisic and Kondic, 2008; Poulard *et al.*, 2005; Sáenz *et al.*, 2015; Semenov *et al.*, 2014; Sodtke *et al.*, 2007). In the absence of evaporation, asymptotic approaches have been extremely fruitful (Hocking, 1983; Lacey, 1982), leading in particular to a systematic derivation of Tanner's law, and some asymptotic analysis has been carried out on mass-transfer models incorporating simple physics (Oliver *et al.*, 2015; Savva *et al.*, 2014).

Assuming that the drop loses mass on a longer timescale than that on which contact-line motion occurs, we expect the effect of gravity on the early-time evolution of an evaporating drop to be the same as in the absence of mass transfer (described earlier). However, the drop gets smaller as it loses mass, and we expect the effects of gravity to be unimportant for small drops. We therefore expect gravity to have little influence on the behaviour of the drop close to extinction.

Surface-tension gradients (as a result of variations in temperature) are another physical effect that may modify the drop profile from the constant-mean-curvature shape expected if capillarity dominates. Such gradients are usually caused by temperature variations within the drop and are thought to be an important factor for many liquids. The effect of surface-tension gradients on the shape of an evaporating drop has been studied recently by Tsoumpas *et al.* (2015) for a diffusion-dominated evaporation model. It was found experimentally, and confirmed using a lubrication model, that surface-tension gradients cause the drop profile to deviate from the classic spherical-cap profile; Marangoni forces pull liquid from the contact line to the centre of the drop to give it an inflated appearance. We note that, since the term in the thin-film equation due to surface-tension gradients depends on the mass flux, it is expected that the choice of constitutive law for the mass flux may be crucial in determining the qualitative effect of surface-tension gradients.

Contact-angle hysteresis is thought to play an important role in the evaporation of a drop (see, for example, Picknett and Bexon, 1977; Guéna *et al.*, 2007; Cazabat and Guéna, 2010; Murisic and Kondic, 2011; Stauber *et al.*, 2014, 2015). A simple model for contact-angle hysteresis is proposed by Hocking (1981) for contact-line motion in the absence of mass transfer. In this hysteresis model, the drop has a constant receding microscopic contact angle smaller than its (constant) advancing microscopic contact angle, with the microscopic contact angle taking an intermediate value if the contact line is pinned. The question of how the extinction time of an axisymmetric drop (not necessarily thin) is affected by contact-angle hysteresis has been considered by Stauber *et al.* (2014, 2015). In that work, it is assumed that capillarity causes the drop profile to be a spherical cap, with the initial profile parametrized by the initial contact angle. The evolution of the drop is assumed to be affected by contact-angle hysteresis and diffusion-dominated vapour transport. Provided that the initial contact angle is greater than the receding one, the drop evaporates in a 'stick-slide' mode: there is an initial 'constant contact radius' mode in which the drop is pinned and the contact angle decreases to the receding value, followed by a 'constant contact angle' mode in which the contact angle remains equal to its receding value and the contact-set radius decreases monotonically to zero. These two modes are common in the literature (Picknett and Bexon, 1977; Guéna *et al.*, 2007; Cazabat and Guéna, 2010; Murisic and Kondic, 2011). If the initial contact angle is smaller than the receding one, the drop simply evaporates in the constant-contact-angle mode. Assuming that the motion consists of a single constant-contact-radius mode, followed by a single

constant-contact-angle mode (Stauber *et al.*, 2014), the extinction time is given by a sum of two terms that correspond to the time spent in the two modes.

1.4 Outline

In chapter 2, we formulate and non-dimensionalize a thin-film model for an axisymmetric evaporating drop, taking into account the effects of viscous dissipation, capillarity, slip, diffusion-dominated vapour transport, gravity, surface-tension gradients, and contact-angle hysteresis.

In chapter 3, we find a criterion for when the scaling argument leading to the d^2-law is valid. We shall also determine what scaling behaviour is valid near extinction when this criterion is not satisfied. To accomplish this, we apply a systematic asymptotic analysis, in the limit of small slip, to a simplified version of our model (in which gravity, surface-tension gradients, and contact-angle hysteresis are neglected).

In chapter 4, we extend the analysis of chapter 3 to the full model (in which gravity, surface-tension gradients, and contact-angle hysteresis are taken into account). The focus of the analysis of chapter 4 is to gain an understanding of the dynamics that govern the evolution of the drop profile and determine its extinction time.

In chapter 5, we replace the lens evaporation model used in chapters 2–4 with a linear, kinetics-based constitutive law for the mass flux across the liquid–gas interface, inspired by the Hertz-Knudsen relation (1.4); we assume that the equilibrium vapour concentration is constant. We will have two main goals. The first is to investigate the way in which kinetic effects regularize the mass-flux singularity at the contact line. The second is to derive an explicit expression for the evaporation rate; in principle, this enables the analysis of chapters 3 and 4 to be carried out for the kinetics-based evaporation model (although we do not perform such an analysis in this thesis).

In chapter 6, we summarize our results and outline directions for future work.

1.5 Statement of authorship

The content of this thesis is based on three papers. At time of writing, the first is published (Saxton *et al.*, 2016c), the second is under revision (Saxton *et al.*, 2016a), and the third is in preparation (Saxton *et al.*, 2016b). The author of this thesis is the first author of these three papers, which he co-authored with his supervisors Prof. James Oliver, Prof. Jonathan Whiteley, and Prof. Dominic Vella. Some of the numerical codes used in this thesis were written by Prof. Oliver or Prof. Whiteley;

appropriate authorship is cited where used. In addition, figure 3.1 and the figures used in chapter 4, with the exception of figure 4.7, were generated by Prof. Oliver. All other work herein is that of the author of this thesis.

Chapter 2

Theoretical Formulation

2.1 Dimensional governing equations

2.1.1 Thin-film equation

We introduce cylindrical polar coordinates (r^*, z^*) measuring the radial distance from the line of symmetry of the axisymmetric drop and the normal distance from the substrate, respectively (here and hereafter, starred variables denote dimensional quantities). The free surface of the drop is denoted by $z^* = h^*(r^*, t^*)$, where t^* is time. The liquid occupies the region $0 < z^* < h^*(r^*, t^*)$ for $0 < r^* < s^*(t^*)$, so that $r^* = s^*(t^*)$ is the location of the contact line (where the drop thickness vanishes). The drop thickness profile $h^*(r^*, t^*)$ and contact-set radius $s^*(t^*)$ are not known *a priori* — their determination is a major goal of our analysis. A definition sketch is given in figure 2.1.

We assume that the liquid is incompressible with a constant density ρ and that its motion is governed by the Stokes equations with a constant viscosity μ and a constant acceleration due to gravity g (the values of the physical parameters used in the model are given for various liquids in table 2.1). The receding microscopic contact angle Ψ_R between the free boundary and substrate is assumed to be constant and small. The initial drop profile is assumed to be smooth with a small aspect ratio of the order of Ψ_R. To leading order in Ψ_R, the radial and normal velocity components, u^* and w^* respectively, and the pressure field p^* then satisfy the lubrication equations, given by

$$\frac{1}{r^*}\frac{\partial}{\partial r^*}(r^* u^*) + \frac{\partial w^*}{\partial z^*} = 0, \quad \frac{\partial p^*}{\partial r^*} = \mu \frac{\partial^2 u^*}{\partial z^{*2}}, \quad \frac{\partial p^*}{\partial z^*} = -\rho g, \qquad (2.1a - c)$$

for $0 < z^* < h^*(r^*, t^*)$, $0 < r^* < s^*(t^*)$.

The liquid is assumed to slip on the substrate according to a generalized Navier slip law with slip length $\Lambda^{3-n}(h^*)^{n-2}$, with Λ and n constant parameters (with Λ

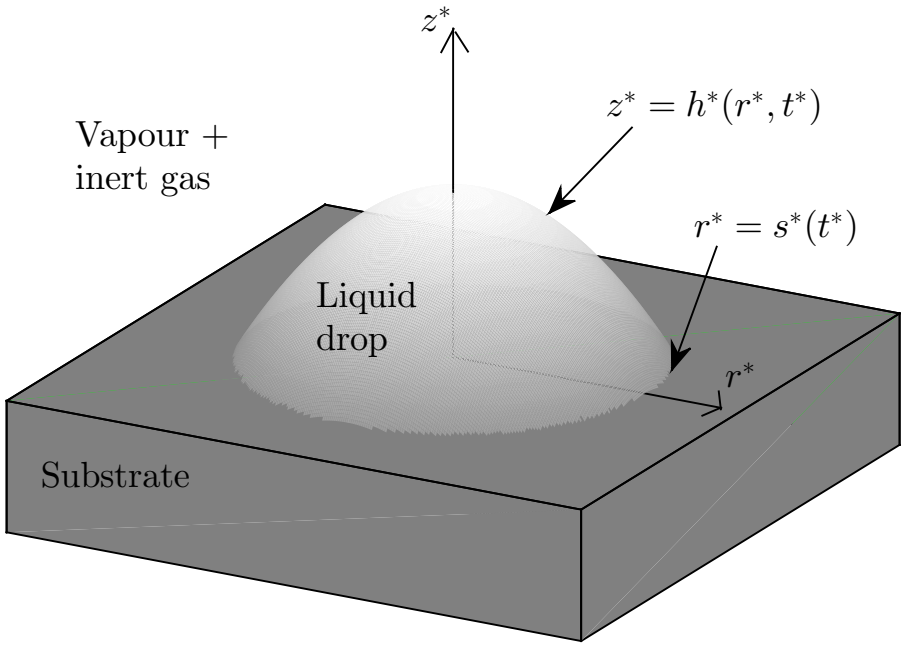

Figure 2.1: Definition sketch. Cylindrical polar coordinates (r^*, z^*) measure the radial distance from the axis of symmetry of the drop and the normal distance from the substrate, respectively. The contact line is located at $r^* = s^*(t^*)$ and the free surface of the drop is at $z^* = h^*(r^*, t^*)$, where t^* is time.

		Hexane	Isopropanol	HFE-7100
γ_s	$(\mathrm{mN\,m^{-1}})$	17.89	20.93	13.6
μ	$(\mathrm{mPa\,s})$	0.300	2.038	0.61
ρ	$(\mathrm{kg\,m^{-3}})$	656	790	1482
D	$(\mathrm{cm^2\,s^{-1}})$	0.03	0.096	0.061
L_v	$(\mathrm{kJ\,kg^{-1}})$	322	790	112
M	$(\mathrm{g\,mol^{-1}})$	86.2	60.1	250
c_e	$(\mathrm{mol\,m^{-3}})$	0.02	2.2	10.9
k	$(\mathrm{W\,m^{-1}\,K^{-1}})$	0.12	0.135	0.069
v_k	$(\mathrm{m\,s^{-1}})$	67.6	81.0	28.1
$\lvert\mathrm{d}\gamma/\mathrm{d}T\rvert$	$(\mathrm{mN\,m^{-1}\,K^{-1}})$	0.102	0.25	0.096

Table 2.1: Values of the physical parameters used in the model for hexane, isopropanol and HFE-7100 at 25°C and 1 atm (Lide, 2004; Murisic and Kondic, 2011; Sultan *et al.*, 2005; Tsoumpas *et al.*, 2015). In order to estimate γ_s, we assume that the solid substrate is held at a temperature $T_s = 25°\mathrm{C}$. The equilibrium vapour concentration c_e is evaluated using the saturation vapour pressure. The kinetic velocity v_k will be defined and used in chapter 5.

having the dimensions of length and n being dimensionless). We delay until later a discussion of which values of n are most physically relevant but note that our model will be shown to be correctly specified for $n < 5/2$. The substrate is assumed to be impermeable so that the slip and no-flux boundary conditions on the solid–liquid boundary are given by

$$u^* = \Lambda^{3-n}(h^*)^{n-2}\frac{\partial u^*}{\partial z^*}, \quad w^* = 0, \tag{2.2a, b}$$

on $z^* = 0$, $0 < r^* < s^*(t^*)$, respectively.

The traction on the free surface is assumed to be due to a surface tension $\gamma^*(r^*, t^*)$ only. We assume that the drop loses mass through its free boundary at a mass flux $E^*(r^*, t^*)$ per unit area per unit time. Expressions for the quantities γ^* and E^* will be derived shortly. Thus, to leading order in Ψ_R, the kinematic and dynamic boundary conditions at the liquid–vapour interface are given by

$$w^* = \frac{\partial h^*}{\partial t^*} + u^*\frac{\partial h^*}{\partial r^*} + \frac{E^*}{\rho}, \quad p^* = -\gamma^*\left(\frac{\partial^2 h^*}{\partial r^{*2}} + \frac{1}{r^*}\frac{\partial h^*}{\partial r^*}\right), \quad \mu\frac{\partial u^*}{\partial z^*} = \frac{\partial \gamma^*}{\partial r^*}, \tag{2.3$a-c$}$$

on $z^* = h^*(r^*, t^*)$, $0 < r^* < s^*(t^*)$.

The lubrication equations (2.1) and boundary conditions (2.2)–(2.3) lead in the usual way (Myers, 1998; Oron *et al.*, 1997) to the thin-film equation

$$\frac{\partial h^*}{\partial t^*} + \frac{1}{r^*}\frac{\partial}{\partial r^*}(r^* h^* \overline{u}^*) = -\frac{E^*}{\rho} \quad \text{for } 0 < r^* < s^*(t^*), \tag{2.4}$$

where the depth-averaged radial velocity $\overline{u}^*$ is given by

$$\overline{u}^* = \frac{1}{\mu}\left\{\left(\frac{h^{*2}}{3} + \Lambda^{3-n}(h^*)^{n-1}\right)\frac{\partial}{\partial r^*}\left[\gamma^*\left(\frac{\partial^2 h^*}{\partial r^{*2}} + \frac{1}{r^*}\frac{\partial h^*}{\partial r^*}\right) - \rho g h^*\right] + \left(\frac{h^*}{2} + \Lambda^{3-n}(h^*)^{n-2}\right)\frac{\partial \gamma^*}{\partial r^*}\right\} \tag{2.5}$$

for $0 < r^* < s^*(t^*)$.

2.1.2 Surface tension

We assume that the solid substrate is held at a constant temperature T_s and the surface tension γ^* depends on temperature T^* (of the liquid–gas interface) according to a linear equation of state, given by

$$\gamma^*(T^*) = \gamma_s - \left|\frac{\mathrm{d}\gamma}{\mathrm{d}T}\right|(T^* - T_s), \tag{2.6}$$

where $\gamma_s := \gamma^*(T_s)$, and the temperature derivative of the surface tension $\mathrm{d}\gamma/\mathrm{d}T$ is assumed to be constant. Dependence of the surface tension on pressure is assumed to be negligible, as in treatments of similar problems (Ajaev, 2005; Sultan *et al.*, 2005).

The temperature $T^*(r^*, z^*, t^*)$ of the liquid phase is assumed to be governed by an advection-diffusion equation with a constant thermal diffusivity. We further assume that the timescale of diffusive heat transport is much shorter than that of advective heat transport. Thus, to leading order in the thin-film limit, the temperature of the liquid phase is governed by

$$\frac{\partial^2 T^*}{\partial z^{*2}} = 0, \tag{2.7}$$

for $0 < z^* < h^*(r^*, t^*),\ 0 < r^* < s^*(t^*)$. The thermal conductivity of the gas phase is assumed to be much smaller than the thermal conductivity of the liquid phase. Thus, to leading order in the thin-film limit, boundary conditions on the temperature of the liquid phase are given by

$$T^* = T_s \text{ on } z^* = 0; \quad -k\frac{\partial T^*}{\partial z^*} = L_v E^* \text{ on } z^* = h^*(r^*, t^*), \tag{2.8a, b}$$

for $0 < r^* < s^*(t^*)$, where k is the thermal conductivity of the liquid and L_v is the latent heat of vaporization per unit mass of liquid, both of which are assumed to be constant. We deduce from (2.7) and (2.8) that the temperature of the liquid phase is given by

$$T^*(r^*, z^*, t^*) = T_s - \frac{L_v}{k}E^*(r^*, t^*)z^*. \tag{2.9}$$

We deduce from the equation of state (2.6) and the expression for the temperature of the liquid phase (2.9) that the surface tension γ^* of the liquid–gas interface is given by

$$\gamma^* = \gamma_s + \frac{L_v}{k}\left|\frac{\mathrm{d}\gamma}{\mathrm{d}T}\right| E^* h^*. \tag{2.10}$$

2.1.3 Mass flux

A mixture of liquid vapour and an inert gas occupies the region above the drop and substrate. We assume that the dynamics of the vapour may be reduced to a diffusion equation for the vapour concentration c^*, with constant diffusion coefficient D, given by

$$\frac{\partial c^*}{\partial t^*} = D\nabla^2 c^* \quad \text{for } z^* > 0; \tag{2.11}$$

we note that since the vertical extent of the drop is assumed to be much smaller than the radius of the circular contact set of the drop, and the latter is the relevant lengthscale for the transport of liquid vapour, the gas phase occupies the region $z^* > 0$ to leading order in Ψ_R.

The vapour just above the free surface of the drop is assumed to be at equilibrium and the equilibrium vapour concentration is assumed to take a constant value c_e. As the substrate is impermeable, there is no flux of vapour through the substrate. Thus, after linearizing the boundary condition on the surface of the drop onto $z^* = 0$, we obtain to leading order in Ψ_R the mixed boundary conditions

$$c^* = c_e \quad \text{on } z^* = 0,\ 0 < r^* < s^*(t^*); \quad \frac{\partial c^*}{\partial z^*} = 0 \quad \text{on } z^* = 0,\ r^* > s^*(t^*). \tag{2.12a, b}$$

We assume that the vapour concentration in the far field takes a constant value c_∞, so that

$$c^* \to c_\infty \quad \text{as } r^{*2} + z^{*2} \to \infty,\ z^* > 0. \tag{2.13}$$

The mass flux $E^*(r^*, t^*)$ through the liquid–gas interface per unit area per unit time is given in terms of the solution to the mixed-boundary-value problem (2.11)–(2.13) by

$$E^*(r^*, t^*) = -DM\left.\frac{\partial c^*}{\partial z^*}\right|_{z^*=0} \quad \text{for } 0 < r^* < s^*(t^*), \tag{2.14}$$

where M is the molar mass of the liquid vapour.

If we assume that the timescale of vapour diffusion is much smaller than the shortest timescale on which mass loss becomes relevant, then the vapour transport equation (2.11) reduces to Laplace's equation and the mixed-boundary-value problem (2.11)–(2.13) for the vapour concentration is mathematically equivalent to that of

finding the electric potential around an electrified disc charged to a uniform potential; the solution of this problem (Weber, 1873; Wiley and Webster, 1982) implies that the mass flux in this special case is given by

$$E^*(r^*, t^*) = \frac{2DM(c_e - c_\infty)}{\pi(s^{*2} - r^{*2})^{1/2}} \quad \text{for } 0 < r^* < s^*(t^*). \tag{2.15}$$

Such an inverse-square-root singularity in the evaporative flux is common in the literature (Deegan *et al.*, 1997, 2000).

A quantity of interest is the surface-integrated flux Q^* out of the drop per unit time, given by

$$Q^*(t^*) = 2\pi \int_0^{s^*(t^*)} r^* E^*(r^*, t^*)\, \mathrm{d}r^*. \tag{2.16}$$

The quantity Q^* is needed to determine the evolution of the volume of the drop and thus the extinction time (at which the drop volume vanishes), even in models that do not consider the detailed hydrodynamics of motion (Stauber *et al.*, 2014, 2015).

2.2 Non-dimensionalization

2.2.1 Timescales

We now identify some important timescales in the problem. We let R denote the initial radius of the circular contact set, *i.e.* $s^*(0) = R$. We also assume that capillary forces dominate gravity and Marangoni forces. Finally, we assume that vapour diffusion occurs on a much faster timescale than mass loss.

From a balance of terms in a diffusion equation governing vapour transport, we identify a typical timescale of vapour diffusion τ_D; a balance of the two terms on the left-hand side of the thin-film equation (2.4) identifies a typical timescale of capillary action τ_C; a balance of the first and last terms in the thin-film equation (2.4) identifies a typical timescale of global mass loss τ_M. These three timescales are given by

$$\tau_D = \frac{R^2}{D}, \quad \tau_C = \frac{3\mu R}{\Psi_R^3 \gamma_s}, \quad \tau_M = \frac{\pi \Psi_R \rho R^2}{2DM(c_e - c_\infty)}. \tag{2.17$a-c$}$$

The values of these timescales for drops of hexane, isopropanol and HFE-7100 with initial contact-set radii of 5mm, 0.5mm and 50μm are given in table 2.2.

We will non-dimensionalize the thin-film equation (2.4) on the timescale of capillary action. We therefore require $\tau_D \ll \tau_C$ for the expression (2.15) to hold; since $\tau_D/\tau_C \propto R$, this assumption is valid for sufficiently small drops (see table 2.2). For reasons discussed in chapter 6, much of the analysis in this thesis is valid even when this condition is not met, although details of the early-time evolution are different.

	R	τ_D (s)	τ_C (s)	τ_M (s)	τ_D/τ_C
Hexane	5mm	8.3	0.25	5.0×10^5	33
	0.5mm	0.083	0.025	5.0×10^3	3.3
	50μm	8.3×10^{-4}	2.5×10^{-3}	50	0.33
Isopropanol	5mm	2.6	1.5	2.4×10^3	1.8
	0.5mm	0.026	0.15	24	0.18
	50μm	2.6×10^{-4}	0.015	0.24	0.018
HFE-7100	5mm	4.1	0.67	89	6.1
	0.5mm	0.041	0.067	0.89	0.61
	50μm	4.1×10^{-4}	6.7×10^{-3}	8.9×10^{-3}	0.061

Table 2.2: Typical timescales of vapour diffusion τ_D, capillary action τ_C and mass loss τ_M for hexane, isopropanol and HFE-7100 for initial contact-set radii of 5mm, 0.5mm and 50μm. We also give the ratio τ_D/τ_C, which must be small for the expression (2.15) for the mass flux to be valid.

2.2.2 Dimensionless model

We non-dimensionalize by scaling $r^* = Rr$, $t^* = \tau_C t$, $s^* = Rs$ and $h^* = \Psi_R R h$. We obtain thereby the dimensionless thin-film equation

$$\frac{\partial h}{\partial t} + \frac{1}{r}\frac{\partial}{\partial r}(rh\overline{u}) = -\frac{\alpha}{(s^2 - r^2)^{1/2}} \quad \text{for } 0 < r < s(t), \tag{2.18}$$

where

$$\overline{u} = (h^2 + \lambda^{3-n}h^{n-1})\frac{\partial}{\partial r}\left(\frac{\partial^2 h}{\partial r^2} + \frac{1}{r}\frac{\partial h}{\partial r} - \mathrm{Bo}\, h\right) + \mathrm{Ma}\left(h + \frac{2}{3}\lambda^{3-n}h^{n-2}\right)\frac{\partial}{\partial r}\left(\frac{h}{(s^2 - r^2)^{1/2}}\right), \tag{2.19}$$

and non-dimensionalization has introduced four dimensionless parameters:

$$\alpha = \frac{\tau_C}{\tau_M}, \quad \lambda = \frac{3^{1/(3-n)}\Lambda}{\Psi_R R}, \quad \mathrm{Bo} = \frac{\rho g R^2}{\gamma_s}, \quad \mathrm{Ma} = \frac{3DM(c_e - c_\infty)L_v}{\pi\Psi_R\gamma_s k}\left|\frac{\mathrm{d}\gamma}{\mathrm{d}T}\right|. \tag{2.20a-d}$$

Here α is the ratio of the timescales of capillary action and mass loss, λ is the slip coefficient (the ratio between the slip length and the typical drop thickness), Bo is the Bond number (the ratio between gravity and capillary forces), and Ma is the Marangoni number (the ratio of Marangoni forces to capillary forces). The values of these parameters for drops of hexane, isopropanol and HFE-7100 with initial contact-set radii of 5mm, 0.5mm and 50μm are given in table 2.3. We note that the slip exponent n is also a dimensionless parameter. In chapter 3, we shall find that an

	R	α	λ	$\mathcal{E}$	Bo	Ma
Hexane	5mm	5.1×10^{-7}	3.0×10^{-5}	1.3×10^{-4}	9.0	7.6×10^{-4}
	0.5mm	5.1×10^{-6}	3.0×10^{-4}	4.1×10^{-4}	0.090	7.6×10^{-4}
	50μm	5.1×10^{-5}	3.0×10^{-3}	1.3×10^{-3}	9.0×10^{-4}	7.6×10^{-4}
Isopropanol	5mm	6.0×10^{-4}	3.0×10^{-5}	0.15	9.3	0.85
	0.5mm	6.0×10^{-3}	3.0×10^{-4}	0.49	0.093	0.85
	50μm	0.060	3.0×10^{-3}	1.5	9.3×10^{-4}	0.85
HFE-7100	5mm	7.6×10^{-3}	3.0×10^{-5}	2.0	27	7.2
	0.5mm	0.076	3.0×10^{-4}	6.2	0.27	7.2
	50μm	0.76	3.0×10^{-3}	20	2.7×10^{-3}	7.2

Table 2.3: The values of the dimensionless parameters α, λ, $\mathcal{E}$ (defined in (3.12)), Bo and Ma for hexane, isopropanol and HFE-7100 for initial contact-set radii of 5mm, 0.5mm and 50μm. We assume that the acceleration due to gravity is $g = 9.81\mathrm{m\,s^{-2}}$, the concentration of each vapour in the far field is $c_\infty = 0$, the temperature of the substrate is $T_s = 25°\mathrm{C}$, the receding microscopic contact angle is $\Psi_R = 0.1$, the slip exponent is $n = 2$ and the slip length is $\Lambda = 5\mathrm{nm}$ (typical slip lengths are in the range 1–10nm).

important combination of these parameters is given by $\mathcal{E} = 2^{1/2}\alpha/\lambda^{1/2}$; the physical significance of the dimensionless parameter $\mathcal{E}$ will be discussed later. From table 2.3, we see that in physically relevant scenarios, α and λ are both small, while $\mathcal{E}$, Bo and Ma may either be small or of order-unity size, but are not large.

The modelling assumptions above, together with the assumption that there is no flux of liquid through the contact line, imply that the pertinent boundary conditions for the thin-film equation (2.18) are given by

$$\frac{\partial h}{\partial r} = 0,\ rh\overline{u} = 0 \text{ at } r = 0; \quad h = 0,\ -\frac{\partial h}{\partial r} = \Psi,\ rh\overline{u} = 0 \text{ at } r = s(t)^-,\ (2.21a - e)$$

where Ψ is the (dimensionless) microscopic contact angle. We adopt the simple model for contact-angle hysteresis proposed by Hocking (1981) by imposing the constraints

$$\Psi = 1 \text{ for } \dot{s} < 0; \quad 1 \le \Psi \le 1 + \Psi_H \text{ for } \dot{s} = 0; \quad \Psi = 1 + \Psi_H \text{ for } \dot{s} > 0,\ (2.22a - c)$$

where $\dot{s} := \mathrm{d}s/\mathrm{d}t$. We refer to the parameter

$$\Psi_H = \frac{\Psi_A - \Psi_R}{\Psi_R} \tag{2.23}$$

as the contact-angle hysteresis, where Ψ_A is the (constant) advancing microscopic contact angle. The boundary conditions thus introduce one dimensionless parameter (Ψ_H) in addition to the five parameters in thin-film equation (2.18) and (2.19) (namely

α, λ, Bo, Ma and n). We also impose continuity on s when the contact line de-pins or becomes pinned.

We prescribe an initial drop profile

$$h(r,0) = \mathcal{H}(r) \quad \text{for } 0 \leq r \leq s(0) = 1, \tag{2.24}$$

where the function $\mathcal{H}(r)$ is chosen to be smooth and positive for $0 \leq r < 1$ and to satisfy the boundary conditions ($2.21a-e$). We also prescribe an initial microscopic contact angle $\Psi(0) = \Psi_*$.

Integrating the thin-film equation (2.18) from $r = 0$ to $r = s(t)$ and applying the no-flux boundary conditions ($2.21b, e$) implies that the expression representing global conservation of mass is given by

$$\frac{\mathrm{d}V}{\mathrm{d}t} = -2\pi\alpha s, \quad V(t) = 2\pi \int_0^{s(t)} rh(r,t)\,\mathrm{d}r. \tag{2.25}$$

Provided that the drop profile remains positive, $V(t)$ is the (dimensionless) volume of the drop at time t. The volume decreases monotonically with time t until it vanishes at some time $t = t_e$. We refer to t_e as the extinction time of the drop; a goal of this thesis is to determine the dependence of the extinction time on the dimensionless parameters in the model (namely α, λ, Bo, Ma, n and Ψ_H) and the initial condition (2.24) in the physically relevant distinguished limit in which $\alpha, \lambda \ll 1$ and $\mathrm{Bo}, \mathrm{Ma} = \mathrm{O}(1)$.

2.3 Local analysis

In this section, we check that the model (2.18), (2.19), (2.21) and (2.24) is correctly specified. To do this, we consider the local expansion of the drop thickness at each of the two boundaries of the domain and then check that the total number of degrees of freedom in these two expansions is equal to the order of the corresponding thin-film equation.

From (2.18), (2.19) and ($2.21a$,b), we deduce that the local expansion of the solution near the line of symmetry is

$$h \sim a_1 + a_2 r^2 \quad \text{as } r \to 0^+, \tag{2.26}$$

where $a_1(t)$ and $a_2(t)$ are degrees of freedom (in the sense that they are globally, rather than locally determined).

Near to the contact line a local analysis of (2.18) and (2.19) subject to the boundary conditions $(2.21c-e)$ in a frame moving with the contact line implies that $h \sim \Psi(s-r) + \widehat{h}$ as $r \to s^-$, with

$$-\frac{\mathrm{d}s}{\mathrm{d}t}\Psi(s-r) + \lambda^{3-n}\Psi^n(s-r)^n\left(\frac{\partial^3\widehat{h}}{\partial r^3} - \frac{\mathrm{Ma}}{2^{3/2}s^{1/2}(s-r)^{3/2}}\right) \sim \frac{2^{1/2}\alpha}{s^{1/2}}(s-r)^{1/2} + q(t), \tag{2.27}$$

as $r \to s(t)^-$, where $q(t)$ is the flux of liquid through the contact line and we have integrated once with respect to r. However, at this stage we have not yet applied the no-flux condition $(2.21e)$ to set $q = 0$ in order to make the following technical point: it follows from (2.27) that, for $2 \leq n < 5/2$, the local expansion for h can only be asymptotic (with $\widehat{h} = o(s-r)$ as $r \to s^-$) if $q = 0$; thus, the no-flux condition $(2.21e)$ is in fact redundant for $2 \leq n < 5/2$ and need only be imposed for $n < 2$. Setting $q = 0$ for all $n < 5/2$, we can now use (2.27) to deduce that the local expansion is given by

$$h \sim \Psi(s-r) + \begin{cases} c_1(s-r)^{3/2} + \ldots + a_3(s-r)^2 & \text{for } n < 2, \\ c_2(s-r)^{3/2} + \ldots + a_3(s-r)^2 & \text{for } n = 2, \\ c_3(s-r)^{7/2-n} + \ldots + a_3(s-r)^2 & \text{for } 2 < n < 5/2, \end{cases} \tag{2.28}$$

as $r \to s(t)^-$, where $a_3(t)$ is a degree of freedom and

$$\begin{aligned} c_1(t) &= \frac{2^{3/2}\mathrm{Ma}}{3s^{1/2}}, \quad c_2(t) = c_1 + \frac{2^{7/2}\alpha}{3s^{1/2}\lambda\Psi^2}, \\ c_3(t) &= \frac{2^{1/2}\alpha}{s^{1/2}\lambda^{3-n}\Psi^n(n-3/2)(5/2-n)(7/2-n)}. \end{aligned} \tag{2.29}$$

For the special case $\mathrm{Ma} = 0$, we find that (2.28) reduces to

$$h \sim \Psi(s-r) + \begin{cases} a_3(s-r)^2 + c_3(s-r)^{7/2-n} & \text{for } n < 3/2, \\ \left[c_4\log\left(1/(s-r)\right) + a_3\right](s-r)^2 & \text{for } n = 3/2, \\ c_3(s-r)^{7/2-n} + a_3(s-r)^2 & \text{for } 3/2 < n < 5/2, \end{cases} \tag{2.30}$$

as $r \to s(t)^-$, where

$$c_4(t) = \frac{2^{1/2}\alpha}{s^{1/2}\lambda^{3/2}\Psi^{3/2}}. \tag{2.31}$$

There are therefore a total of four degrees of freedom (namely $a_1(t)$, $a_2(t)$, $a_3(t)$ and either $\Psi(t)$ or $s(t)$) in the two expansions (2.26) and (2.28); the thin-film equation (2.18) is fourth-order. Thus, the model (2.18), (2.19), (2.21) and (2.24) is correctly specified with the microscopic contact angle $\Psi(t)$ being determined as part of the solution in regimes where the contact line is pinned and the contact-set radius $s(t)$ being determined as part of the solution in regimes in which the contact line is moving.

We note that the local expansion (2.28) implies that there is an inflection point in the drop profile for $\mathrm{Ma} > 0$, but this is not necessarily the case for $\mathrm{Ma} = 0$. These observations are consistent with experimental and theoretical observations made by Tsoumpas *et al.* (2015).

2.A Finite-element simulations

We may solve the full thin-film problem (2.18), (2.19), (2.21) and (2.24) numerically using a finite-element method. This finite-element code was written by Prof. Jonathan Whiteley. Such finite-element simulations are used to validate the asymptotic predictions that we make in chapters 3 and 4.

The contact set $0 < r < s(t)$ is mapped to a fixed computational domain $0 < \xi < 1$ by setting $r = s(t)\xi$. We also set $h(r,t) = \eta(\xi,t)/s(t)^2$ to enable the resulting thin-film equation to be written in conservative form. We obtain

$$\frac{\partial \eta}{\partial t} - \frac{1}{\xi}\frac{\partial Q}{\partial \xi} = -\frac{\alpha s}{\sqrt{1-\xi^2}}, \tag{2.32}$$

where the flux $Q(\xi,t)$ is given by

$$Q = \xi\left(\frac{\eta^3}{s^{10}} + \frac{\lambda^{3-n}\eta^n}{s^{2n+4}}\right)\frac{\partial P}{\partial \xi} - \mathrm{Ma}\,\xi\left(\frac{\eta^2}{s^7} + \frac{2\lambda^{3-n}\eta^{n-1}}{3s^{2n+1}}\right)\frac{\partial}{\partial \xi}\left(\frac{\eta}{\sqrt{1-\xi^2}}\right) + \frac{\xi^2\eta}{s}\frac{\mathrm{d}s}{\mathrm{d}t}, \tag{2.33}$$

and the pressure $P(\xi,t)$ is given by

$$P = -\left(\frac{\partial^2 \eta}{\partial \xi^2} + \frac{1}{\xi}\frac{\partial \eta}{\partial \xi}\right) + s^2\mathrm{Bo}\,\eta, \tag{2.34}$$

for $0 < \xi < 1$. The boundary conditions $(2.21a-e)$ give

$$\frac{\partial \eta}{\partial \xi} = 0,\ Q = 0 \text{ at } \xi = 0; \quad \eta = 0,\ -\frac{\partial \eta}{\partial \xi} = s^3\Psi,\ Q = 0 \text{ at } \xi = 1^-, \qquad (2.35a-e)$$

where we impose the constraints (2.22) on the microscopic contact angle Ψ. We use an initial condition of the form

$$\eta(\xi,0) = \mathcal{H}(\xi) = \frac{(6V_* - \pi\Psi_*)}{\pi}(1-\xi^2) + \frac{3(\pi\Psi_* - 4V_*)}{4\pi}(1-\xi^4) \quad \text{for } 0 \le \xi \le 1, \tag{2.36}$$

with $s(0) = 1$, $\Psi(0) = \Psi^*$, and V_* and Ψ_* chosen such that

$$1 \le \Psi_* \le 1 + \Psi_H, \quad V_* > \frac{\pi\Psi_*}{12}. \qquad (2.37a,b)$$

(The latter condition ensures that $\mathcal{H}(\xi) > 0$ for $0 \le \xi < 1$.)

At each time step, we solve the system (2.32)–(2.34) — treated as a system of two second-order partial differential equations for η and P — subject to the boundary conditions $(2.35a-c, e)$. If the contact line is moving, the remaining boundary condition $(2.35d)$ is used to determine the contact-set radius $s(t)$ implicitly, and the microscopic contact angle $\Psi(t)$ is given by (2.22). If the contact line is pinned, $s(t)$ is given by its value at the previous timestep, and the remaining boundary condition $(2.35d)$ is used to determine $\Psi(t)$ implicitly. The finite-element method used is implicit in time and uses a linear approximation of the solution on each element. The spatial grid is piecewise-uniform; the grid points are more densely packed close to the contact line in order to achieve the necessary resolution in that region. We check that our simulations have converged in the usual way by refining the spatial mesh and decreasing the time step.

Chapter 3

When is the d^2-law valid?

3.1 Motivation

In many experimental systems, it has been found that, close to extinction, the remaining extinction time of a drop is proportional to the square of its current diameter. This 'd^2-law' can be rationalized using diffusion-limited arguments, as outlined in chapter 1. Here, we seek to understand whether hydrodynamics modifies this picture — when is the d^2-law valid? To investigate this, we analyse a simplified version of the model derived in chapter 2. In particular, we neglect gravity, surface-tension gradients, and contact-angle hysteresis (*i.e.* $\mathrm{Bo} = \mathrm{Ma} = \Psi_H = 0$) so that the drop thickness $h(r,t)$ satisfies the thin-film equation

$$\frac{\partial h}{\partial t} + \frac{1}{r}\frac{\partial}{\partial r}(rh\overline{u}) = -\frac{\alpha}{(s^2 - r^2)^{1/2}} \quad \text{for } 0 < r < s(t), \tag{3.1}$$

where

$$\overline{u} = (h^2 + \lambda^{3-n}h^{n-1})\frac{\partial}{\partial r}\left[\frac{1}{r}\frac{\partial}{\partial r}\left(r\frac{\partial h}{\partial r}\right)\right]. \tag{3.2}$$

This is to be solved subject to the boundary conditions

$$\frac{\partial h}{\partial r} = 0,\ rh\overline{u} = 0 \text{ at } r = 0; \quad h = 0,\ -\frac{\partial h}{\partial r} = 1,\ rh\overline{u} = 0 \text{ at } r = s(t)^-, \quad (3.3a - e)$$

and the initial condition

$$h(r,0) = \mathcal{H}(r) \quad \text{for } 0 \le r \le s(0) = 1. \tag{3.4}$$

The content of this chapter is based heavily on Saxton *et al.* (2016c).

3.2 Three timescales

In practical scenarios, it is expected that the slip coefficient λ is small. We now perform an asymptotic analysis in the small-slip limit $\lambda \to 0$. We begin with the timescale of capillary action; we will see that on this timescale the contact line does not move and mass is conserved, both to leading order in λ. The drop profile will be shown to relax under surface tension from its prescribed initial condition to a profile with constant mean curvature (in the thin-film limit). Our analysis of the timescale of capillary action will identify a longer timescale on which the contact line moves an order-unity distance. On this longer timescale we will show that, provided the ratio α of the timescales of capillary action and mass loss satisfies $\alpha = \mathrm{O}(\lambda^{1/2})$ as $\lambda \to 0$, mass is still conserved to leading order. The drop either spreads or recedes under surface tension to an equilibrium leading-order contact-set radius that, loosely speaking, is determined by a balance of capillarity and mass loss in an inner region near the contact line (about which more shortly). On an even longer timescale, we show that the drop starts to lose an order-unity amount of mass and that the leading-order contact-set radius and leading-order drop volume decrease monotonically with time until the drop becomes extinct.

3.3 Timescale of capillary action

3.3.1 Asymptotic structure

The spatial asymptotic structure on the timescale of capillary action consists of an outer region in which $(s - r)$, $h = \mathrm{O}(1)$ as $\lambda \to 0$, and an inner region near the contact line in which slip becomes important. We see from the expression (3.2) for $\overline{u}$ that slip modifies the mobility of the liquid when $h = \mathrm{O}(\lambda)$. Since the (dimensionless) microscopic contact angle is 1, this must occur within a distance of $\mathrm{O}(\lambda)$ from the contact line. To match efficiently the contact angle between the outer and inner regions, we introduce an intermediate region, spanning all lengthscales between them. This spatial asymptotic structure is illustrated in figure 3.1.

3.3.2 Outer region

We see from the global conservation of mass expression (2.25) that, provided that $\alpha \ll 1$ as $\lambda \to 0$, mass loss occurs on a longer timescale than capillary action (we note that we shall in fact shortly make a more restrictive assumption on α, namely that $\alpha = \mathrm{O}(\lambda^{1/2})$ as $\lambda \to 0$). In the absence of mass transfer, it has been shown that the

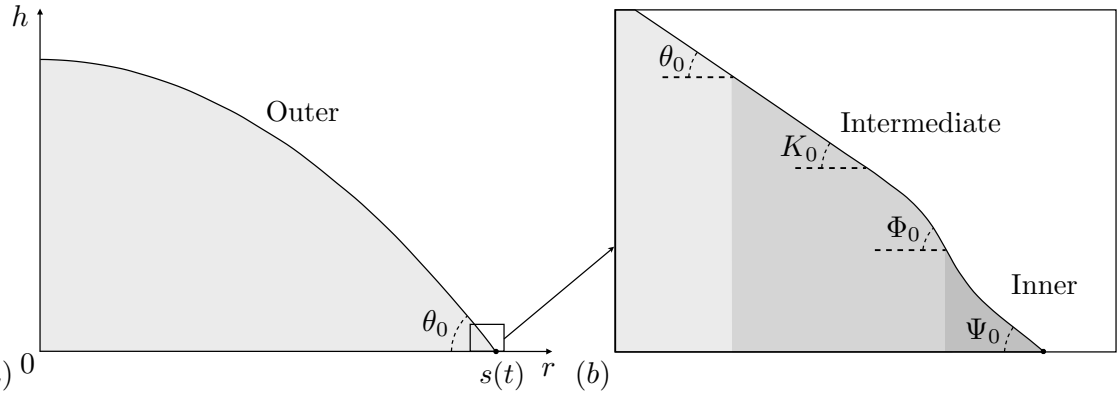

Figure 3.1: Asymptotic regions in the small-slip limit on the timescale of capillary action; θ_0, K_0, and Ψ_0 are the leading-order contact angles in the outer (macroscopic), intermediate (mesoscopic), and inner (microscopic) regions, respectively. In the absence of contact-angle hysteresis, $\Psi_0 = 1$. The remaining contact angle depicted, Φ_0, is the leading-order far-field microscopic contact angle, which plays the role of an effective microscopic contact angle in the leading-order contact-line law.

contact line moves an order-unity distance on a longer timescale $t = \mathrm{O}(\log(1/\lambda))$ as $\lambda \to 0$ (Hocking, 1983; Lacey, 1982). We therefore expand $h \sim h_0$, $s \sim 1 + s_1/\log(1/\lambda)$ as $\lambda \to 0$. In the outer region in which $(s - r)$, $h = \mathrm{O}(1)$, the evolution of the leading-order film profile $h_0(r, t)$ is governed by the thin-film equation given by

$$\frac{\partial h_0}{\partial t} + \frac{1}{r}\frac{\partial}{\partial r}(r h_0 \overline{u}_0) = 0, \quad \overline{u}_0 = h_0^2 \frac{\partial}{\partial r}\left[\frac{1}{r}\frac{\partial}{\partial r}\left(r\frac{\partial h_0}{\partial r}\right)\right] \quad \text{for } 0 < r < 1. \tag{3.5}$$

This is to be solved subject to the boundary conditions

$$\frac{\partial h_0}{\partial r} = 0, \ r h_0 \overline{u}_0 = 0 \text{ at } r = 0^+; \quad h_0 = 0, \ -\frac{\partial h_0}{\partial r} = \theta_0 \text{ at } r = 1^-, \qquad (3.6a - d)$$

where a degree-of-freedom count reveals that the leading-order macroscopic contact angle $\theta_0(t)$ is determined as part of the solution. The leading-order-outer problem is closed by the initial condition

$$h_0(r, 0) = \mathcal{H}(r) \quad \text{for } 0 \le r \le 1. \tag{3.7}$$

The boundary conditions $(3.6c, d)$ imply that there is no flux of liquid through the contact line (as described by, for example, (Oliver *et al.*, 2015) for the two-dimensional version of the problem). We then deduce that the global conservation of mass condition is given by

$$2\pi \int_0^1 r h_0(r, t)\, \mathrm{d}r = V_*, \tag{3.8}$$

where $V_* := V(0)$ is the initial (dimensionless) volume of the drop.

We note that (3.5)–(3.6) has a steady solution $h_0 = 2V_*(1-r^2)/\pi$, which has constant mean curvature (in the thin-film limit). We therefore postulate that this constant-curvature profile is a large-time attractor and that the correctly specified problem (3.5)–(3.7) governs the relaxation of the profile under surface tension from its prescribed initial value (3.7) to this state. We note that this is what happens in the numerical simulations of Oliver *et al.* (2015) for the analogous two-dimensional case in which the evaporation rate is uniform and of size $\mathrm{O}(1/\log(1/\lambda))$ as $\lambda \to 0$. We therefore expect the large-time attractors

$$h_0(r,t) \to \frac{2V_*}{\pi}(1-r^2), \quad \theta_0(t) \to \frac{4V_*}{\pi} \quad \text{as } t \to \infty. \tag{3.9}$$

We solve numerically the problem (3.5)–(3.7) using a finite-element code analogous to the one used to solve the full problem (described in appendix 2.A). We use a candidate initial condition of the form

$$\mathcal{H}(r) = \frac{(6V_*-\pi)}{\pi}(1-r^2) + \frac{3(\pi-4V_*)}{4\pi}(1-r^4) \quad \text{for } 0 \le r \le 1. \tag{3.10}$$

The initial condition (3.10) satisfies the boundary conditions $(3.3a-e)$ but requires $V_* > \pi/12$ to ensure that the initial profile is positive throughout $0 \le r < 1$. We note that even for moderate values of $(V_* - \pi/4)$ (including the value $V_* = 1$ used in the majority of our simulations), the initial condition (3.10) is significantly different from a parabola.

Our numerical simulations suggest that (3.9) is indeed the global attractor for sufficiently smooth initial profiles $\mathcal{H}$ satisfying the boundary conditions (3.3). For example, we plot the numerical predictions for the leading-order drop profile $h_0(r,t)$ and the leading-order macroscopic contact angle $\theta_0(t)$ in figure 3.2 alongside the theoretically predicted large-time attractors (3.9) for $V_* = 1$ and $V_* = 0.4$. We see that both solutions converge to the large-time attractor (3.9), but with the relaxation being much slower for the case $V_* = 0.4$ (where the prescribed initial condition is further from a parabola).

3.3.3 Inner region

In the inner region of size $\mathrm{O}(\lambda)$ near the contact line, we set $h = \lambda H$, $r = s - \lambda X$ and expand $H \sim H_0$, $s \sim 1 + s_1/\log(1/\lambda)$ as $\lambda \to 0$. Integrating the resulting leading-order thin-film equation once with respect to X and applying the condition of no flux of liquid through the contact line gives

$$(H_0^3 + H_0^n)\frac{\partial^3 H_0}{\partial X^3} = -\mathcal{E}X^{1/2} \quad \text{for } X > 0, \tag{3.11}$$

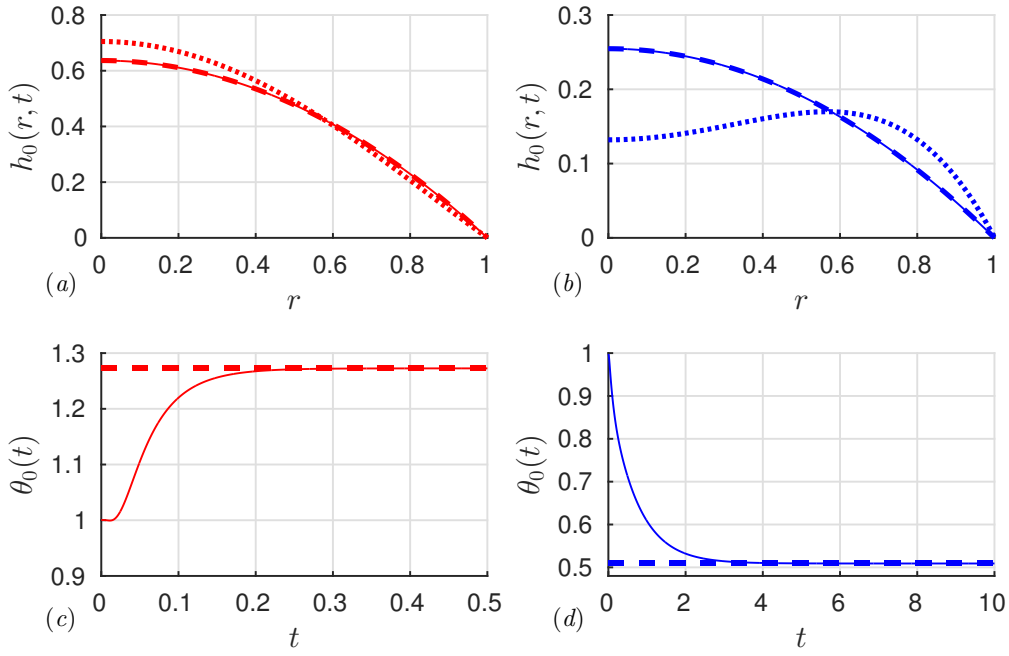

Figure 3.2: The drop profile $h_0(r,t)$ as a function of r for (a) $V_* = 1$ and (b) $V_* = 0.4$. The dotted curves are the prescribed initial conditions (3.10); we see that the initial condition for $V_* = 0.4$ is much further from a parabola than the initial condition for $V_* = 1$. The dashed curves are the predicted large-time attractors (3.9) and the solid curves are the numerical solution at time $t = 10$ of the leading-order-outer problem (3.5)–(3.7); we see that the numerical solution is in excellent agreement with the theoretically predicted large-time attractors (3.9) at this time. We also plot the leading-order macroscopic contact angle $\theta_0(t)$ as a function of t for (c) $V_* = 1$ and (d) $V_* = 0.4$. The dashed lines are the predicted large-time attractors (3.9) and the solid curves are the results of numerical simulations.

where the dimensionless parameter $\mathcal{E}$ is given by

$$\mathcal{E} = \frac{2^{1/2}\alpha}{\lambda^{1/2}} = \frac{2^{3/2}3^{(5/2-n)/(3-n)}\mu DM(c_e - c_\infty)}{\pi \Psi_R^{7/2}\Lambda_0^{1/2}\gamma_S \rho R^{1/2}}; \tag{3.12}$$

we note that $\mathcal{E}$ may be viewed as a capillary number based on the liquid velocity induced by the evaporative flux in the inner region. For brevity, we shall hereafter refer to this evaporation-induced capillary number $\mathcal{E}$ as the evaporation rate. The thin-film equation (3.11) is to be solved subject to the conditions

$$H_0 = 0, \quad \frac{\partial H_0}{\partial X} = 1 \quad \text{at } X = 0^+; \quad \frac{\partial H_0}{\partial X} \to \Phi_0(\mathcal{E}, n) \quad \text{as } X \to \infty, \tag{3.13}$$

where Φ_0 is the leading-order far-field microscopic contact angle.

The balance of all terms in the leading-order-inner equation (3.11) tells us that there is a distinguished limit when $\mathcal{E} = \mathrm{O}(1)$ as $\lambda \to 0$: if $\mathcal{E} \ll 1$ as $\lambda \to 0$, the leading-order problem on the timescale of capillary action will be the same as if there were no mass transfer. This suggests that the d^2-law will be valid if α is such that $\mathcal{E} \ll 1$ as $\lambda \to 0$. To test whether the d^2-law breaks down when this condition does not hold, we analyse the distinguished limit $\mathcal{E} = \mathrm{O}(1)$ as $\lambda \to 0$ and shall find that a different close-to-extinction scaling behaviour emerges. (We also check that in the sub-limit $\mathcal{E} \to 0$, the d^2-law is recovered.) The values of $\mathcal{E}$ for several liquids were shown in table 2.3. We see that the distinguished limit $\mathcal{E} = \mathrm{O}(1)$ as $\lambda \to 0$ is the physically relevant one for some liquids, but that $\mathcal{E} \ll 1$ as $\lambda \to 0$ for others (provided these liquids satisfy the other modelling assumptions).

In appendix 3.A we show that Φ_0 is a degree of freedom belonging to the leading-order-inner problem given by (3.11) and (3.13). We also describe how the dependence of Φ_0 on $\mathcal{E}$ is determined numerically for $n = 1$ and $n = 2$, and we derive the asymptotes

$$\Phi_0(\mathcal{E}, n) \sim 1 + \Phi_{01}(n)\mathcal{E} \quad \text{as } \mathcal{E} \to 0, \tag{3.14}$$

$$\Phi_0(\mathcal{E}, n) \sim \Phi_\infty(n)\mathcal{E}^{2/7} \quad \text{as } \mathcal{E} \to \infty, \tag{3.15}$$

where $\Phi_{01}(1) = \pi/\sqrt{2}$, $\Phi_{01}(2) = \pi$, $\Phi_\infty(1) \approx 1.750$, and $\Phi_\infty(2) \approx 1.939$ (the last two quantities being determined numerically as described in appendix 3.A). We plot the numerical solution of the boundary-value problem (3.11) and (3.13) for Φ_0 as a function of $\mathcal{E}$ for $n = 1$ and $n = 2$ in figure 3.3. We also plot the small-$\mathcal{E}$ and large-$\mathcal{E}$ asymptotes to Φ_0, (3.14) and (3.15) respectively. We see excellent agreement between the numerical solution of the boundary-value problem and the asymptotes in the expected range of validity.

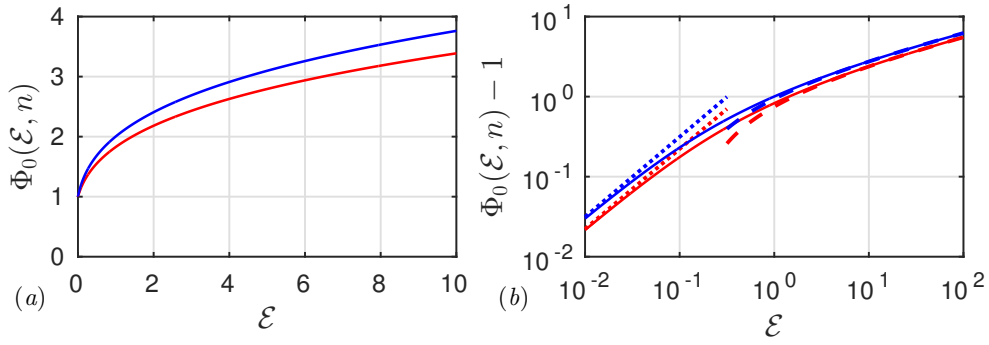

Figure 3.3: (a) Dependence of the leading-order far-field microscopic contact angle $\Phi_0(\mathcal{E}, n)$ on the evaporation rate $\mathcal{E}$ for $n = 1$ (red curve) and $n = 2$ (blue curve). In (b) we plot $(\Phi_0 - 1)$ together with the small-$\mathcal{E}$ asymptotes (dotted lines) and large-$\mathcal{E}$ asymptotes (dashed curves), (3.14) and (3.15), respectively.

We note that Φ_0 is a monotone-increasing function of the evaporation rate $\mathcal{E}$; loosely speaking, the evaporative singularity pulls the contact line toward the liquid in a manner that increases with the evaporation rate (in the sense that the drop profile is thicker in the inner region for a larger evaporation rate). We also note that the leading-order far-field microscopic contact angle $\Phi_0(\mathcal{E}, n)$ takes similar values for $n = 1$ and $n = 2$, and we find that for each of these values it may be approximated to within 1% by

$$\Phi_0(\mathcal{E}, n) \approx [1 + \Phi_\infty(n)^{7/2}\mathcal{E}]^{2/7}; \tag{3.16}$$

however, we do not use this approximation in the sequel.

3.3.4 Intermediate region and matching

In the intermediate region, we follow, for example, (Hocking, 1983; Oliver *et al.*, 2015) by setting $h = (s - r)K(\xi, t)$, $(s - r) = \lambda^{(1-\xi)}$ and expanding $K \sim K_0$, $s \sim 1 + s_1/\log(1/\lambda)$ as $\lambda \to 0$ with $\xi = \mathrm{O}(1)$, $0 < \xi < 1$. We find that, since $\alpha = \mathrm{O}(\lambda^{1/2})$ as $\lambda \to 0$,

$$\frac{\partial h}{\partial t} \sim -\frac{K_0}{\log(1/\lambda)}\frac{\mathrm{d}s_1}{\mathrm{d}t}, \quad \frac{1}{r}\frac{\partial}{\partial r}(rh\overline{u}) \sim \frac{K_0^3}{\log(1/\lambda)}\frac{\partial K_0}{\partial \xi}, \quad \frac{\alpha}{(s^2 - r^2)^{1/2}} = \mathrm{O}(\lambda^{\xi/2}), \tag{3.17}$$

as $\lambda \to 0$ with $\xi = \mathrm{O}(1)$, $0 < \xi < 1$. Thus, the leading-order mesoscopic contact angle $K_0(\xi, t)$ satisfies the equation

$$K_0^2\frac{\partial K_0}{\partial \xi} = \frac{\mathrm{d}s_1}{\mathrm{d}t} \quad \text{for } 0 < \xi < 1. \tag{3.18}$$

Matching with the outer region (as $\xi \to 1^-$) and the inner region (as $\xi \to 0^+$) reveals that (3.18) is to be solved subject to the conditions

$$K_0(0,t) = \Phi_0(\mathcal{E}, n), \quad K_0(1,t) = \theta_0(t). \tag{3.19}$$

We deduce immediately from the consistency condition for the leading-order-intermediate problem (3.18) and (3.19) that the asymptote for the contact-line law as $\lambda \to 0$ is given by

$$\frac{\mathrm{d}s}{\mathrm{d}t} \sim \frac{1}{\log(1/\lambda)} \frac{\mathrm{d}s_1}{\mathrm{d}t} = \frac{\theta_0(t)^3 - \Phi_0(\mathcal{E}, n)^3}{3\log(1/\lambda)} \quad \text{as } \lambda \to 0. \tag{3.20}$$

This tells us that the contact line moves an order-unity distance on a longer timescale, $t = \mathrm{O}(\log(1/\lambda))$ as $\lambda \to 0$, just as in the cases of no mass transfer (Hocking, 1983; Lacey, 1982) and uniform mass transfer of size $\mathrm{O}(1/\log(1/\lambda))$ as $\lambda \to 0$ (Oliver *et al.*, 2015).

Equation (3.20) may also be compared to Tanner's law for the spreading of a drop in the absence of mass loss, namely that

$$v(t) \propto \theta(t)^3 - 1, \tag{3.21}$$

where $v(t)$ is the contact-line velocity and $\theta(t)$ is the macroscopic contact angle. Having identified the timescale of contact-line motion as $t = \mathrm{O}(\log(1/\lambda))$ as $\lambda \to 0$, we see that the contact-line law (3.20) is the generalization of Tanner's law (3.21) with evaporation accounted for by replacing the microscopic contact angle with the leading-order far-field microscopic contact angle $\Phi_0(\mathcal{E}, n)$. We therefore identify Φ_0 as an effective microscopic contact angle and shall henceforth refer to it as such.

To summarize this section, on the timescale of capillary action $t = \mathrm{O}(1)$ as $\lambda \to 0$, mass is conserved and the contact line does not move, both to leading order. The leading-order drop profile relaxes under surface tension from its prescribed initial value to a steady-state profile with constant mean curvature (in the thin-film limit) and volume equal to the initial volume. Thus, the only information from the initial drop profile that is passed on to later timescales is the initial contact-set radius and volume.

3.4 Timescale of contact-line motion

The contact line begins to move an order-unity distance on the longer timescale $\widehat{t} = t/\log(1/\lambda) = \mathrm{O}(1)$ as $\lambda \to 0$. The spatial asymptotic structure is the same as

for the timescale of capillary action, though the details in each of the three regions are different, as we shall now describe. We begin with the outer region by expanding $h(r,t) \sim \widehat{h}_0(r,\widehat{t}\,)$ and $s(t) \sim \widehat{s}_0(\widehat{t}\,)$ as $\lambda \to 0$ to find that the leading-order-outer problem is quasi-steady with no mass loss. The solution is the constant-mean-curvature profile

$$\widehat{h}_0 = \frac{\widehat{\theta}_0}{2\widehat{s}_0}(\widehat{s}_0^2 - r^2) \quad \text{for } 0 < r < \widehat{s}_0, \tag{3.22}$$

where $\widehat{\theta}_0(\widehat{t}\,)$ is the leading-order macroscopic contact angle. We note that neither $\widehat{\theta}_0(\widehat{t}\,)$ nor the leading-order contact-set radius $\widehat{s}_0(\widehat{t}\,)$ are determined as part of the solution to the leading-order-outer problem. The first of the two pieces of information needed to determine these quantities comes from the leading-order version of the global conservation of mass condition (2.25). Matching with the timescale of capillary action tells us that the initial leading-order drop volume is V_*. Using the leading-order-outer solution (3.22), we find that, since $\alpha = \mathrm{O}(\lambda^{1/2})$ as $\lambda \to 0$, the conservation of mass condition (2.25) implies that

$$\frac{\pi\widehat{\theta}_0\widehat{s}_0^3}{4} = V_*. \tag{3.23}$$

This determines $\widehat{\theta}_0$ in terms of $\widehat{s}_0$, leaving us in need of an additional piece of information to determine $\widehat{s}_0$. We shall see that this additional piece of information is the condition for matching the contact angles between the outer and inner regions.

The leading-order-inner problem is the same as for the timescale of capillary action, namely (3.11) and (3.13), except that the evaporation rate $\mathcal{E}$ appearing on the right-hand side of the thin-film equation (3.11) is replaced by $\mathcal{E}/\widehat{s}_0^{1/2}$.

In the intermediate region, we set $(s - r) = \lambda^{(1-\xi)}$ and expand $h(r,t) \sim (\widehat{s}_0 - r)\widehat{K}_0(\xi,\widehat{t}\,)$, $s(t) \sim \widehat{s}_0(\widehat{t}\,)$ as $\lambda \to 0$ with $\xi = \mathrm{O}(1)$, $0 < \xi < 1$. We find that the leading-order mesoscopic contact angle $K_0(\xi,\widehat{t}\,)$ satisfies (3.18) and (3.19) but with $\mathrm{d}s_1/\mathrm{d}t$ and $\mathcal{E}$ replaced by $\mathrm{d}\widehat{s}_0/\mathrm{d}\widehat{t}$ and $\mathcal{E}/\widehat{s}_0^{1/2}$, respectively. We deduce immediately from the consistency condition for the resulting leading-order-intermediate problem that the leading-order contact-line law is

$$\frac{\mathrm{d}\widehat{s}_0}{\mathrm{d}\widehat{t}} = \frac{1}{3}\left[\left(\frac{4V_*}{\pi\widehat{s}_0^3}\right)^3 - \Phi_0\left(\frac{\mathcal{E}}{\widehat{s}_0^{1/2}}, n\right)^3\right]. \tag{3.24}$$

Here, we have substituted for $\widehat{\theta}_0$ from the conservation of mass constraint (3.23): on the timescale contact-line motion, the effective microscopic contact angle is given by $\Phi_0(\mathcal{E}/\widehat{s}_0^{1/2}, n)$.

We plot the leading-order contact-line law (3.24) in figure 3.4(a) for $n = 1$, $V_* = 1$, and several values of $\mathcal{E}$. Each curve has a unique point at which $\mathrm{d}\widehat{s}_0/\mathrm{d}\widehat{t} = 0$, from which we deduce that the leading-order contact-set radius evolves to a steady state $\widehat{s}_0 = s_e$. This steady state must satisfy the equation

$$V_* = \frac{\pi s_e^3}{4}\Phi_0\left(\frac{\mathcal{E}}{s_e^{1/2}}, n\right). \tag{3.25}$$

From our knowledge of the dependence of Φ_0 on its first argument (illustrated by figure 3.3 and the asymptotes (3.14) and (3.15)), we deduce that the right-hand side of (3.25) is a continuous, monotone-increasing function of s_e and thus that there exists a function Σ such that $s_e = \Sigma(V_*)$. A lookup table for the function Σ, which gives the equilibrium contact-set radius s_e for a given initial drop volume V_*, is created by calculating the value of V_* that satisfies (3.25) for several values of s_e (using our lookup table for Φ_0). A plot of s_e against V_* for $n = 1$ and several values of the evaporation rate $\mathcal{E}$ is shown in figure 3.4(b). We see that s_e increases with V_* and decreases with $\mathcal{E}$. We note that both of the cases $s_e < 1$ and $s_e > 1$ are possible: the contact line may either recede or advance on this timescale.

Matching with the timescale of capillary action gives an initial condition $\widehat{s}_0(0) = 1$. The initial-value problem (3.24) subject to $\widehat{s}_0(0) = 1$ is solved using MATLAB's built-in solver `ode113`; we use a lookup table and spline interpolation for the function Φ_0 (see appendix 3.A for details of how we compute Φ_0 for given values of $\mathcal{E}$ and n) and check convergence by increasing the number of terms in the lookup table and reducing the error tolerances until doing so does not change the solution to within four significant figures. The solution of the initial-value problem is plotted in figure 3.4(c) for $n = 1$, $\mathcal{E} = 1$, and several values of V_*. These plots confirm that the leading-order contact-set radius evolves to a steady state, with

$$\widehat{s}_0(\widehat{t}\,) \to s_e \quad \text{as } \widehat{t} \to \infty. \tag{3.26}$$

In figure 3.4(d), we plot the corresponding solution for the leading-order macroscopic contact angle $\widehat{\theta}_0(\widehat{t}\,)$, and we see that reaching equilibrium corresponds to $\widehat{\theta}_0$ being equal to the effective microscopic contact angle Φ_0.

To summarize this section, on the timescale of contact-line motion $\widehat{t} = t/\log(1/\lambda) = \mathrm{O}(1)$ as $\lambda \to 0$, mass is conserved to leading order. However, the leading-order drop profile spreads under surface tension according to a generalization of Tanner's law that accounts for mass transfer. The drop spreads while maintaining a profile with constant mean curvature (in the thin-film limit) and ultimately reaches an equilibrium contact-set radius such that the leading-order macroscopic contact angle is equal

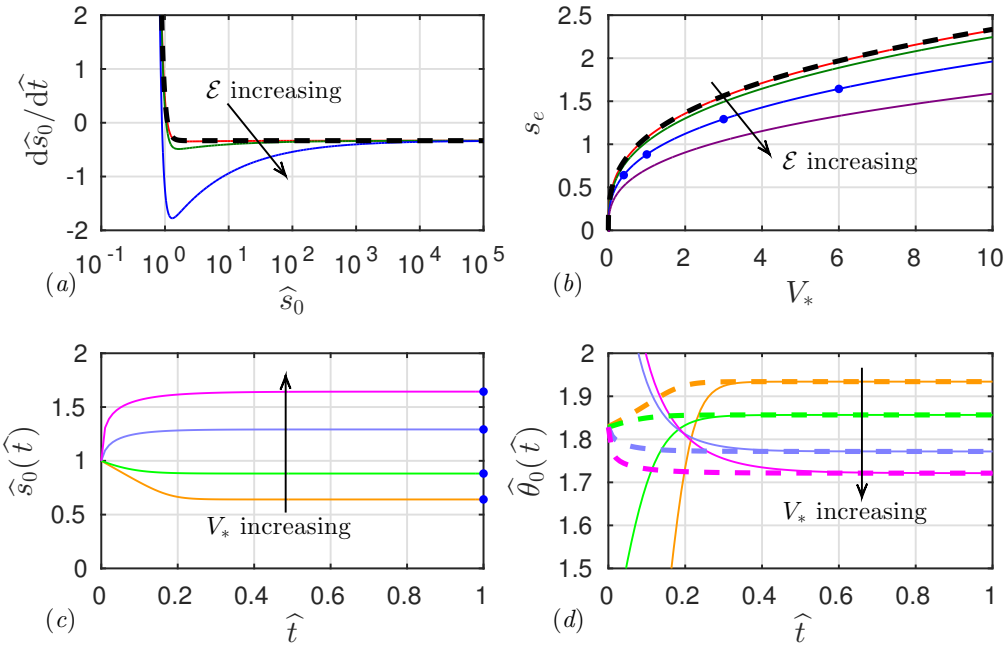

Figure 3.4: (a) The leading-order contact-line law (3.24) on the timescale of contact-line motion for $n = 1$ and $V_* = 1$. We see that the curves all intersect the $\widehat{s}_0$-axis at a single point, corresponding to the steady state $\widehat{s}_0 = s_e$. (b) Dependence of the equilibrium contact-set radius s_e on the initial drop volume V_* for $n = 1$. In (a) and (b), the red, dark green, dark blue curves correspond to $\mathcal{E} = 10^{-2}, 10^{-1}, 1$, respectively, and the black dashed curve is the solution for $\mathcal{E} = 0$, namely Tanner's law (3.21); in (b), the purple curve corresponds to $\mathcal{E} = 10$. (c) The leading-order contact-set radius $\widehat{s}_0$ as a function of time $\widehat{t}$ on the timescale of contact-line motion for $n = 1$ and $\mathcal{E} = 1$, showing the evolution to the steady state $\widehat{s}_0 = s_e$. The point marked at the end of each curve corresponds to the relevant point marked in (b). (d) The leading-order macroscopic contact angle $\widehat{\theta}_0$ as a function of time $\widehat{t}$ on the timescale of contact-line motion for $n = 1$ and $\mathcal{E} = 1$. The dashed curves are the effective microscopic contact angle $\Phi_0(\mathcal{E}/\widehat{s}_0^{1/2}, n)$; we see that $\widehat{\theta}_0 \to \Phi_0$ as $\widehat{t} \to \infty$. In (c) and (d), the orange, light green, light blue, and pink curves correspond to $V_* = 0.4, 1, 3, 6$, respectively.

to the effective microscopic contact angle. This effective microscopic contact angle depends on the evaporation rate in the inner region (and thus so does the equilibrium contact-set radius): evaporation has an effect on this timescale even though the mass of the drop is conserved to leading order.

We note that for an axisymmetric drop the non-local effects of evaporation on the contact-line law (3.24) manifest themselves in the form of the dependence of the effective microscopic contact angle on the contact-set radius, with the relevant evaporation-induced capillary number, namely $\mathcal{E}/\widehat{s}_0^{1/2}$, being proportional to the coefficient of the inverse-square-root singularity in the rate of evaporation at the contact line. If the drop were not axisymmetric, but had a smooth contact line, then to leading order the effective microscopic contact angle would vary with distance along the contact line and depend on the liquid flow solely through the geometry of the contact set (since this determines the coefficient of the inverse-square-root singularity in the rate of evaporation at the contact line in each plane perpendicular to the contact line).

3.5 Timescale of mass loss

The drop starts to lose an order-unity amount of mass on a longer timescale $T = \alpha t = \mathrm{O}(1)$ as $\lambda \to 0$. The leading-order-outer problem is quasi-steady (as for the timescale of contact-line motion) and hence has a constant-mean-curvature solution analogous to (3.22). However, mass loss now enters the global conservation of mass expression at leading order:

$$\frac{\mathrm{d}V_0}{\mathrm{d}T} = -2\pi S_0; \quad V_0 = \frac{\pi \Theta_0 S_0^3}{4}, \tag{3.27a, b}$$

where $V_0(T)$, $S_0(T)$, and $\Theta_0(T)$ denote the leading-order drop volume, contact-set radius, and macroscopic contact angle respectively. The leading-order-inner problem is the same as for the timescale of contact-line motion. An intermediate region is not required on this timescale as direct matching of the outer and inner solutions gives

$$\Theta_0 = \Phi_0 \left(\frac{\mathcal{E}}{S_0^{1/2}}, n \right) : \tag{3.28}$$

the equilibrium established on the timescale of contact-line motion persists throughout the timescale of mass loss. Thus, the problem has been reduced to a single ordinary differential equation for S_0, namely

$$\frac{\mathrm{d}}{\mathrm{d}T} \left[\frac{\pi S_0^3}{4} \, \Phi_0 \left(\frac{\mathcal{E}}{S_0^{1/2}}, n \right) \right] = -2\pi S_0. \tag{3.29}$$

Matching with the timescale of contact-line motion gives the initial condition

$$S_0(0) = \lim_{\widehat{t}\to\infty} \widehat{s}_0(\widehat{t}\,) = s_e = \Sigma(V_*). \tag{3.30}$$

We now outline an efficient method to solve the initial-value problem (3.29) and (3.30) numerically. We note from (3.25), (3.27b), and (3.28) that $S_0 = \Sigma(V_0)$, where Σ is the function that related s_e to V_* (see discussion after (3.25)). We then deduce from (3.27a) that the leading-order drop volume $V_0(T)$ at time T is given by

$$T = \frac{1}{2\pi}\int_{V_0(T)}^{V_*} \frac{\mathrm{d}v}{\Sigma(v)}. \tag{3.31}$$

In particular, the leading-order extinction time T_e of the drop, defined such that $V_0(T_e) = 0$ and $t_e \sim T_e/\alpha$ as $\lambda \to 0$, is given by

$$T_e = \frac{1}{2\pi}\int_{0}^{V_*} \frac{\mathrm{d}v}{\Sigma(v)}. \tag{3.32}$$

We will analyse the dependence of the extinction time on the parameters in our problem in §3.8. We determine numerically the evolution of the leading-order contact-set radius and drop volume on the timescale of mass loss as follows. We begin by prescribing a range of values $V_0 \in (0, V_*]$. We then evaluate numerically the integral (3.31) to find the corresponding $T(V_0)$ (using a lookup table for Σ, spline interpolation, and the function `integral` in MATLAB with sufficiently small error tolerances to resolve the integrable singularity at $v = 0$). Finally, the relationship $S_0 = \Sigma(V_0)$ is used to determine the corresponding values of S_0.

In figure 3.5(a), we plot a typical solution for the leading-order contact-set radius S_0 as a function of time T for $n = 1$ and $n = 2$ and see that the extinction time for $n = 2$ is slightly larger than the extinction time for $n = 1$. An explanation for this is as follows: the dependence of the mobility on n in the leading-order-inner thin-film equation (3.11) means that the effective microscopic contact angle is larger for $n = 2$ than for $n = 1$ (as illustrated in figure 3.3(a)). On the timescale of mass loss, the macroscopic and effective microscopic contact angles are equal so that to achieve a given drop volume, the contact-set radius must be smaller for $n = 2$ than for $n = 1$ (to compensate for the larger macroscopic contact angle). Since the total mass flux out of the drop is proportional to the contact-set radius, this means that the total mass flux for a given drop volume is smaller for $n = 2$ than for $n = 1$, resulting in a larger extinction time for $n = 2$. Since the evolution for $n = 1$ and $n = 2$ is otherwise qualitatively similar, we shall hereafter focus on the case $n = 1$ (for which it is easier to carry out numerical simulations of the full problem).

Close to extinction, the leading-order contact-set radius $S_0 \to 0^+$. Hence, $\mathcal{E}/S_0^{1/2} \to \infty$ and we deduce from the asymptote (3.15) for Φ_0 that

$$\Phi_0\left(\frac{\mathcal{E}}{S_0^{1/2}}, n\right) \sim \frac{\Phi_\infty(n)\mathcal{E}^{2/7}}{S_0^{1/7}} \quad \text{as } S_0 \to 0^+. \tag{3.33}$$

We note that the effective microscopic contact angle, and thus also the macroscopic contact angle, is unbounded as $T \to T_e^-$. We therefore expect that the lubrication approximation breaks down when $S_0 = \mathrm{O}(\Psi_R^7)$ as $\Psi_R \to 0$. However, since $\Psi_R^7 \approx 10^{-7} \ll \lambda$ for the values given in table 2.3, we expect that in practice the small-slip asymptotics will break down before the lubrication approximation does; we do not discuss the details of the breakdown further in this thesis.

We deduce from the evolution equation (3.29) and the asymptote (3.33) that

$$S_0 \sim A(T_e - T)^{7/13} \quad \text{as } T \to T_e^-, \tag{3.34}$$

where the coefficient A is given in terms of $\Phi_\infty(n)$ and $\mathcal{E}$ by

$$A = \left(\frac{26}{5\Phi_\infty(n)}\right)^{7/13} \mathcal{E}^{-2/13}, \tag{3.35}$$

and T_e is given by (3.32). Equation (3.34) is our main result: rather than the d^2-law, a (slightly modified) '$d^{13/7}$-law' is appropriate in the distinguished limit $\mathcal{E} = \mathrm{O}(1)$ as $\lambda \to 0$. We plot the numerical solution of the initial-value problem (3.29) and (3.30), together with the near-extinction asymptote (3.34) in figure 3.5(b). We see that the numerical solution agrees well with the asymptote, and that the gradient of the curve on the log-log plot is not 1/2 (in which case it would go through the bottom-left and top-right corners). We therefore have evidence that a $d^{13/7}$-law, rather than a d^2-law, is appropriate. We also see from figure 3.5(b), that the $d^{13/7}$-law in fact appears to be a good approximation to the solution for the entire mass-loss timescale, and not just close to extinction.

To summarize this section, on the timescale of mass loss $T = \alpha t = \mathrm{O}(1)$ as $\lambda \to 0$, the drop starts to lose an order-unity amount of mass. The leading-order drop profile has constant mean curvature (in the thin-film limit), as on the timescale of contact-line motion, and the leading-order macroscopic contact angle is equal to the effective microscopic contact angle throughout the mass-loss timescale. The contact line recedes from the equilibrium position it reached on the timescale of contact-line motion until the drop becomes extinct at some finite time. Close to extinction, the leading-order contact-set radius evolves as the time remaining until extinction raised

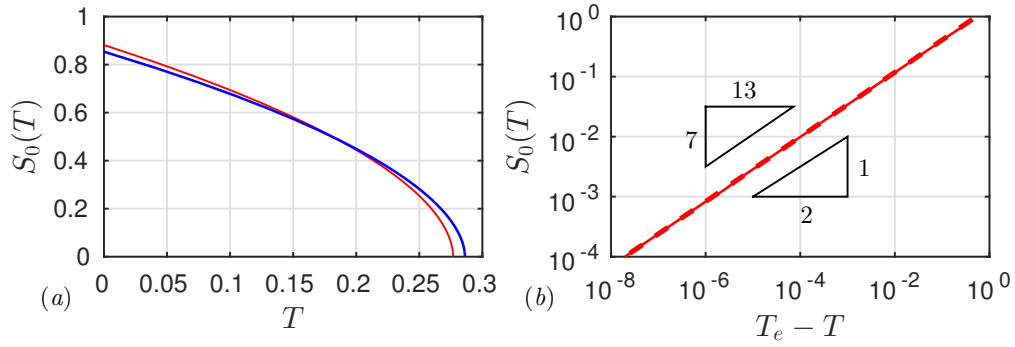

Figure 3.5: (a) The leading-order contact-set radius $S_0(T)$ as a function of time T on the mass-loss timescale for $\mathcal{E} = 1$, $V_* = 1$ with $n = 1$ (red curve) and $n = 2$ (blue curve); we see that the extinction with $n = 2$ occurs slightly later. (b) A log-log plot of S_0 against the time remaining until extinction $(T_e - T)$ for $n = 1$, $\mathcal{E} = 1$, $V_* = 1$; the solid curve is the numerical solution, obtained as described immediately after equation (3.31), while the dashed line is the $d^{13/7}$-law (3.34); we see that a $d^{13/7}$-law, rather than a d^2-law, is appropriate.

to the power 7/13: a $d^{13/7}$-law. Thus, the d^2-law is not valid in the distinguished limit in which $\mathcal{E} = \mathrm{O}(1)$ as $\lambda \to 0$ (although we note that the $d^{13/7}$-law is only a slight modification).

3.6 Small-$\mathcal{E}$ sub-limit

The analysis of §3.3–§3.5 pertains to the distinguished limit in which $\mathcal{E} = \mathrm{O}(1)$ as $\lambda \to 0$. We saw that the d^2-law was not valid in this limit. We now consider the sub-limit $\mathcal{E} \to 0$ as $\lambda \to 0$. In this case the timescale of contact-line motion is sufficiently small compared to the timescale of mass loss that the effects of evaporation do not enter the inner region to leading order. In chapter 1, we argued physically that in this case we should expect the d^2-law to be valid. We now show that this result is recovered from the results of §3.3–§3.5, but with $\mathcal{E} \to 0$.

From the asymptote (3.14) for Φ_0, we have that

$$\Phi_0\left(\frac{\mathcal{E}}{\widehat{s}_0^{1/2}}, n\right) \sim 1 \quad \text{as } \mathcal{E} \to 0 \text{ with } \mathcal{E} \ll \widehat{s}_0^{1/2}. \tag{3.36}$$

Since $\widehat{s}_0 = \mathrm{O}(1)$ on the timescale of contact-line motion, (3.36) tells us that the timescale of capillary action and the timescale of contact-line motion for this sub-limit are identical to those for the distinguished limit in which $\mathcal{E} = \mathrm{O}(1)$ as $\lambda \to 0$, but with the effective microscopic contact angle Φ_0 replaced by the true microscopic

contact angle, namely 1. Hence, the leading-order contact-line law for the timescale of contact-line motion is now precisely Tanner's law (3.21). We may solve exactly the leading-order version of the equation (3.25) for the steady state attained on the timescale of contact-line motion to give

$$s_e \sim \left(\frac{4V_*}{\pi}\right)^{1/3} \quad \text{as } \mathcal{E} \to 0. \tag{3.37}$$

On the timescale of mass loss, we begin with $S_0 = \mathrm{O}(1)$ and may therefore use the asymptote (3.36) for Φ_0. However, we note that the analysis will break down when $S_0 = \mathrm{O}(\mathcal{E}^2)$, at which point the assumption that $\mathcal{E}/S_0^{1/2} \ll 1$ becomes invalid. While this assumption *is* valid, the matching condition between the outer and inner regions (3.28) implies that the drop evolves with a constant macroscopic contact angle equal to its microscopic value, *i.e.* $\Theta_0(T) \equiv 1$. The leading-order version of the initial-value problem (3.29) and (3.30) for the drop radius may then be solved exactly to give

$$S_0(T) \sim A_0(T_{e0} - T)^{1/2} \quad \text{as } \mathcal{E} \to 0; \quad A_0 = \frac{4}{\sqrt{3}}; \quad T_{e0} = \frac{3}{16}\left(\frac{4V_*}{\pi}\right)^{2/3}. \tag{3.38}$$

We therefore do indeed recover the d^2-law in the limit $\mathcal{E} \to 0$ as $\lambda \to 0$. Moreover, this behaviour is valid from the start of the mass-loss timescale and not just close to extinction.

The leading-order solution (3.38) implies that the assumption that $\mathcal{E}/S_0^{1/2} \ll 1$ becomes invalid on the timescale $\overline{T} = (T - T_{e0})/\mathcal{E}^4 = \mathrm{O}(1)$ as $\mathcal{E} \to 0$, before the drop is extinct. To examine the near-extinction evolution on this timescale, we use the solution (3.38) to motivate scaling r, s, and h with $\mathcal{E}^2$ in both the thin-film equation given by (3.1) and (3.2) and in the boundary conditions (3.3), but on the timescale of mass loss (so that $\partial h/\partial t$ is replaced by $\alpha\,\partial h/\partial T$ in (3.1)). We find that the resulting versions of (3.1), (3.2), and (3.3) are unchanged upon replacing α and λ with $\overline{\alpha} = \alpha/\mathcal{E}^2 = \lambda/(2\alpha)$ and $\overline{\lambda} = \lambda/\mathcal{E}^2 = \lambda^2/(2\alpha^2)$, respectively. Hence, if $\lambda \ll \alpha$ as $\lambda \to 0$ (in addition to the assumption that $\alpha \ll \lambda^{1/2}$ as $\lambda \to 0$ corresponding to being in the small-$\mathcal{E}$ regime), then $\overline{\alpha} \ll 1$ and $\overline{\lambda} \ll 1$, and we deduce immediately that the asymptotic analysis in §3.5 pertains: the evolution of the contact-set radius $\overline{S}(\overline{T}) = S(T)/\mathcal{E}^2$ is governed to leading order by (3.29) but with S_0, T, and $\mathcal{E}$ replaced by $\overline{S}_0$, $\overline{T}$, and $\overline{\mathcal{E}} = (2/\overline{\lambda})^{1/2}\overline{\alpha} = 1$, respectively Matching with the leading-order solution (3.38) on the timescale of mass loss then yields the matching condition that $\overline{S}_0(\overline{T}) \sim A_0(-\overline{T})^{1/2}$ as $\overline{T} \to -\infty$. Thus, in the regime in which $\lambda \ll \alpha \ll \lambda^{1/2}$ as $\lambda \to 0$, a $d^{13/7}$-law is appropriate close to extinction. We note that if $\alpha = \mathrm{O}(\lambda)$ as

$\lambda \to 0$, then the evolution close to extinction is instead governed by the full balance of terms in (3.1) and (3.2), a regime that we do not consider further.

To summarize this section, if the ratio α of the timescales of capillary action and mass loss satisfies the condition

$$\lambda \ll \alpha \ll \lambda^{1/2} \quad \text{as } \lambda \to 0, \tag{3.39}$$

then the d^2-law is valid for the whole timescale of mass loss, except in a small temporal boundary layer close to extinction where a $d^{13/7}$-law should instead hold close to extinction. However, once α is large enough that $\mathcal{E} = \mathrm{O}(1)$ as $\lambda \to 0$, our analysis predicts that the scaling behaviour changes and instead a $d^{13/7}$-law is appropriate close to extinction on the timescale of mass loss. We note that our numerical simulations in fact suggest this law to be valid to a good approximation for the whole mass-loss timescale. A possible explanation for this extended validity of the $d^{13/7}$-law may be the following. We recall that the $d^{13/7}$-law came from the fact that, close to extinction, Φ_0 could be replaced by its large-argument asymptote (3.15). Now consider the approximation (3.16) to Φ_0; since $\Phi_\infty(n)^{7/2}$ is (moderately) large (at least for $n = 1$ and $n = 2$), the approximation (3.16) may itself be approximated by $\Phi_\infty(n)\mathcal{E}^{2/7}$. This suggests that the asymptote (3.15) is a good approximation to $\Phi_0(\mathcal{E}, n)$ even for order-unity values of $\mathcal{E}$, and consequently we do not need to be especially close to extinction for the $d^{13/7}$-law to be valid. Finally, we note that if α were sufficiently large that evaporation entered the outer or intermediate region at leading order, the behaviour would change yet again, but we do not consider further these apparently physically unrealistic regimes.

3.7 Comparison to numerical results

In order to validate our asymptotic results, we solve numerically the full problem (3.1)–(3.4) using a finite-element method. A description of the method used is given in appendix 2.A; we note in particular that the initial condition used for the simulations (3.10) is not close to that of a parabola and that we found it easier to use $n = 1$, rather than $n = 2$, in our simulations, so that the pressure is not unbounded at the contact line.

We use our leading-order asymptotic results to construct additive composite expansions for the leading-order contact-set radius and leading-order drop volume across the three timescales. Since the leading-order drop volume is constant on the timescales of capillary action and contact-line motion, the leading-order composite expansion for

the drop volume is simply given by $V_0(T)$. The leading-order contact-set radius is constant on the timescale of capillary action, so the leading-order composite expansion is obtained by adding together the solutions $\widehat{s}_0$ and S_0 on the timescales of contact-line motion and mass loss and then subtracting the 'overlap' $\widehat{s}_0(\infty) = S_0(0) = \Sigma(V_*)$.

The contact-set radius and drop volume as calculated by the full numerical solutions and the leading-order asymptotics are compared in figures 3.6(a) and 3.6(b), respectively, for $n = 1$, $V_* = 1$, and several values of $\mathcal{E}$. The plots show good agreement between the numerics and asymptotics, particularly for smaller values of $\mathcal{E}$. We can also see from these plots the presence of three distinct timescales in the evolution. There is an initial fast timescale on which the contact-set radius and drop volume are both constant. We then move to a longer timescale during which the drop volume remains constant but the contact-set radius begins to evolve: the contact line advances for smaller values of $\mathcal{E}$ and recedes for larger values of $\mathcal{E}$. Physically, the drop is equilibrating under surface tension such that its macroscopic contact angle is equal to the effective microscopic contact angle (which depends on $\mathcal{E}$), and the contact-set radius adjusts to preserve volume. Finally, there is an even longer timescale on which both the contact-set radius and drop volume decrease monotonically with time until some finite time at which they both vanish. These three timescales correspond to the timescales of capillary action, contact-line motion, and mass loss that we identified as part of our asymptotic analysis.

In figures 3.6(c) and 3.6(d), we plot s^2 and $s^{13/7}$, respectively, as functions of the time remaining until extinction. The black dashed lines join the endpoints of each curve, so that the curve should lie on top of the dashed line if the relevant near-extinction scaling law is valid. For $\mathcal{E} = 1, 10$, we see some curvature in the numerical solution in the s^2-plot, but not in the $s^{13/7}$-plot, which suggests that a $d^{13/7}$-law, rather than a d^2-law is valid close to extinction; however, we are unable to draw any conclusions based on our plots for $\mathcal{E} = 10^{-2}, 10^{-1}$.

The agreement that we have found between our leading-order asymptotic predictions and the solution as calculated by the finite-element method gives us confidence that our asymptotic results are correct.

3.8 Extinction time of the drop

We shall now investigate the dependence of the extinction time T_e of the drop on the initial drop volume V_* and the evaporation rate $\mathcal{E}$ (we shall take the slip exponent n to be equal to 1 for the reasons given in §3.5). We shall then put our results into

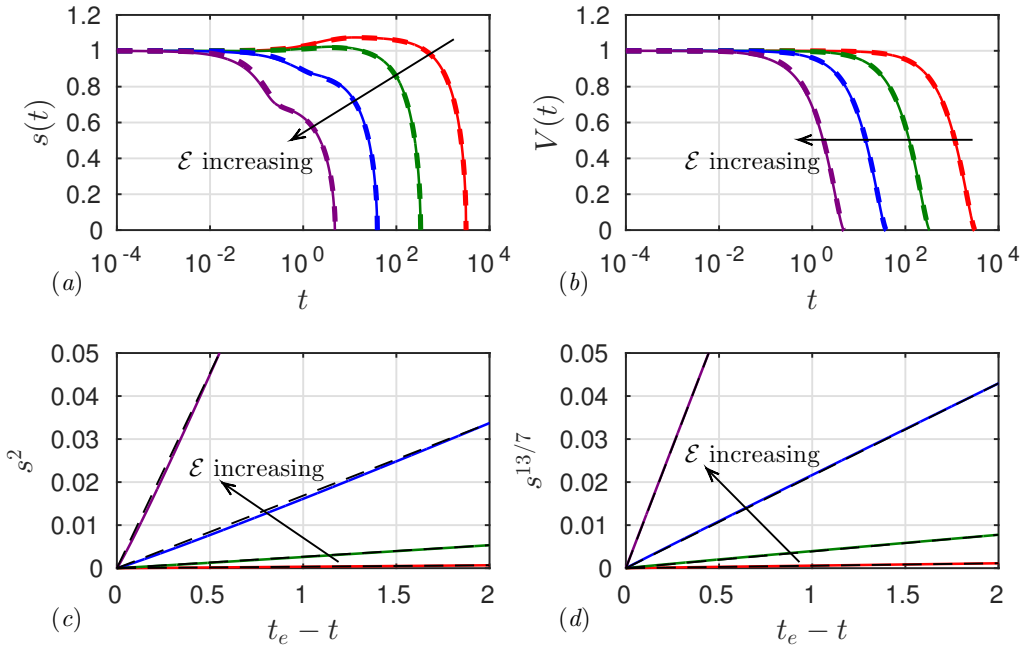

Figure 3.6: Comparison of our leading-order asymptotic predictions with the full numerical solutions with $n = 1$, $V_* = 1$, $\lambda = 10^{-4}$, and values of α chosen such that $\mathcal{E} = 10^{-2}, 10^{-1}, 1, 10$ (red, green, blue, and purple, respectively). In (a), we plot the contact-set radius s as a function of time t. In (b), we plot the drop volume V as a function of time t. The solid curves show the full numerical solutions and the dashed curves show the leading-order asymptotic solutions (which are obtained from an additive composite expansion over the three timescales, as described in the text); we see good agreement between the two methods. In (c) and (d), we plot s^2 and $s^{13/7}$, respectively, as functions of the time remaining until extinction $(t_e - t)$. The extinction time t_e is computed as described in appendix 2.A. The black dashed lines join the endpoints of each curve, so that the curve should lie on top of the dashed line if the relevant near-extinction scaling law were valid. We see that a $d^{13/7}$-law, rather than a d^2-law is valid for $\mathcal{E} = 1, 10$, but are unable to draw any conclusions based on our plots for $\mathcal{E} = 10^{-2}, 10^{-1}$.

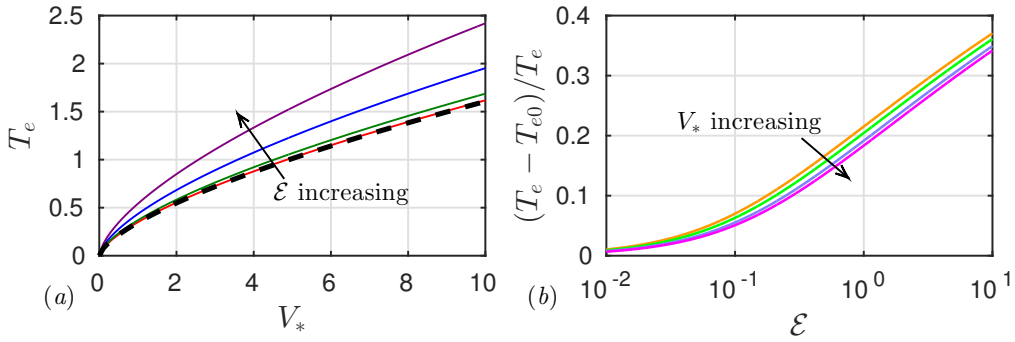

Figure 3.7: (a) Extinction time T_e of the drop as a function of the initial drop volume V_* for $n = 1$ and values of $\mathcal{E} = 10^{-2}, 10^{-1}, 1, 10$ (red, dark green, dark blue, and purple, respectively). The black dashed curve is the small-$\mathcal{E}$ asymptote. (b) The relative error in T_e introduced by assuming that the effective microscopic contact angle is equal to unity, as a function of $\mathcal{E}$ for $n = 1$ and values of $V_* = 0.4, 1, 3, 6$ (orange, light green, light blue, and pink, respectively).

context by comparing them with the case in which the effective microscopic contact angle is assumed to be constant.

We exploit the fact that our asymptotic analysis has essentially reduced the problem to a single ordinary differential equation to efficiently perform a parameter sweep of the extinction time T_e. We shall put these results into context by considering the case in which the effective microscopic angle is assumed to be equal to one. This assumption has been made in the literature when considering a 'constant contact angle mode' for the evaporation of a drop (Erbil *et al.*, 2002; Hu and Larson, 2002; Stauber *et al.*, 2014). We saw in §3.6 that this assumption should be valid when the evaporation rate $\mathcal{E}$ is small and found an exact expression (3.38c) for the quantity T_{e0} such that $t_e \sim T_{e0}/\alpha$ as $\lambda,\ \mathcal{E} \to 0$. In figure 3.7$(a)$, we plot T_e as a function of the initial drop volume V_* for several values of $\mathcal{E}$, as well as plotting the small-$\mathcal{E}$ asymptote. We see that T_e increases with both V_* and $\mathcal{E}$. We also observe that the difference between the small-$\mathcal{E}$ asymptote (3.38c) and the expression (3.32) for T_e is significant for $\mathcal{E}$ of order-unity size or larger. In figure 3.7(b), we plot the relative error $(T_e - T_{e0})/T_e$ as a function of $\mathcal{E}$ for $n = 1$ and several values of V_*. We see that the relative error grows quickly with $\mathcal{E}$ once the assumption that $\mathcal{E}$ is small ceases to be valid, with the relative error for $n = 1$, $V_* = 1$, $\mathcal{E} = 1$ being just over 20%.

3.9 Summary

Our main aim in this chapter was to answer the question of when the famous d^2-law, observed in many experiments, is valid. We considered a simplified version of the model derived in chapter 2, taking the effects of viscous dissipation, capillarity, and diffusion-dominated vapour transport into account. The effects of gravity, surface-tension gradients, and contact-angle hysteresis were neglected in favour of mathematical tractability. The stress singularity at the contact line was resolved using a generalized Navier slip law in place of the usual no-slip boundary condition.

Within the framework of this simplified model, we exploited the smallness of the slip coefficient to perform a systematic asymptotic analysis. We found that the spatial asymptotic structure on the timescale of capillary action consisted of an outer region away from the contact line, an inner region near the contact line in which the effects of slip become important, and an intermediate region, spanning all lengthscales between the outer and inner regions, which facilitates matching of the contact angles between them. We identified the distinguished limit in which the evaporation-induced capillary number

$$\mathcal{E} := \frac{2^{3/2}3^{(5/2-n)/(3-n)}\mu DM(c_e - c_\infty)}{\pi \Psi_R^{7/2}\Lambda_0^{1/2}\gamma_S \rho R^{1/2}} = \mathrm{O}(1) \quad \text{as } \lambda \to 0, \tag{3.40}$$

in which the effects of mass loss enter the inner region to leading order in λ (but not the outer or intermediate regions), resulting in a leading-order far-field (effective) microscopic contact angle larger than the actual microscopic contact angle.

In our analysis of this distinguished limit, we identified three distinct timescales in the evolution of the drop. Initially, there is the aforementioned timescale of capillary action during which the contact line does not move and mass is conserved to leading order. On this timescale, the drop relaxes under surface tension from its prescribed initial shape to a steady-state profile with constant curvature. On a longer timescale, the contact line begins to move an order-unity distance with mass still being conserved to leading order. The contact line advances or recedes according to a modified version of Tanner's law in which the microscopic contact angle is a function of the evaporation rate $\mathcal{E}$ divided by the square-root of the contact-set radius. The drop ultimately reaches a steady state with some equilibrium contact-set radius s_e that makes its macroscopic contact angle equal to the effective microscopic contact angle. The equilibrium contact-set radius was found to be a continuous, monotone-increasing function of the initial drop volume V_* and a decreasing function of the evaporation rate $\mathcal{E}$. On an even longer mass-loss timescale, the drop starts to lose an order-unity amount of mass. The contact-set radius and drop volume both decrease

monotonically with time, while the macroscopic contact angle remains equal to the effective microscopic contact angle. The contact-set radius and volume vanish at a finite time $T = T_e$, which we refer to as the extinction time of the drop. The slip exponent n was found to have a small but noticeable influence on the extinction time, with the extinction time for $n = 2$ (corresponding to a constant slip length) being slightly larger than the extinction time for $n = 1$ (corresponding to a slip length inversely proportional to the drop thickness); this is a consequence of the effective microscopic contact angle being slightly larger for $n = 2$ than for $n = 1$.

By analysing the evolution close to extinction with $\mathcal{E} = \mathrm{O}(1)$ as $\lambda \to 0$, we found that the behaviour of the leading-order contact-set radius satisfies a $d^{13/7}$-law (3.34). We next considered the sub-limit $\mathcal{E} \to 0$ of the problem and showed that the d^2-law (3.38a) is valid for the entire mass loss timescale, except for a small temporal boundary layer close to extinction, in which a $d^{13/7}$-law is appropriate close to extinction, subject to the condition (3.39). This answers our central question of when the d^2-law is valid. Our leading-order asymptotic results were validated by comparison with results generated by numerical solutions of the full problem, obtained using a finite-element method. Good agreement was found for a range of physically relevant parameter values, giving us confidence in our asymptotic predictions.

In §3.8, we analysed the dependence of the extinction time T_e on the initial drop volume V_* and the evaporation rate $\mathcal{E}$ in the inner region. We found that T_e was an increasing function of both V_* and $\mathcal{E}$. Our predictions for the extinction time were put into context by comparison with the case in which the effective microscopic contact angle is assumed to be constant.

The model on which the analysis of this chapter is based retains only the key physics to facilitate mathematical tractability. While the physical effects we neglected may be expected to be less important than those we retained for certain liquids and certain sizes of drop, in other situations these effects may be crucial to the extinction time or to the validity of the d^2-law. Therefore, in the next chapter, having gained an understanding of the underlying spatial and temporal asymptotic structure of the problem in this chapter, we shall carry out a similar analysis for the full model derived in chapter 2.

3.A Details of the inner region

In this appendix we analyse the leading-order-inner problem (3.11) and (3.13). We begin by showing that the problem is correctly specified with the leading-order far-

field microscopic contact angle $\Phi_0(\mathcal{E}, n)$ being determined as part of the solution for $n < 5/2$. We then describe how the boundary-value problem (3.11) and (3.13) is solved numerically. Finally we consider the small-$\mathcal{E}$ and large-$\mathcal{E}$ limits of the problem.

3.A.1 Local and far-field analysis

The local expansion of the solution near the contact line is given by

$$H_0 \sim X + \begin{cases} B_1 X^2 + C_1 X^{7/2-n} & \text{for } n < 3/2, \\ [C_2 \log(1/X) + B_1]\, X^2 & \text{for } n = 3/2, \\ C_1 X^{7/2-n} + B_1 X^2 & \text{for } 3/2 < n < 5/2, \end{cases} \tag{3.41}$$

as $X \to 0^+$, where $B_1(\mathcal{E}, n)$ is a degree of freedom and

$$C_1(\mathcal{E}, n) = \frac{\mathcal{E}}{(n - 3/2)(5/2 - n)(7/2 - n)}, \quad C_2(\mathcal{E}) = \frac{\mathcal{E}}{2}. \tag{3.42}$$

For $n < 5/2$, the far-field expansion of the solution is given by

$$H_0 \sim \Phi_0 X - \frac{8\mathcal{E}}{3\Phi_0^3} X^{1/2} - \frac{4\mathcal{E}^2}{\Phi_0^7} \log(X) + B_2, \tag{3.43}$$

as $X \to \infty$, where $B_2(\mathcal{E}, n)$ is a degree of freedom. There are therefore a total of three degrees of freedom (namely $B_1(\mathcal{E}, n)$, $B_2(\mathcal{E}, n)$, and $\Phi_0(\mathcal{E}, n)$) in the two expansions (3.41) and (3.43), which is equal to the order of equation (3.11). Thus, the problem (3.11) and (3.13) is correctly specified with the effective microscopic contact angle $\Phi_0(\mathcal{E}, n)$ being determined as part of the solution for $n < 5/2$.

3.A.2 Numerical solution of the boundary-value problem

This code was written by Prof. Jonathan Whiteley. We write the leading-order-inner thin-film equation (3.11) as the first-order system of equations

$$\frac{\mathrm{d}H_0}{\mathrm{d}X} = Q, \quad \frac{\mathrm{d}Q}{\mathrm{d}X} = R, \quad \frac{\mathrm{d}R}{\mathrm{d}X} = -\frac{\mathcal{E} X^{1/2}}{H_0^3 + H_0^n} \quad \text{for } X > 0, \tag{3.44a-c}$$

This system is solved subject to the boundary conditions

$$H_0(0) = 0, \quad Q(0) = 1, \quad R(\infty) = 0. \tag{3.45a-c}$$

The computational domain is truncated to $0 < X < X_N$ and then partitioned into N equally sized intervals bounded by the nodes $X_0, X_1, \ldots, X_N$. We calculate H_0 numerically by an iterative relaxation procedure as follows. An initial guess $H_0 = X$ is used to seed the iterative process. On each iteration we use the previous iterate for H_0

to first compute R by solving (3.44c) subject to the boundary condition $R(X_N) = 0$ by integrating backwards from $X = X_N$. We note that R blows up as $X \to 0^+$, so we stop solving at $X = X_1$, the first spatial node away from the origin. We then use the solution for R to solve (3.44a, b) as initial-value problems subject to the initial conditions (3.45a, b) to give an updated H_0. This is done using the backward Euler method, so that the first value of R needed is at the node $X = X_1$, rather than at the origin. We complete our iterative step by relaxing the solution for H_0, that is taking H_0 to be some weighted average of the previous iterate and the updated H_0. This iterative procedure is continued until convergence has been reached; we check that our simulations have converged in the usual way by refining the spatial mesh, and also by increasing the value of X_N.

3.A.3 Small-$\mathcal{E}$ limit

We now consider the small-$\mathcal{E}$ limit. We expand $H_0 \sim H_{00} + \mathcal{E}H_{01}$, $\Phi_0 \sim \Phi_{00} + \mathcal{E}\Phi_{01}$ as $\mathcal{E} \to 0$. It follows from the leading-order problem that

$$H_{00} = X, \quad \Phi_{00} = 1. \tag{3.46}$$

Thus, for small values of $\mathcal{E}$ the effective microscopic contact angle is approximately equal to the microscopic contact angle. We find that the $\mathrm{O}(\mathcal{E})$-correction to the effective microscopic contact angle is given by

$$\Phi_{01}(n) = \int_0^\infty \int_v^\infty \frac{u^{1/2}}{u^3 + u^n} \,\mathrm{d}u \,\mathrm{d}v, \tag{3.47}$$

the integral being finite for $n < 5/2$. In particular, we have that

$$\Phi_{01}(1) = \frac{\pi}{\sqrt{2}}, \quad \Phi_{01}(2) = \pi. \tag{3.48}$$

The small-$\mathcal{E}$ asymptote is plotted alongside the numerical solution of the boundary-value problem (3.11)–(3.13) in figure 3.3(b) for $n = 1$ and $n = 2$; we see excellent agreement with the asymptotes in their expected region of validity.

3.A.4 Large-$\mathcal{E}$ limit

Next we consider the large-$\mathcal{E}$ limit. The asymptotic structure consists of three regions. Mass loss enters in a region where $X = \mathrm{O}(\mathcal{E}^{-2/7})$ as $\mathcal{E} \to \infty$. There is also a region where $X = \mathrm{O}(1)$ as $\mathcal{E} \to \infty$ and a boundary layer in which the contact-line boundary conditions are satisfied.

We begin with the region in which mass loss enters the leading-order balance as $\mathcal{E} \to \infty$. We scale $X = \mathcal{E}^{-2/7}\overline{X}$ and expand $H_0(X) \sim H_\infty(\overline{X})$ as $\mathcal{E} \to \infty$. The leading-order thin-film equation is given by

$$(H_\infty^3 + H_\infty^n)\frac{\partial^3 H_\infty}{\partial \overline{X}^3} = -\overline{X}^{1/2} \quad \text{for } \overline{X} > 0. \tag{3.49}$$

This is to be solved solved subject to the matching conditions

$$H_\infty = 0, \ \frac{\partial H_\infty}{\partial \overline{X}} = 0 \text{ at } \overline{X} = 0^+; \quad \frac{\partial H_\infty}{\partial \overline{X}} \to \Phi_\infty(n) \text{ as } \overline{X} \to \infty. \qquad (3.50a-c)$$

The far-field expansion of the solution is analogous to that of the $\mathcal{E} = \mathrm{O}(1)$ problem (3.43), with (for $n < 5/2$)

$$H_\infty \sim \Phi_\infty \overline{X} - \frac{8}{3\Phi_\infty^3}\overline{X}^{1/2} - \frac{4}{\Phi_\infty^7}\log(\overline{X}) + \overline{B}_2 \quad \text{as } \overline{X} \to \infty, \tag{3.51}$$

where $\Phi_\infty(n)$ and $\overline{B}_2(n)$ are degrees of freedom. The near-field expansion is different due to the boundary condition (3.50b); we find that

$$H_\infty \sim \begin{cases} \overline{B}_3\overline{X}^2 + A_1\overline{X}^{7/2-2n} & \text{for } n < 3/4, \\ \left[A_2 \log^{4/7}(1/\overline{X}) + \overline{B}_3\right]\overline{X}^2 & \text{for } n = 3/4, \\ A_3\overline{X}^m + \overline{B}_3\overline{X}^{p_3} & \text{for } 3/4 < n < 5/2, \end{cases} \tag{3.52}$$

as $\overline{X} \to 0^+$, where $\overline{B}_3(n)$ is a degree of freedom; the coefficients $A_1(n)$ and $A_2(n)$ appearing in the expansions for $n < 3/4$ and $n = 3/4$, respectively, are given by

$$A_1 = -\frac{1}{\overline{B}^n(3/2-2n)(5/2-2n)(7/2-2n)}, \quad A_2 = \left(\frac{7}{8}\right)^{4/7}; \tag{3.53}$$

the coefficient $A_3(n)$ and the exponent $m(n)$ appearing in the expansion for $3/4 < n < 5/2$ are given by

$$A_3 = \left[\frac{7(n-3/4)(5/2-n)}{(n+1)^3}\right]^{-1/(n+1)}, \quad m = \frac{7}{2(n+1)}; \tag{3.54}$$

and $p_3(n)$ is the real root, satisfying $p_3 > 2$, of the cubic equation in p,

$$p(p-1)(p-2) = \frac{7n(n-3/4)(5/2-n)}{(n+1)^3}. \tag{3.55}$$

Thus, the boundary-value problem (3.49)–(3.50) is correctly specified.

Next we consider the region where $X = \mathrm{O}(1)$ as $\mathcal{E} \to \infty$. We find that

$$H_0(X) \sim \mathcal{E}^{2/7}\Phi_\infty(n)X \quad \text{as } \mathcal{E} \to \infty, \tag{3.56}$$

so that

$$\Phi_0(\mathcal{E}, n) \sim \Phi_\infty(n)\mathcal{E}^{2/7} \quad \text{as } \mathcal{E} \to \infty. \tag{3.57}$$

It is the result (3.57) that is key in deriving the 7/13 exponent in the behaviour of the contact-set radius close to extinction (3.34). The large-$\mathcal{E}$ asymptote (3.57) is plotted alongside the numerical solution of the boundary-value problem (3.11) and (3.13) in figure 3.3(b) for $n = 1$ and $n = 2$ (with $\Phi_\infty(1)$ and $\Phi_\infty(2)$ calculated numerically using a similar method to that described in appendix 3.A.2); we see excellent agreement with the asymptotes in their expected region of validity.

To be sure that this large-$\mathcal{E}$ asymptote is correct, we must consider the boundary layer in which the contact-line boundary conditions are satisfied and check that the leading-order problem in this region is correctly specified. The scalings for this region are obtained by matching with the near-field expansion of the region in which mass loss enters (3.52) and therefore are different for the three cases $n < 3/4$, $n = 3/4$, and $3/4 < n < 5/2$. If $n < 3/4$, we find that

$$H_0(X) \sim \mathcal{E}^{-4/7}(\widetilde{X} + \overline{B}_3\widetilde{X}^2) \quad \text{as } \mathcal{E} \to \infty, \text{ with } \widetilde{X} = \mathcal{E}^{4/7}X = \mathrm{O}(1). \tag{3.58}$$

If $n = 3/4$, we find that

$$H_0(X) \sim (\mathcal{E}\log\mathcal{E})^{-4/7}(\widetilde{X} + 2^{-8/7}\widetilde{X}^2) \quad \text{as } \mathcal{E} \to \infty, \text{ with } \widetilde{X} = (\mathcal{E}\log\mathcal{E})^{4/7}X = \mathrm{O}(1). \tag{3.59}$$

If $3/4 < n < 5/2$, the problem is more complicated. We set $X = \mathcal{E}^{-1/(5/2-n)}\widetilde{X}$ and expand $H_0(X) \sim \mathcal{E}^{-1/(5/2-n)}\widetilde{H}_0(\widetilde{X})$ as $\mathcal{E} \to \infty$. The leading-order problem is

$$\widetilde{H}_0^n\frac{\partial^3\widetilde{H}_0}{\partial\widetilde{X}^3} = -\widetilde{X}^{1/2} \quad \text{for } \widetilde{X} > 0, \tag{3.60}$$

subject to

$$\widetilde{H}_0 = 0, \ \frac{\partial\widetilde{H}_0}{\partial\widetilde{X}} = 1 \text{ at } \widetilde{X} = 0^+; \quad \widetilde{H}_0 \sim A_1\widetilde{X}^m \text{ as } \widetilde{X} \to \infty. \tag{3.61}$$

The near-field expansion of the solution is analogous to that of the $\mathcal{E} = \mathrm{O}(1)$ problem (3.41), with

$$\widetilde{H}_0 \sim \widetilde{X} + \begin{cases} \widetilde{B}_1\widetilde{X}^2 + C_1\widetilde{X}^{7/2-n} & \text{for } 3/4 < n < 3/2, \\ (C_2\log\widetilde{X} + \widetilde{B}_1)\widetilde{X}^2 & \text{for } n = 3/2, \\ C_1\widetilde{X}^{7/2-n} + \widetilde{B}_1\widetilde{X}^2 & \text{for } 3/2 < n < 5/2, \end{cases} \tag{3.62}$$

as $\widetilde{X} \to 0^+$, where $\widetilde{B}_1(n)$ is a degree of freedom and the coefficients $C_1(n)$ and C_2 are defined as in (3.42) but with $\mathcal{E} = 1$. The far-field expansion is

$$\widetilde{H}_0 \sim A_1 \widetilde{X}^m + \begin{cases} \widetilde{B}_2 \widetilde{X}^{p_2} + \widetilde{B}_3 \widetilde{X}^{p_1} & \text{for } 3/4 < n < n_- \text{ or } n_+ < n < 5/2, \\ (\widetilde{B}_2 \log \widetilde{X} + \widetilde{B}_3) \widetilde{X}^{p_c} & \text{for } n = n_- \text{ or } n = n_+, \\ \widetilde{B}_2 \widetilde{X}^{p_r} \cos(p_i \log \widetilde{X} + \widetilde{B}_3) & \text{for } n_- < n < n_+, \end{cases} \tag{3.63}$$

as $\widetilde{X} \to \infty$. Here $\widetilde{B}_2(n)$ and $\widetilde{B}_3(n)$ are degrees of freedom. The numbers n_- and n_+ are the two roots satisfying $3/4 < n_- < n_+ < 5/2$ of the cubic equation in n,

$$7n(n - 3/4)(5/2 - n) = \frac{2}{\sqrt{27}}(n + 1)^3. \tag{3.64}$$

The real numbers $p_1(n)$, $p_2(n)$, $p_c(n)$, $p_r(n)$, and $p_i(n)$ relate to the roots of the cubic equation (3.55) as follows. If $3/4 < n < n_-$ or $n_+ < n < 5/2$, the cubic has three real roots p_1, p_2, and p_3 with $0 < p_1 < 1 - 1/\sqrt{3} < p_2 < 1 < m < 2 < p_3$; if $n = n_-$ or $n = n_+$, the cubic has a repeated real root $p_c = 1 - 1/\sqrt{3}$ and a third real root $p_3 > 2$; if $n_- < n < n_+$, the cubic has two complex-conjugate roots $p_r \pm ip_i$ with $0 < p_r < 1 - 1/\sqrt{3}$ and one real root $p_3 > 2$. A more detailed analysis of the roots of the cubic equation (3.55) is given by Oliver *et al.* (2015), where the cubic arises in the analysis of the large-evaporation limit of their problem. We note that $n_- \approx 1.07$ and $n_+ \approx 1.88$, so the particular values $n = 1$ and $n = 2$ both correspond to the first case. We deduce from (3.63) that there is a sensitive dependence of the solution on the parameter n: there is a transition from monotonic behaviour to weak capillary ripples as n increases through n_- and then a transition back to monotonic behaviour as n increases through n_+. A similar transition of behaviour is found (when a different parameter is varied) in the analysis of evaporation-driven Stokes flow in a wedge (Gelderblom *et al.*, 2012).

The near-field and far-field expansions (3.62) and (3.63) contain a total of three degrees of freedom (namely $\widetilde{B}_1(n)$, $\widetilde{B}_2(n)$, and $\widetilde{B}_3(n)$). This is equal to the order of equation (3.60), so the boundary-layer problem is correctly specified for $3/4 < n < 5/2$, and thus for all n in the range $n < 5/2$.

Chapter 4

The effects of gravity, surface-tension gradients, and contact-angle hysteresis

4.1 Motivation

In this chapter, we extend the analysis of chapter 3 to the full version of the model that we derived in chapter 2; thus, we now take the effects of gravity, surface-tension gradients, and contact-angle hysteresis into account. A key objective of this chapter will be to determine how these effects influence the extinction time of a thin evaporating drop. We proceed by performing an asymptotic analysis in the limit in which $\alpha, \lambda \ll 1$ and $\mathrm{Bo}, \mathrm{Ma}, \mathcal{E} = \mathrm{O}(1)$ (we see from table 2.3 that this limit is the physically relevant one).

The content of this chapter is based heavily on Saxton *et al.* (2016b).

4.2 Temporal and spatial asymptotic structure

As in chapter 3, there are three distinct timescales. First, there is a timescale of capillary action, during which the contact line does not move and mass is conserved, both to leading order in λ. For sufficiently large initial drop volumes, the drop profile will be shown to relax from its prescribed initial condition to an equilibrium shape. Next, there is a timescale of contact-line motion, during which the contact line moves an order-unity distance while mass is conserved to leading order. The drop either remains pinned throughout the timescale, or evolves to an equilibrium leading-order contact-set radius that makes its macroscopic contact angle equal to an evaporation-modified effective microscopic contact angle. Finally, there is a timescale of mass

loss, during which the drop loses an order-unity amount of mass and the drop volume decreases monotonically with time until the drop has fully evaporated.

The spatial asymptotic structure on the timescale of capillary action is the same as that in chapter 3, illustrated in figure 3.1. As in chapter 3, the spatial asymptotic structure on the timescale of contact-line motion is the same as for the timescale of capillary action and on the timescale of mass loss, the outer and inner regions may be matched directly, so that an intermediate region is not needed.

4.3 Timescale of capillary action

4.3.1 Outer region

Following chapter 3, we expand $h \sim h_0$, $s \sim 1 + s_1/\log(1/\lambda)$ as $\lambda \to 0$. The evolution of the leading-order film profile $h_0(r,t)$ is governed by the thin-film equation given by

$$\frac{\partial h_0}{\partial t} + \frac{1}{r}\frac{\partial}{\partial r}(r h_0 \overline{u}_0) = 0 \quad \text{for } 0 < r < 1, \tag{4.1}$$

where

$$\overline{u}_0 = h_0^2 \frac{\partial}{\partial r}\left(\frac{\partial^2 h_0}{\partial r^2} + \frac{1}{r}\frac{\partial h_0}{\partial r} - \mathrm{Bo}\, h_0\right) + \mathrm{Ma}\, h_0 \frac{\partial}{\partial r}\left(\frac{h_0}{\sqrt{1-r^2}}\right). \tag{4.2}$$

This is to be solved subject to the boundary conditions

$$\frac{\partial h_0}{\partial r} = 0,\ r h_0 \overline{u}_0 = 0 \text{ at } r = 0^+; \quad h_0 = 0,\ -\frac{\partial h_0}{\partial r} = \theta_0 \text{ at } r = 1^-, \qquad (4.3a-d)$$

where a degree-of-freedom count reveals that the leading-order macroscopic contact angle $\theta_0(t)$ is determined as part of the solution. The leading-order-outer problem is closed by the initial condition

$$h_0(r,0) = \mathcal{H}(r) \quad \text{for } 0 \le r \le 1. \tag{4.4}$$

We deduce from the leading-order version of the expression (2.25) representing global conservation of mass that

$$2\pi \int_0^1 r h_0(r,t)\,\mathrm{d}r = V_*. \tag{4.5}$$

We look for a steady solution of (4.1)–(4.3). We set $r = \xi$, $h_0 = V_* \eta(\xi)$ and $\theta_0 = V_* \overline{\theta}$. We find that $\eta(\xi)$ is governed by the thin-film equation

$$\eta \frac{\mathrm{d}}{\mathrm{d}\xi}\left(\frac{\mathrm{d}^2\eta}{\mathrm{d}\xi^2} + \frac{1}{\xi}\frac{\mathrm{d}\eta}{\mathrm{d}\xi} - \mathcal{B}\eta\right) + \mathcal{M}\frac{\mathrm{d}}{\mathrm{d}\xi}\left(\frac{\eta}{\sqrt{1-\xi^2}}\right) = 0 \quad \text{for } 0 < \xi < 1, \tag{4.6}$$

with

$$\mathcal{B} = \mathrm{Bo}, \quad \mathcal{M} = \frac{\mathrm{Ma}}{V_*}. \tag{4.7a, b}$$

(We will see later that on the timescale on which the contact line moves an order-unity distance, the quasi-steady drop profile is also governed by the thin-film equation (4.6), but with different values of $\mathcal{B}$ and $\mathcal{M}$.) This is to be solved subject to the conditions

$$\frac{\mathrm{d}\eta}{\mathrm{d}\xi} = 0 \text{ at } \xi = 0^+; \quad \eta = 0 \text{ at } \xi = 1^-; \quad 2\pi \int_0^1 \xi\eta(\xi)\,\mathrm{d}\xi = 1. \tag{4.8$a-c$}$$

Using the solution $\eta(\xi)$ of the boundary-value problem (4.6) and (4.8a–c), we determine the function

$$\overline{\theta}(\mathcal{B}, \mathcal{M}) = -\left.\frac{\mathrm{d}\eta}{\mathrm{d}\xi}\right|_{\xi=1^-}. \tag{4.9}$$

If $\mathcal{M} = 0$ (constant surface tension), there is an exact solution (Hocking, 1983) given by

$$\overline{\theta}(\mathcal{B}, 0) = \frac{\mathcal{B}^{1/2}\mathrm{I}_1(\mathcal{B}^{1/2})}{\pi \mathrm{I}_2(\mathcal{B}^{1/2})}, \tag{4.10}$$

where I_m is the modified Bessel function of first kind of order m. The corresponding drop profile is

$$\eta(\xi) = \frac{\mathrm{I}_0(\mathcal{B}^{1/2}) - \mathrm{I}_0(\mathcal{B}^{1/2}\xi)}{\pi \mathrm{I}_2(\mathcal{B}^{1/2})} \quad \text{for } \mathcal{M} = 0. \tag{4.11}$$

We have

$$\overline{\theta}(\mathcal{B}, 0) \sim \overline{\theta}(0, 0) = \frac{4}{\pi} \quad \text{as } \mathcal{B} \to 0^+, \tag{4.12}$$

the limit corresponding to constant surface tension and no gravity. In this limit we have the classical constant-mean-curvature profile, given by

$$\eta(\xi) = \frac{2}{\pi}(1 - \xi^2) \quad \text{for } \mathcal{B} = \mathcal{M} = 0. \tag{4.13}$$

Moreover, a regular perturbation analysis reveals that

$$\overline{\theta}(\mathcal{B}, \mathcal{M}) \sim \frac{4}{\pi} + \frac{\mathcal{B}}{6\pi} - \frac{\mathcal{M}}{3} \quad \text{as } \mathcal{B}, \mathcal{M} \to 0^+, \text{ with } \frac{\mathcal{M}}{\mathcal{B}} = \mathrm{O}(1), \tag{4.14}$$

so that for small values of $\mathcal{B}$ and $\mathcal{M}$, $\overline{\theta}$ increases with $\mathcal{B}$ and decreases with $\mathcal{M}$. To see if this trend continues for larger values of $\mathcal{B}$ and $\mathcal{M}$, we solve the boundary-value problem (4.6) and (4.8a–c) numerically. Our numerical method is described in appendix 4.A.

The results of our numerical simulations are illustrated in figure 4.1(a,b). For fixed $\mathcal{B} \geq 0$, $\overline{\theta}$ decreases continuously with $\mathcal{M}$ until it vanishes at a critical effective Marangoni number $\mathcal{M}_c(\mathcal{B})$, with $\overline{\theta} \to 0^+$ as $\mathcal{M} \to \mathcal{M}_c^-$. For fixed $\mathcal{M} \leq \mathcal{M}_c$,

$\overline{\theta}$ increases continuously with $\mathcal{B}$. We are unable to find a numerical solution for $\mathcal{M} > \mathcal{M}_c$, which suggests that the leading-order-outer problem (4.1)–(4.4) has no steady-state solution in this regime. The regions of $(\mathcal{B}, \mathcal{M})$-space in which a steady-state solution does not exist are shown in figure 4.1(c). We conjecture that $\mathcal{M}_c(\mathcal{B})$ is determined as part of the solution of (4.6), (4.8a–c), and (4.9) with $\mathcal{M} = \mathcal{M}_c$ and the additional constraint that $\overline{\theta} = 0$.

In appendix 4.B, we use a combination of asymptotic and numerical methods to provide convincing evidence for the existence of the critical effective Marangoni number $\mathcal{M}_c(\mathcal{B})$. However, we note that the numerical simulations converge to the leading-order asymptotic results very slowly, meaning that the asymptotic results are not useful in any physically relevant regime. Moreover, we show that

$$\overline{\theta}(\mathcal{B}, \mathcal{M}) \sim a(\mathcal{B}) \left(\mathcal{M}_c(\mathcal{B}) - \mathcal{M}\right)^{2/(1+\sqrt{7})} \quad \text{as } \mathcal{M} \to \mathcal{M}_c(\mathcal{B})^-, \tag{4.15}$$

with $a(\mathcal{B})$ being a positive constant, at least for $0 \leq \mathcal{B} \leq 100$, and being determined as described in appendix 4.B. This behaviour guarantees that $\overline{\theta}$ is a single-valued function of $\mathcal{M}$ in the vicinity of $\mathcal{M}_c$ (and our numerical simulations suggest this to be the case elsewhere). From figure 4.1(d), we see that for $\mathcal{B} = 0$, the asymptote (4.15) agrees well with the numerical solution in the expected range of validity.

For $\mathcal{M} \leq \mathcal{M}_c(\mathcal{B})$, our numerical simulations suggest that there is a steady-state solution to the leading-order-outer problem (4.1)–(4.4). We plot the steady-state drop profile η as a function of ξ in figure 4.1(e) for $\mathcal{B} = 0, 100$ and several values of $\mathcal{M}$. For $\mathcal{B} = 0$, we see that η is a monotone-decreasing function of ξ, but for $\mathcal{B} = 100$ this is only true for small values of $\mathcal{M}$, while for larger values of $\mathcal{M}$ there is a local maximum in the drop profile, with a rim forming near the contact line. In figure 4.1(f), we plot the slope of the drop close to the contact line to more clearly illustrate this phenomenon. Numerical simulations reveal that there is a critical value of the effective Bond number $\mathcal{B}$, below which η is always a monotone-increasing function of ξ. For given $\mathcal{B}$ above this critical value, there is a critical value of the effective Marangoni number $\mathcal{M}$, below which we still have a monotonic drop profile, but above which the steady-state profile is non-monotonic with a rim near the contact line. A physical explanation for the formation of a rim is as follows. The expression (2.19) for the depth-averaged radial velocity $\overline{u}$ implies that, to leading order in the outer region,

$$\frac{\overline{u}}{V_*^3} \sim \eta^2 \frac{\mathrm{d}}{\mathrm{d}\xi}\left(\frac{\mathrm{d}^2\eta}{\mathrm{d}\xi^2} + \frac{1}{\xi}\frac{\mathrm{d}\eta}{\mathrm{d}\xi}\right) - \mathcal{B}\eta^2\frac{\mathrm{d}\eta}{\mathrm{d}\xi} + \mathcal{M}\eta\frac{\mathrm{d}}{\mathrm{d}\xi}\left(\frac{\eta}{\sqrt{1-\xi^2}}\right). \tag{4.16}$$

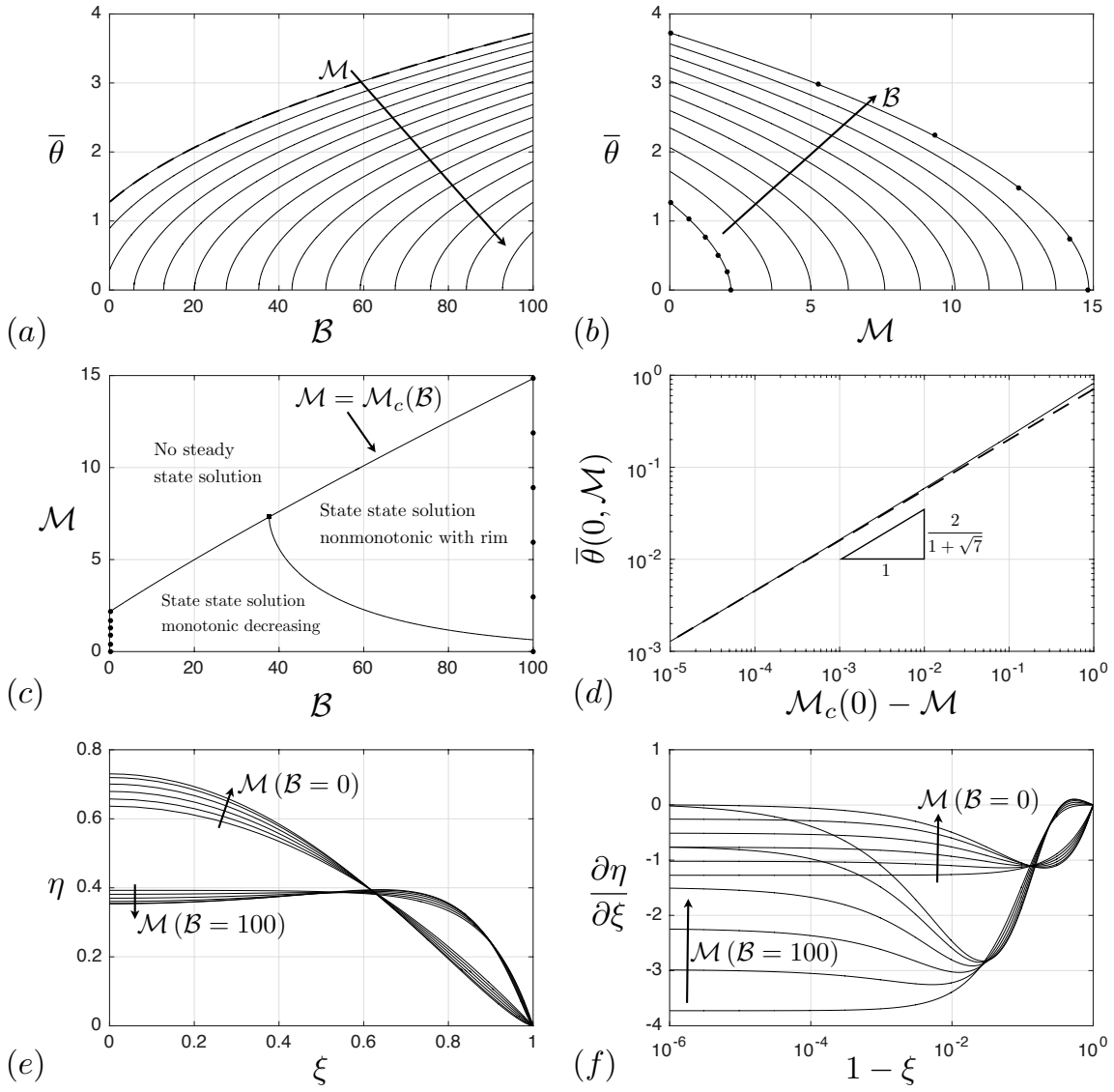

Figure 4.1: Numerical solution of the boundary-value problem (4.6), (4.8*a*–*c*), and (4.9) for the steady state attained on the timescale of capillary action. (*a*) Dependence of $\overline{\theta}$ on $\mathcal{B}$ for $\mathcal{M} = 0, 1, \ldots, 14$; the dashed curve is the exact solution when $\mathcal{M} = 0$ (4.10). (*b*) Dependence of $\overline{\theta}$ on $\mathcal{M}$ for $\mathcal{B} = 0, 10, \ldots, 100$; the points correspond to the drop profiles shown in (*e*,*f*). (*c*) Regime diagram of $(\mathcal{B}, \mathcal{M})$-space showing whether there is a steady-state solution to the boundary-value problem and, if so, whether the steady-state profile is monotonic decreasing in ξ or if it is nonmonotonic with a rim near the contact line. The points along the vertical edges of the figure correspond to the profiles in (*e*,*f*). (*d*) $\overline{\theta}(0, \mathcal{M})$ as a function of $\mathcal{M}_c(0) - \mathcal{M}$. The dashed line is the asymptote (4.15) for $\mathcal{M} \to \mathcal{M}_c^-$ with $\mathcal{B} = 0$; we see good agreement with the asymptote in its expected region of validity. (*e*) Drop profiles for $\mathcal{B} = 0, 100$ and values of $\mathcal{M}$ corresponding to the points in (*b*,*c*). (*f*) Slope of the drop close to the contact line for the profiles shown in (*e*). We see that there is a local maximum in the drop profile (corresponding to a rim) for sufficiently large $\mathcal{B}$ and $\mathcal{M}$.

In the vicinity of the contact line, the terms in (4.16) due to capillarity and gravity are positive, but the term due to surface-tension gradients is negative. Thus, for sufficiently large $\mathcal{M}$ a Marangoni flow pulls liquid away from the contact line. For sufficiently large $\mathcal{B}$, the centre of the drop is flattened by gravity so that liquid is pushed away from the centre of the drop. The combination of gravity pushing liquid away from the centre of the drop and surface-tension gradients pulling liquid away from the contact line leads to the formation of a rim. We note that the effective Bond number required for a rim is quite high, especially for low effective Marangoni numbers, meaning that a rim will not be seen in most experimentally relevant regimes. The transition between the two regimes, the point at which $\mathrm{d}^2\eta/\mathrm{d}\xi^2 = 0$ within the drop, is found numerically. The regime diagram in figure 4.1(c) shows which of the two qualitatively different steady-state profiles will occur for given values of $\mathcal{B}$ and $\mathcal{M}$.

We postulate that for $\mathcal{M} > \mathcal{M}_c(\mathcal{B})$, the nonexistence of a steady state solution to the leading-order-outer problem (4.1)–(4.4) implies that the drop profile touches down in the interior of the contact set at some finite time. For $\mathcal{M} \leq \mathcal{M}_c(\mathcal{B})$, we postulate that the steady-state solution is the large-time attractor, so that the leading-order-outer drop profile relaxes from its prescribed initial condition (4.4) to the steady state, with

$$h_0(r,t) \to V_*\eta(r), \quad \theta_0(t) \to V_*\overline{\theta}\left(\mathrm{Bo}, \frac{\mathrm{Ma}}{V_*}\right) \quad \text{as } t \to \infty. \qquad (4.17a,b)$$

This implies that, to leading order in λ, the only information from the initial drop profile (2.24) that is communicated to later timescales is the initial drop volume V_*.

To obtain evidence supporting these predictions, we solve numerically the leading-order-outer problem (4.1)–(4.4) using a finite-element method analogous to the one described in appendix 2.A. We carry out numerical simulations for $\mathrm{Bo} = \mathrm{Ma} = 1$. For $V_* = 1, 3, 6$, for which $\mathcal{M} \leq \mathcal{M}_c(\mathcal{B})$, we plot the leading-order-outer drop profile in figure 4.2(a) and the leading-order macroscopic contact angle in figure 4.2(b). We see that the large-time attractor is the steady state (4.17), as predicted. For $V_* = 0.4$, for which $\mathcal{M} > \mathcal{M}_c(\mathcal{B})$, our finite-element simulations appear to predict evolution to a steady state, as shown in figure 4.2(c). However, we see in figure 4.2(d) that the drop profile near the contact line moves towards the substrate and that the minimum drop thickness is very small. This suggests that the drop really does touch down in the interior of the contact set (near the contact line), but that our simulations do not have the accuracy necessary to resolve this.

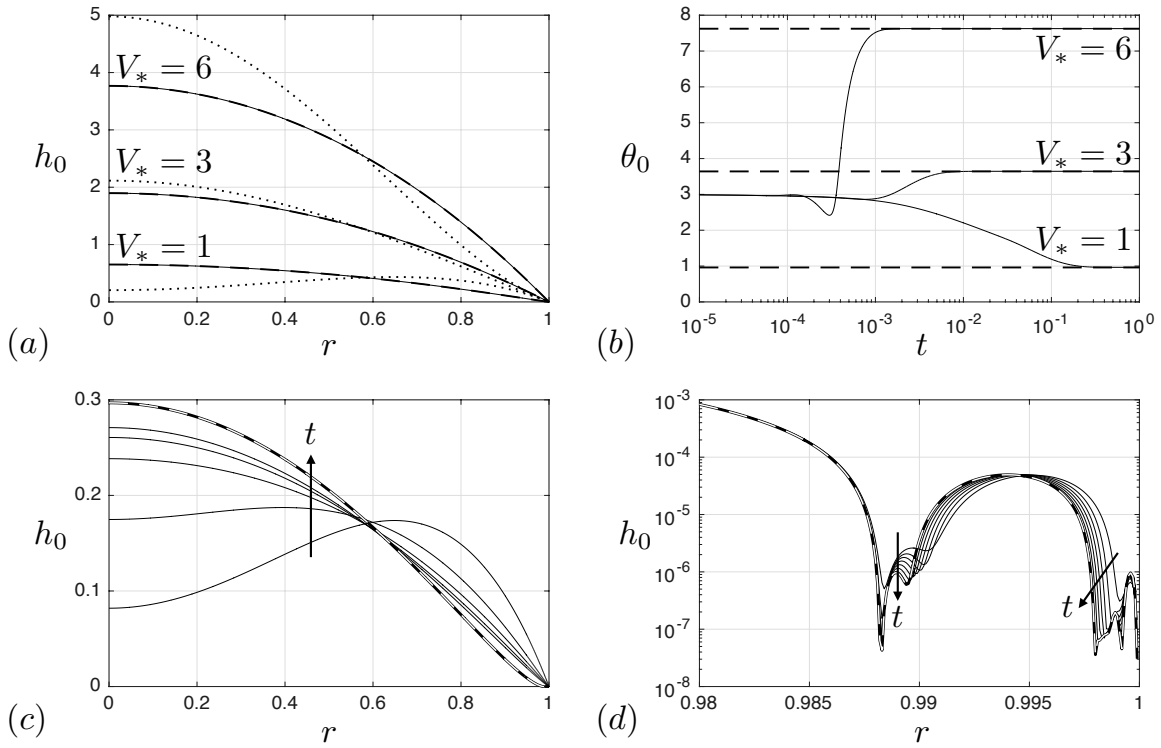

Figure 4.2: Numerical solution of leading-order-outer problem on the timescale of capillary action (4.1)–(4.4) using a finite-element method analogous to the one described in appendix 2.A. The data plotted is for $\mathrm{Bo} = \mathrm{Ma} = 1$ and (a,b) $V_* = 1, 3, 6$ with $\Psi_* = 3$, for which our analysis predicts a steady state exists, (c,d) $V_* = 0.4$ with $\Psi_* = 1.2$, for which our analysis predicts that no steady state exists. In (a) the solid curves show the finite-element solution for the leading-order-outer drop profile h_0 at time $t = 1$; the dashed curves are the theoretically predicted large-time attractors (4.17a); the dotted curves are the prescribed initial conditions. In (b) the solid curves show the finite-element solution for the evolution of the leading-order macroscopic contact angle θ_0; the dashed curves show the predicted large-time attractors (4.17b). In (c), we plot the drop profile h_0 as t increases. Our finite-element simulations predict a steady state, shown by the white dashed curve. In (d), we plot the same data as in (c) but zoom in on the contact line. The white dashed curve again shows the steady state. We see that the drop profile moves towards the substrate as t increases and that the minimum drop thickness is very small. This indicates that the drop profile actually touches down in the interior of the contact set (near the contact line).

4.3.2 Inner region

In the inner region of size $\mathrm{O}(\lambda)$ near the contact line, we follow chapter 3 by setting $h = \lambda H$, $r = s - \lambda X$ and expanding $H \sim H_0$, $s \sim 1 + s_1/\log(1/\lambda)$ as $\lambda \to 0$. We also expand $\Psi \sim \Psi_0$ as $\lambda \to 0$. The leading-order microscopic contact angle Ψ_0 satisfies the same hysteresis constraints as Ψ (2.22), but with $\dot{s}$ replaced by $\dot{s}_1$. We find that the leading-order-inner profile H_0 is governed by the same thin-film equation as in chapter 3 (3.11). This is to be solved subject to the conditions

$$H_0 = 0, \ \frac{\partial H_0}{\partial X} = \Psi_0 \text{ at } X = 0^+; \quad \frac{\partial H_0}{\partial X} \to \Phi_0\left(\mathcal{E}, n, \Psi_0\right) \text{ as } X \to \infty, \tag{4.18}$$

where Φ_0 is the leading-order far-field microscopic contact angle.

We note that when $\Psi_0 = 1$, the boundary-value problem (3.11) and (4.18) is precisely the one considered in chapter 3. We define the leading-order far-field receding microscopic contact angle, given by

$$\Phi_R(\mathcal{E}, n) := \Phi_0(\mathcal{E}, n, 1). \tag{4.19}$$

We note from chapter 3 that Φ_R is a monotone-increasing function of the evaporation rate $\mathcal{E}$ and has the asymptotes

$$\Phi_R(\mathcal{E}, n) \ \sim \ 1 + \Phi_{R1}(n)\mathcal{E} \quad \text{as } \mathcal{E} \to 0, \tag{4.20}$$

$$\Phi_R(\mathcal{E}, n) \ \sim \ \Phi_\infty(n)\mathcal{E}^{2/7} \quad \text{as } \mathcal{E} \to \infty, \tag{4.21}$$

where $\Phi_{R1}(1) = \pi/\sqrt{2}$, $\Phi_{R1}(2) = \pi$, $\Phi_\infty(1) \approx 1.750$ and $\Phi_\infty(2) \approx 1.939$ (the last two quantities being determined numerically).

We may scale $X = \widehat{X}/\Psi_0$ in (3.11) and (4.18) to deduce that

$$\Phi_0(\mathcal{E}, n, \Psi_0) = \Psi_0 \Phi_R\left(\frac{\mathcal{E}}{\Psi_0^{7/2}}, n\right). \tag{4.22}$$

In particular, for $\dot{s}_1 > 0$, the leading-order far-field advancing microscopic contact angle is given by

$$\Phi_A(\mathcal{E}, n, \Psi_H) := \Phi_0(\mathcal{E}, n, 1 + \Psi_H) = (1 + \Psi_H)\Phi_R\left(\frac{\mathcal{E}}{(1 + \Psi_H)^{7/2}}, n\right). \tag{4.23}$$

If $\dot{s}_1 \neq 0$, then Ψ_0 is given by (2.22), so that $\Psi_0 = 1$ for $\dot{s}_1 < 0$ and $\Psi_0 = 1 + \Psi_H$ for $\dot{s}_1 > 0$, and Φ_0 is a degree of freedom for the leading-order-inner problem (3.11) and (4.18). If $\dot{s}_1 = 0$, then Ψ_0 is a degree of freedom for the leading-order-inner problem and we will see that Φ_0 is determined by the leading-order-intermediate problem.

4.3.3 Intermediate region and matching

In the intermediate region, we follow chapter 3 by setting $h = (s-r)K(\zeta, t)$, $(s-r) = \lambda^{(1-\zeta)}$ and expanding $K \sim K_0$, $s \sim 1 + s_1/\log(1/\lambda)$ as $\lambda \to 0$ with $\zeta = \mathrm{O}(1)$, $0 < \zeta < 1$. We find that the leading-order mesoscopic contact angle $K_0(\zeta, t)$ satisfies the same the leading-order-intermediate problem as in chapter 3, namely (3.18) and (3.19), except now the leading-order far-field microscopic contact angle Φ_0 also depends on the leading-order microscopic contact angle Ψ_0. We deduce that the asymptote for the contact-line law as $\lambda \to 0$ is given by

$$\frac{\mathrm{d}s}{\mathrm{d}t} \sim \frac{1}{\log(1/\lambda)} \frac{\mathrm{d}s_1}{\mathrm{d}t} = \frac{\theta_0(t)^3 - \Phi_0(\mathcal{E}, n, \Psi_0)^3}{3\log(1/\lambda)} \quad \text{as } \lambda \to 0. \tag{4.24}$$

As in chapter 3, we deduce from (4.24) that the contact line moves an order-unity distance on the longer timescale $t = \mathrm{O}(\log(1/\lambda))$, and comparison of the leading-order contact-line law (4.24) to Tanner's law identifies Φ_0 as an effective microscopic contact angle accounting for evaporation.

If $\dot{s}_1 = 0$, the solvability condition (4.24) determines the degree of freedom $\Phi_0 = \theta_0$: an intermediate region is not required to match in this case. If $\dot{s}_1 \neq 0$, Φ_0 has been determined by the leading-order-inner problem and the degree of freedom $\dot{s}_1$ is given by (4.24).

4.3.4 Three evolution regimes

We shall see that when we consider the timescale of contact-line motion, the evolution of the contact-set radius may be divided into one of three behaviours depending on whether the initial leading-order contact-line velocity is positive, negative, or zero. Matching implies that we may identify which of the three regimes the drop is in by whether $\dot{s}_1$ is positive, negative, or zero at large times (on the timescale of capillary action). The condition (4.24) may be used as follows to determine which regime the drop is in. We have $\theta_0(\infty) = V_* \overline{\theta}(\mathrm{Bo}, \mathrm{Ma}/V_*)$. If $0 < \theta_0(\infty) < \Phi_R(\mathcal{E}, n)$, the contact line is receding at large times; we call this regime I. If $\Phi_R(\mathcal{E}, n) \leq \theta_0(\infty) \leq \Phi_A(\mathcal{E}, n, \Psi_H)$, the contact line is pinned at large times; we call this regime II. If $\theta_0(\infty) > \Phi_A(\mathcal{E}, n, \Psi_H)$, the contact line is advancing at large times; we call this regime III. In figure 4.3(a) we plot contours $\overline{\theta}$ = constant in $(\mathcal{B}, \mathcal{M})$-space, and in figure 4.3(b), we plot a regime diagram to show which of regimes I, II or III the drop evolves in, constructed using the dividing contours $\overline{\theta} = 0, \Phi_R/V_*, \Phi_A/V_*$.

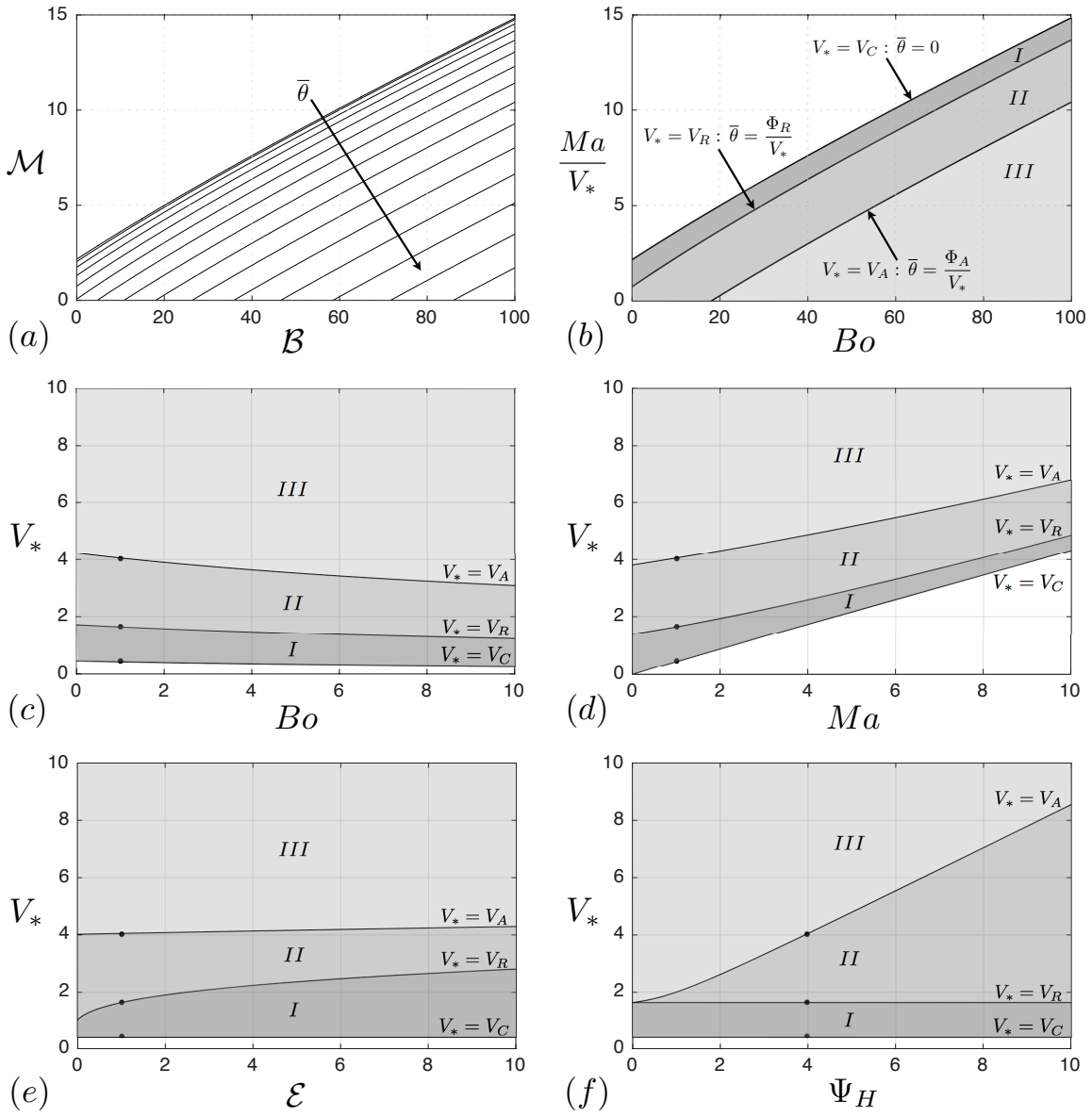

Figure 4.3: (a) Plot of $(\mathcal{B}, \mathcal{M})$-space showing contours $\overline{\theta} = 0, 1, 2, \ldots$. ($b$) Regime diagram showing whether the drop will touch down in finite time, or evolve in regime I (contact line receding at large times on the timescale of capillary action), regime II (contact line pinned at large times on the timescale of capillary action), or regime III (contact line advancing at large times on the timescale of capillary action); this depends on the positions of the contours $\overline{\theta} = 0$, $\overline{\theta} = \Phi_R/V_*$, and $\overline{\theta} = \Phi_A/V_*$. ($c$–$f$) The critical volumes $V_* = V_C, V_R, V_A$ as functions of (c) the Bond number Bo, (d) the Marangoni number Ma, (e) the evaporation rate $\mathcal{E}$, and (f) the hysteresis Ψ_H. In each plot, we have Bo = 1, Ma = 1, $\mathcal{E} = 1$, and $\Psi_H = 4$ (and $n = 1$), unless a parameter is explicitly varied. The points shown are the same in each plot, giving the values $V_C \approx 0.43$, $V_R \approx 1.64$, and $V_A \approx 4.05$.

We note that corresponding to the critical effective Marangoni number $\mathcal{M} = \mathcal{M}_c(\mathcal{B})$, there is a critical initial volume $V_* = V_C$, given by

$$V_C = \frac{\mathrm{Ma}}{\mathcal{M}_c(\mathrm{Bo})}, \tag{4.25}$$

such that there is no steady-state solution to the leading-order-outer problem for $0 \leq V_* < V_C$. The dependence of V_C on the parameters in our model is illustrated in figure 4.3(c–f). We see that V_C decreases very slightly with Bo and increases with Ma; V_C is independent of $\mathcal{E}$ and Ψ_H. A physical explanation for the dependence of V_C on Bo and Ma is as follows. We recall that the condition $V_* = V_C$ is equivalent to the condition $\overline{\theta} = 0$. As Ma increases, the Marangoni flow pulls more liquid away from the contact line so that the condition $\overline{\theta} = 0$ can be achieved for a larger drop volume V_*: V_C increases with Ma. As Bo increases, the centre of the drop is flattened so that for a fixed volume V_* there is more liquid near the contact line. Thus the volume $V_* = V_C$ at which the Marangoni flow can pull liquid away from the contact line to make $\overline{\theta} = 0$ is smaller: V_C decreases with Bo.

In addition, it follows from figure 4.3(b) that the condition $\theta_0(\infty) = \Phi_R$ corresponds to a unique critical volume $V_* = V_R$. An explicit expression for V_R will be determined later in §4.5.1. This critical volume V_R may be determined by solving the thin-film equation (4.6) with $\mathcal{M} = \mathrm{Ma}/V_R$ subject to the conditions (4.8a–c) and (4.9) with $\overline{\theta} = \Phi_R(\mathcal{E}, n)/V_R$, and obtaining V_R as a degree of freedom. The dependence of V_R on the parameters in our model is illustrated in figure 4.3(c–f). We see that V_R decreases slightly with Bo, increases with Ma, and increases with $\mathcal{E}$; V_R is independent of Ψ_H. A physical explanation for these trends is as follows. We recall that the condition $V_* = V_R$ is equivalent to the macroscopic contact angle being equal to the effective receding microscopic contact angle. As Bo increases, there is more liquid near the contact line for the reasons given in the previous paragraph. This increases the macroscopic contact angle, so that a smaller volume V_* is needed to make it equal to the effective receding microscopic contact angle: V_R decreases with Bo. As Ma increases, there is less liquid near the contact line for the reasons given in the previous paragraph and so V_R increases with Ma (for the same reasoning behind the Bo trend). As $\mathcal{E}$ increases, the effective receding microscopic contact angle increases (see figure 3.3(a)) and so a larger volume is needed to make the macroscopic contact angle equal to the effective microscopic contact angle: V_R increases with $\mathcal{E}$.

It also follows from figure 4.3(b) that the condition $\theta_0(\infty) = \Phi_A$ corresponds to a unique critical volume $V_* = V_A$. An explicit expression for V_A will be determined later in §4.5.1. This critical volume V_A may be determined by solving the thin-film

equation (4.6) with $\mathcal{M} = \mathrm{Ma}/V_A$ subject to the conditions (4.8*a*–*c*) and (4.9) with $\overline{\theta} = \Phi_A(\mathcal{E}, n, \Psi_H)/V_A$, and obtaining V_A as a degree of freedom. The dependence of V_A on the parameters in our model is illustrated in figure 4.3(*c*–*f*). We see that V_A decreases with Bo, increases with Ma, increases very slightly with $\mathcal{E}$, and increases significantly with Ψ_H (with $V_R = V_A$ for $\Psi_H = 0$). A physical explanation for the dependence of V_A on Bo, Ma, and $\mathcal{E}$ is the same as for V_R above, except that the effective receding microscopic contact angle is replaced by the effective advancing microscopic contact angle. If the contact line is advancing, the true microscopic contact angle Ψ increases with Ψ_H and so the effective advancing microscopic contact angle is an increasing function of Ψ_H also. Thus, a larger volume is needed to make the macroscopic contact angle equal to the effective advancing microscopic contact angle: V_A increases with Ψ_H.

In summary, on the timescale of capillary action $t = \mathrm{O}(1)$ as $\lambda \to 0$, mass is conserved and the contact line does not move, both to leading order. Our analysis suggests that there exists a critical initial drop volume $V_* = V_C$ such that there is no steady-state solution to the leading-order problem for $0 < V_* < V_C$ and the free surface touches down in the interior of the contact set at some finite time on this timescale. For $V_* \geq V_C$, our analysis suggests that the leading-order drop profile evolves from its prescribed initial value to a steady-state profile. Henceforth, we shall consider only the case $V_* \geq V_C$.

4.4 Timescale of contact-line motion

In §4.3, we deduced that the contact line begins to move an order-unity distance on the timescale $\widehat{t} = t/\log(1/\lambda) = \mathrm{O}(1)$ as $\lambda \to 0$. We expand $s(t) \sim \widehat{s}_0(\widehat{t}\,)$ as $\lambda \to 0$. Matching with the timescale of capillary action implies that

$$\lim_{\widehat{t}\to 0^+} \frac{\mathrm{d}\widehat{s}_0}{\mathrm{d}\widehat{t}} = \lim_{t\to\infty} \frac{\mathrm{d}s_1}{\mathrm{d}t}, \tag{4.26}$$

so that to leading order the contact line is receding initially in regime I, pinned initially in regime II and advancing initially in regime III.

We begin with the outer region by expanding $h(r,t) \sim \widehat{h}_0(r, \widehat{t}\,)$ as $\lambda \to 0$. The leading-order-outer problem is quasi-steady with no mass loss. We set $r = \widehat{s}_0\xi$, $h_0 = V_*\eta/\widehat{s}_0^2$ and $\widehat{\theta}_0 = V_*\overline{\theta}/\widehat{s}_0^3$, where $\widehat{\theta}_0(\widehat{t}\,)$ is the leading-order macroscopic contact angle. We obtain the same boundary-value problem as for the steady state on the timescale of capillary action, *i.e.* (4.6), (4.8*a*–*c*), and (4.9), but with

$$\mathcal{B} = \mathrm{Bo}\,\widehat{s}_0^2, \quad \mathcal{M} = \frac{\mathrm{Ma}\,\widehat{s}_0^3}{V_*}. \tag{4.27a, b}$$

Thus, the leading-order macroscopic contact angle $\widehat{\theta}_0(\widehat{t}\,)$ is given in terms of the function $\overline{\theta}(\mathcal{B},\mathcal{M})$ by

$$\widehat{\theta}_0 = \frac{V_*}{\widehat{s}_0^3}\overline{\theta}\left(\mathrm{Bo}\,\widehat{s}_0^2, \frac{\mathrm{Ma}\,\widehat{s}_0^3}{V_*}\right). \tag{4.28}$$

We note that the leading-order contact-set radius $\widehat{s}_0(\widehat{t}\,)$ is not determined as part of the solution to the leading-order-outer problem.

As in chapter 3, the leading-order-inner problem is the same as for the timescale of capillary action, namely (3.11) and (4.18), except that the evaporation rate $\mathcal{E}$ appearing on the right-hand side of the thin-film equation (3.11) is replaced by $\mathcal{E}/\widehat{s}_0^{1/2}$.

In the intermediate region, we set $(s-r) = \lambda^{(1-\zeta)}$ and expand $h(r,t) \sim (\widehat{s}_0 - r)\widehat{K}_0(\zeta,\widehat{t}\,)$, $s(t) \sim \widehat{s}_0(\widehat{t}\,)$ as $\lambda \to 0$ with $\zeta = \mathrm{O}(1)$, $0 < \zeta < 1$. We find that the leading-order mesoscopic contact angle $K_0(\zeta,\widehat{t}\,)$ satisfies (3.18) and (3.19), but with $\mathrm{d}s_1/\mathrm{d}t$ and $\mathcal{E}$ replaced by $\mathrm{d}\widehat{s}_0/\mathrm{d}\widehat{t}$ and $\mathcal{E}/\widehat{s}_0^{1/2}$, respectively. We deduce immediately from the consistency condition for the resulting leading-order-intermediate problem the leading-order contact-line law

$$\frac{\mathrm{d}\widehat{s}_0}{\mathrm{d}\widehat{t}} = \frac{1}{3}\left[\widehat{\theta}_0^3 - \Phi_0\left(\frac{\mathcal{E}}{\widehat{s}_0^{1/2}}, n, \Psi_0\right)^3\right]. \tag{4.29}$$

In regime II, in which the contact line is pinned initially, (4.29) implies that the contact line is pinned to leading order throughout this timescale with $\widehat{s}_0 \equiv 1$ and $\widehat{\theta}_0 = \Phi_0(\mathcal{E}, n, \Psi_0)$.

In figure 4.4(a), we plot $\widehat{\theta}_0$, $\Phi_R(\mathcal{E}/\widehat{s}_0^{1/2}, n)$ and $\Phi_A(\mathcal{E}/\widehat{s}_0^{1/2}, n, \Psi_H)$ as functions of $\widehat{s}_0$ for $\mathcal{E} = 1$, $\mathrm{Bo} = 1$, $\mathrm{Ma} = 1$, $\Psi_H = 4$ and several values of V_*. We see that each $\widehat{\theta}_0$-curve intersects the Φ_R- and Φ_A-curves at a unique value of $\widehat{s}_0$. This implies the existence of a unique steady state value of $\widehat{s}_0$ in regimes I and III, in which the contact line is moving initially, with

$$\widehat{s}_0(\widehat{t}\,) \to s_e \quad \text{as } \widehat{t} \to \infty. \tag{4.30}$$

Thus, on the timescale of contact-line motion, the contact line recedes from its initial position to an equilibrium contact-set radius $s_e < 1$ in regime I, remains pinned at its initial contact-set radius $s_e = 1$ in regime II, and advances from its initial position to an equilibrium contact-set radius $s_e > 1$ in regime III.

Using (4.28) and (4.29), we deduce that in regime I, the equilibrium contact-set radius s_e must satisfy the equation

$$\frac{V_*}{s_e^3}\overline{\theta}\left(\mathrm{Bo}\,s_e^2, \frac{\mathrm{Ma}\,s_e^3}{V_*}\right) = \Phi_R\left(\frac{\mathcal{E}}{s_e^{1/2}}, n\right). \tag{4.31}$$

It follows from the contour plot in figure 4.3(b) that (4.31) implies that there exists a function Σ such that, in regime I,

$$s_e = \Sigma(V_*; \mathcal{E}, \mathrm{Bo}, \mathrm{Ma}, n). \tag{4.32}$$

In regime III, we deduce from the relationship between the functions Φ_R and Φ_A (4.23) that

$$s_e = \Sigma\left(\frac{V_*}{1+\Psi_H}; \frac{\mathcal{E}}{(1+\Psi_H)^{7/2}}, \mathrm{Bo}, \frac{\mathrm{Ma}}{1+\Psi_H}, n\right). \tag{4.33}$$

For the parameter values given above, the dependence of the equilibrium contact-set radius s_e on the initial drop volume V_* is illustrated in figure 4.4(b). We see that the value of s_e is continuous between the regimes and is a monotone-increasing function of V_* in regimes I and III. For other parameter values, the curves in figure 4.4(a) are shifted but the topology remains the same, so that a unique steady state still exists. The dependence of s_e on the other parameters in the model is illustrated later in figure 4.8(a).

We integrate the contact-line law (4.29) for the initial condition $\widehat{s}_0(0) = 1$ using the function `ode15s` in MATLAB, and plot the resulting evolution of $\widehat{s}_0(\widehat{t}\,)$ in figure 4.4(c). This verifies that the contact-set radius reaches an equilibrium value as $\widehat{t} \to \infty$. For fixed $\widehat{t}$, we use the corresponding value of $\widehat{s}_0$ to calculate the value of $\widehat{\theta}_0$ from (4.28) using a lookup table and spline interpolation for the function $\overline{\theta}$. We plot the resulting evolution of $\widehat{\theta}_0(\widehat{t}\,)$ in figure 4.4(d), and we see that $\widehat{\theta}_0$ also reaches an equilibrium value as $\widehat{t} \to \infty$.

In summary, on the timescale of contact-line motion $\widehat{t} = t/\log(1/\lambda) = \mathrm{O}(1)$ as $\lambda \to 0$, mass is conserved to leading order. If the contact line is pinned initially, then it does not move to leading order on this timescale. If the contact line is moving initially, then it evolves according to a generalization of Tanner's law that accounts for mass transfer. As in chapter 3, the drop ultimately reaches an equilibrium contact-set radius s_e such that the leading-order macroscopic contact angle is equal to the effective microscopic contact angle.

4.5 Timescale of mass loss

4.5.1 Outer region

The drop starts to lose an order-unity amount of mass on a longer timescale $T = \alpha t = \mathrm{O}(1)$ as $\lambda \to 0$. The leading-order-outer problem is quasi-steady (as for the timescale of contact-line motion). We let $S_0(T)$ and $\Theta_0(T)$ denote the leading-order

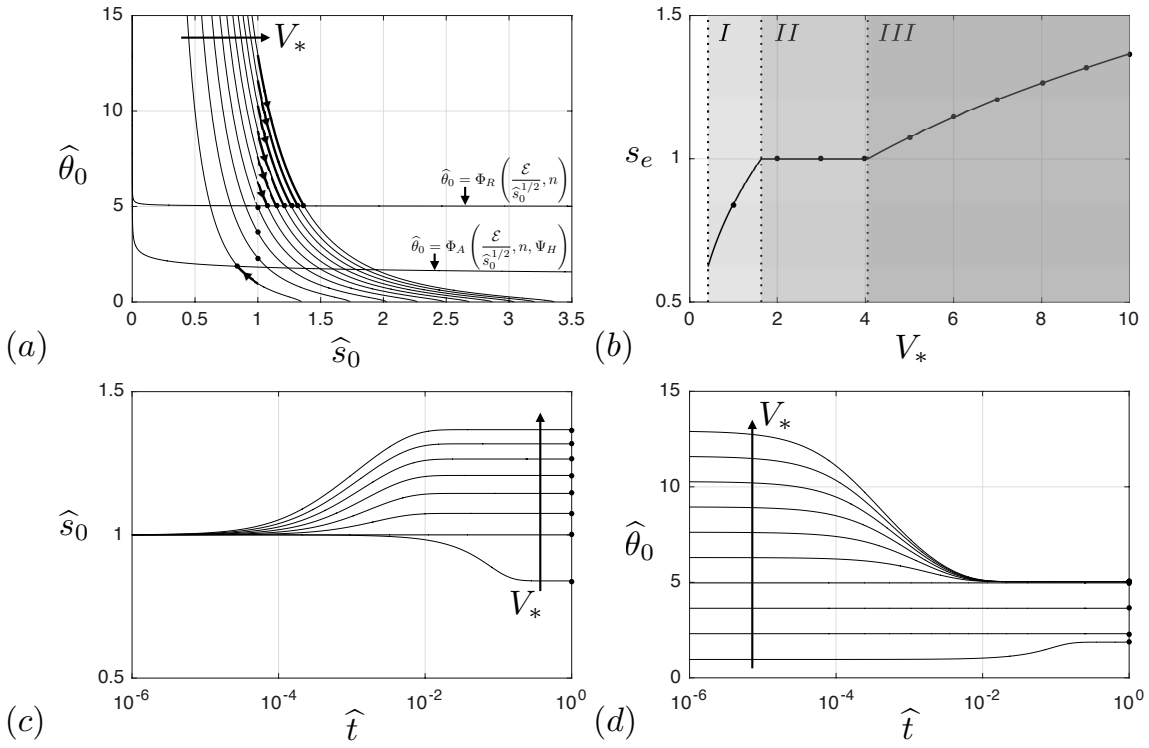

Figure 4.4: Evolution on the timescale of contact-line motion for Bo = 1, Ma = 1, $\mathcal{E} = 1$, $n = 1$, and $\Psi_H = 4$. (a) The leading-order macroscopic contact angle $\widehat{\theta}_0$ as a function of the leading-order contact-set radius $\widehat{s}_0$ for $V_* = 1, 2, \ldots, 10$, along with the curves $\widehat{\theta}_0 = \Phi_R(\mathcal{E}/\widehat{s}_0^{1/2}, n)$ and $\widehat{\theta}_0 = \Phi_A(\mathcal{E}/\widehat{s}_0^{1/2}, n, \Psi_H)$. The arrows along the curves illustrate evolution from the initial condition $\widehat{s}_0(0) = 1$ to the steady state $\widehat{s}_0 = s_e$. (b) Value of the steady-state s_e as a function of V_*. The points at $V_* = 1, 2, \ldots, 10$ correspond to those shown in (a). (c) The leading-order contact-set radius $\widehat{s}_0$ and (d) the leading-order macroscopic contact angle $\widehat{\theta}_0$, as functions of time $\widehat{t}$ for $V_* = 1, 2, \ldots, 10$ (note that $V_* = 2, 3, 4$ are all in regime II and thus give $\widehat{s}_0 \equiv 1$). We see explicitly that $\widehat{s}_0$ and $\widehat{\theta}_0$ evolve to a steady state on this timescale.

contact-set radius and macroscopic contact angle, respectively, and set $r = S_0\xi$ and $h = \Theta_0 S_0 \eta$. We find that η satisfies the same thin-film equation as on the previous two timescales (4.6) and the same boundary conditions (4.8*a,b*), but now with

$$\mathcal{B} = \mathrm{Bo}\, S_0^2, \quad \mathcal{M} = \frac{\mathrm{Ma}}{\Theta_0}. \qquad (4.34a, b)$$

and the condition (4.8*c*) replaced by

$$-\frac{\mathrm{d}\eta}{\mathrm{d}\xi} = 1 \text{ at } \xi = 1^-. \qquad (4.35)$$

Since the problem is quasi-steady, we suppress the dependence of η on T (which occurs through $\mathcal{B}$ and $\mathcal{M}$). Using the solution $\eta(\xi)$ of the boundary-value problem (4.6), (4.8*a,b*) and (4.35), we determine the function

$$\overline{V}(\mathcal{B}, \mathcal{M}) = 2\pi \int_0^1 \xi \eta(\xi)\, \mathrm{d}\xi, \qquad (4.36)$$

from which we determine, in terms of Θ_0 and S_0, the leading-order drop volume

$$V_0 = \Theta_0 S_0^3 \overline{V} \left(\mathrm{Bo}\, S_0^2, \frac{\mathrm{Ma}}{\Theta_0} \right). \qquad (4.37)$$

We note that there is a relationship between the boundary-value problem (4.6), (4.8*a–c*), and (4.9) for the function $\overline{\theta}$ and the boundary-value problem (4.6), (4.8*a,b*), (4.35), and (4.36) for the function $\overline{V}$. By setting $\eta = \overline{\eta}/\overline{\theta}$ in (4.6), (4.8*a,b*), (4.35), and (4.36), we deduce that

$$\overline{\theta}(\mathcal{B}, \mathcal{M}) \overline{V} \left(\mathcal{B}, \frac{\mathcal{M}}{\overline{\theta}(\mathcal{B}, \mathcal{M})} \right) = 1 \quad \text{and} \quad \overline{\theta} \left(\mathcal{B}, \frac{\mathcal{M}}{\overline{V}(\mathcal{B}, \mathcal{M})} \right) \overline{V}(\mathcal{B}, \mathcal{M}) = 1. \qquad (4.38)$$

Using (4.38), we deduce from the solution of the boundary-value problem for $\overline{\theta}$ when $\mathcal{M} = 0$ (4.10) that

$$\overline{V}(\mathcal{B}, 0) = \frac{\pi \mathrm{I}_2(\mathcal{B}^{1/2})}{\mathcal{B}^{1/2} \mathrm{I}_1(\mathcal{B}^{1/2})}, \qquad (4.39)$$

with

$$\overline{V}(\mathcal{B}, 0) \sim \overline{V}(0, 0) = \frac{\pi}{4} \quad \text{as } \mathcal{B} \to 0^+. \qquad (4.40)$$

Moreover, a regular perturbation analysis reveals that

$$\overline{V}(\mathcal{B}, \mathcal{M}) \sim \frac{\pi}{4} - \frac{\pi \mathcal{B}}{96} + \frac{\pi \mathcal{M}}{12} \quad \text{as } \mathcal{B}, \mathcal{M} \to 0^+, \text{ with } \frac{\mathcal{M}}{\mathcal{B}} = \mathrm{O}(1), \qquad (4.41)$$

so that for small values of $\mathcal{B}$ and $\mathcal{M}$, $\overline{V}$ decreases with $\mathcal{B}$ and increases with $\mathcal{M}$. To see if this trend continues for larger values of $\mathcal{B}$ and $\mathcal{M}$, we solve the boundary-value

problem (4.6), (4.8*a,b*) and (4.35) numerically. Our numerical method is described in appendix 4.A.

The results of our numerical simulations are illustrated in figure 4.5(*a*–*c*). For fixed $\mathcal{B} \geq 0$, $\overline{V}$ increases continuously with $\mathcal{M}$, while for fixed $\mathcal{M} \geq 0$, $\overline{V}$ decreases continuously with $\mathcal{B}$. We note that we are able to find a solution to the boundary-value problem (4.6), (4.8*a,b*) and (4.35) even for $\mathcal{M} > \mathcal{M}_c$, in contrast to the boundary-value problem (4.6) and (4.8*a*–*c*) on the timescale of contact-line motion.

Our numerical simulations predict that the quasi-steady drop profile η may either be a monotone-decreasing function of ξ, or may be non-monotonic with a rim near the contact line. We gave a physical explanation for these different behaviours when describing the steady-state drop profiles in §4.3 (see paragraph between (4.15) and (4.17)). The transition between these two regimes, at which $\mathrm{d}^2\eta/\mathrm{d}\xi^2 = 0$ at $\xi = 0$, is found numerically. In figure 4.5(*d*), we plot which regions of $(\mathcal{B}, \mathcal{M})$-space exhibit each of these behaviours. We plot some example drop profiles in figure 4.5(*e*) to demonstrate these two possible behaviours, and plot the corresponding drop slope in figure 4.5(*f*).

The relationship (4.38) has some important implications. Firstly, it gives another method by which to compute the function $\overline{\theta}(\mathcal{B}, \mathcal{M})$: we may first solve the boundary-value problem (4.6), (4.8*a,b*), and (4.35) to determine $\overline{V}$ via (4.36), and then determine $\overline{\theta}$ implicitly from (4.38). In principle, this may be easier than solving the boundary-value problem (4.6) and (4.8*a*–*c*) directly, and then determining $\overline{\theta}$ via (4.9), since it is easier to work with three boundary conditions than two boundary conditions plus an integral constraint. In practice, a combination of this method and others is used to determine $\overline{\theta}$, as described in appendix 4.A.

Secondly, it is now possible to determine more directly which of the three evolution regimes from the timescale of contact-line motion the drop is in, given its initial volume V_*. We recall that the transition between regime I (in which the contact line recedes on the timescale of contact-line motion) and regime II (in which the contact line is pinned on the timescale of contact-line motion) is given by the condition $\theta_0(\infty) = \Phi_R(\mathcal{E}, n)$, where $\theta_0(\infty) = V_*\overline{\theta}(\mathrm{Bo}, \mathrm{Ma}/V_*)$. Similarly, the transition between regime II and regime III (in which the contact line advances on the timescale of contact-line motion) is given by the condition $\theta_0(\infty) = \Phi_A(\mathcal{E}, n, \Psi_H)$. We deduce from (4.38) that the critical volumes $V_* = V_R$ and $V_* = V_A$ defined in §4.3 are given

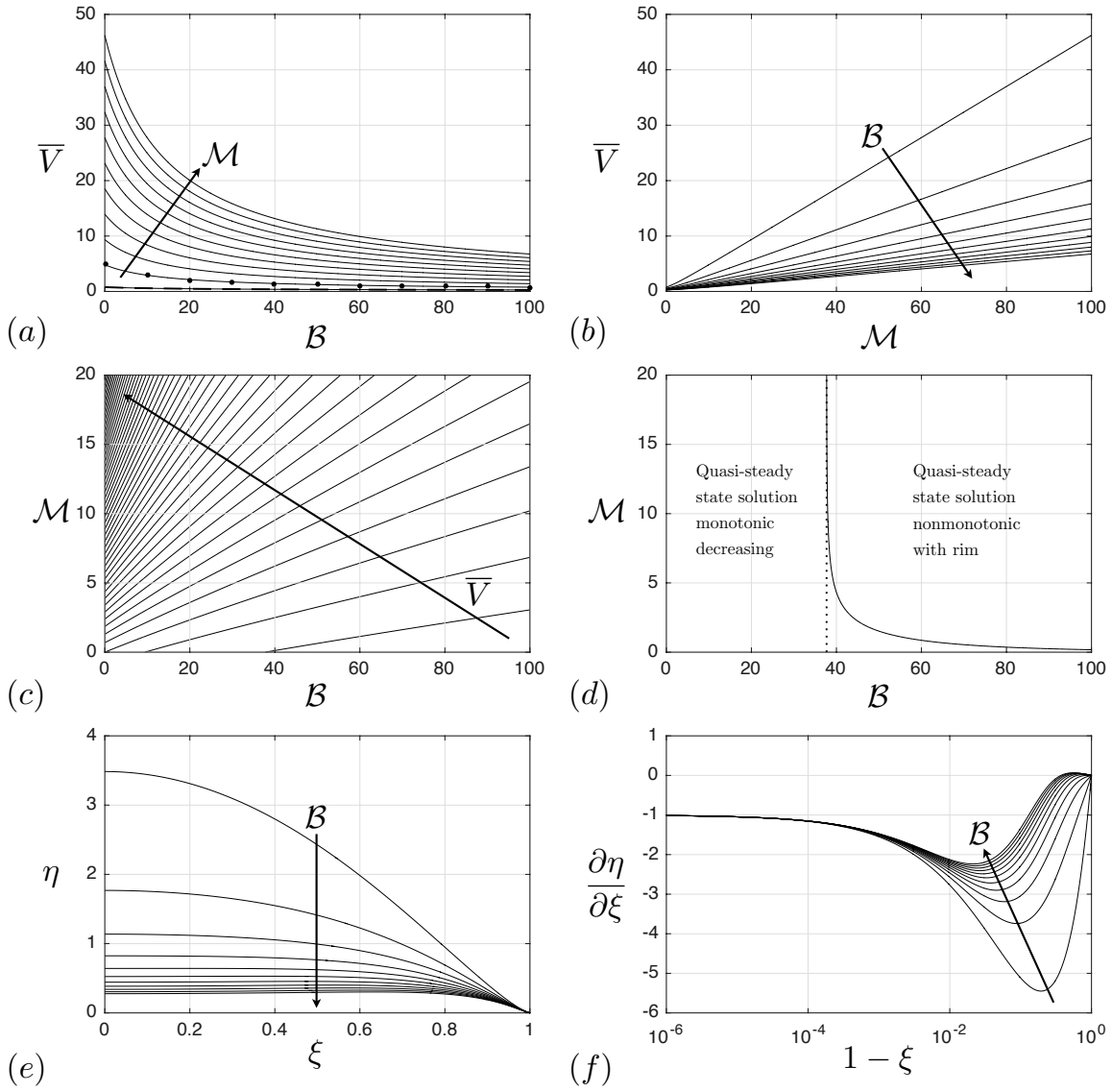

Figure 4.5: Numerical solution of the boundary-value problem (4.6), (4.8*a,b*) and (4.35), that determines the function $\overline{V}(\mathcal{B},\mathcal{M})$ via (4.36). (*a*) $\overline{V}$ as a function of $\mathcal{B}$ for $\mathcal{M} = 0, 10, \ldots, 100$. The dashed curve shows the exact solution (4.39) for $\mathcal{M} = 0$; the points correspond to the profiles shown in (*e,f*). (*b*) $\overline{V}$ as a function of $\mathcal{M}$ for $\mathcal{B} = 0, 10, \ldots, 100$. (*c*) Contours $16\overline{V}/\pi = 1, 2, \ldots$ plotted in $(\mathcal{B},\mathcal{M})$-space. (*d*) Regime diagram of $(\mathcal{B},\mathcal{M})$-space showing whether the quasi-steady drop profile is monotone-decreasing in ξ, or whether it is non-monotonic with a rim near the contact line. The dotted line is the critical value of the effective Bond number $\mathcal{B}$, below which the profile is monotone-decreasing for any value of $\mathcal{M}$. ((*e*) Drop profiles for $\mathcal{M} = 10$ and $\mathcal{B} = 0, 10, \ldots, 100$, corresponding to the points in (*a*). (*f*) Slope of the drop near the contact line, corresponding to the profiles in (*e*). We see that there is a slight rim near the contact line for sufficiently large $\mathcal{B}$ (with $\mathcal{M} = 10$).

by

$$V_R = \Phi_R(\mathcal{E}, n)\overline{V}\left(\mathrm{Bo}, \frac{\mathrm{Ma}}{\Phi_R(\mathcal{E}, n)}\right), \tag{4.42}$$

$$V_A = \Phi_A(\mathcal{E}, n, \Psi_H)\overline{V}\left(\mathrm{Bo}, \frac{\mathrm{Ma}}{\Phi_A(\mathcal{E}, n, \Psi_H)}\right). \tag{4.43}$$

Thirdly, we may write the expression for the steady state $\widehat{s}_0 = s_e$ in regime I (4.31) in terms of the function $\overline{V}$; we find that

$$V_* = \Phi_R\left(\frac{\mathcal{E}}{s_e^{1/2}}, n\right) s_e^3 \overline{V}\left(\mathrm{Bo}\, s_e^2, \frac{\mathrm{Ma}}{\Phi_R(\mathcal{E}/s_e^{1/2}, n)}\right). \tag{4.44}$$

Using our knowledge of the dependence of the functions Φ_R and $\overline{V}$ on their arguments, we deduce that, for given values of $(\mathcal{E}, \mathrm{Bo}, \mathrm{Ma}, n)$, V_* is a continuous, monotone-increasing function of s_e.

4.5.2 Evolution on the timescale of mass loss

The leading-order drop volume $V_0(T)$ at time T is given in terms of S_0 and Θ_0, and the function $\overline{V}$, by (4.37). We note that the leading-order version of the expression (2.25) representing global conservation of mass is given by

$$\frac{\mathrm{d}V_0}{\mathrm{d}T} = -2\pi S_0. \tag{4.45}$$

We begin with regime I ($V_C \leq V_* < V_R$), in which the contact line recedes to an equilibrium contact-set radius $s_e < 1$ on the timescale of contact-line motion. The leading-order-inner problem is the same as for the timescale of contact-line motion upon replacing $\widehat{s}_0$ with S_0. An intermediate region is not required on this timescale as direct matching of the outer and inner solutions gives

$$\Theta_0 = \Phi_R\left(\frac{\mathcal{E}}{S_0^{1/2}}, n\right). \tag{4.46}$$

Since the leading-order macroscopic contact angle is equal to the effective receding microscopic contact angle, the contact line begins to recede instantaneously at $T = 0$. This receding phase is analogous to the constant-contact-angle phase considered by Stauber *et al.* (2014), with the important difference that the contact angle (4.46) is not constant; rather, the contact angle increases with time as the contact-set radius decreases. If, however, $\mathcal{E} \ll 1$ as $\lambda \to 0$, then for the part of the motion for which $S_0 \gg \mathcal{E}^2$, the asymptote (4.20) for Φ_R tells us that the contact angle is constant to leading order in $\mathcal{E}$.

We substitute (4.46) into (4.37) to find that the leading-order drop volume V_0 is given in terms of the leading-order contact-set radius S_0 by

$$V_0 = \Phi_R\left(\frac{\mathcal{E}}{S_0^{1/2}}, n\right) S_0^3 \overline{V}\left(\mathrm{Bo}\, S_0^2, \frac{\mathrm{Ma}}{\Phi_R(\mathcal{E}/S_0^{1/2}, n)}\right). \tag{4.47}$$

By comparing (4.47) to (4.44), we see that $S_0 = \Sigma(V_0)$, where Σ is the same function that relates s_e to V_* in regime I. We may therefore write the conservation-of-mass equation (4.45) as an ordinary differential equation for V_0, given by

$$\frac{\mathrm{d}V_0}{\mathrm{d}T} = -2\pi\Sigma(V_0). \tag{4.48}$$

Matching with the timescale of contact-line motion gives the initial condition

$$V_0(0) = V_*. \tag{4.49}$$

We integrate (4.48) subject to (4.49) to find that the leading-order drop volume $V_0(T)$ at time T is given by

$$T = \frac{1}{2\pi}\int_{V_0(T)}^{V_*} \frac{\mathrm{d}v}{\Sigma(v)} \quad \text{for } 0 \le T \le T_e, \tag{4.50}$$

where T_e is the extinction time of the drop, given by

$$T_e = \frac{1}{2\pi}\int_0^{V_*} \frac{\mathrm{d}v}{\Sigma(v)}. \tag{4.51}$$

We now consider regime II ($V_R \le V_* \le V_A$), in which the contact line was pinned at an equilibrium contact-set radius $s_e = 1$ throughout the timescale of contact-line motion, together with regime III ($V_* > V_A$), in which the contact line advances to an equilibrium contact-set radius $s_e > 1$ on the timescale of contact-line motion. In the borderline case $V_* = V_R$, we have $\Theta_0(0) = \Phi_R(\mathcal{E}, n)$ and the evolution proceeds as described above for regime I. Otherwise, we have $\Theta_0(0) > \Phi_R(\mathcal{E}, n)$ so that we are initially in a pinned phase with $S_0(T) = s_e$. This pinned phase is analogous to the constant-contact-radius phase considered by Stauber *et al.* (2014). During this pinned phase, the macroscopic contact angle Θ_0 decreases monotonically with T until it reaches the receding microscopic contact angle $\Phi_R(\mathcal{E}, n)$ at some finite time T_d, at which time the drop de-pins. Simultaneously, the microscopic contact angle Ψ_0 decreases from the value it had on the timescale of contact-line motion to 1 (its receding value). Matching with the timescale of contact-line motion gives $V_0(0) = V_*$. We then deduce from (4.45) that the drop volume evolves according to

$$V_0 = V_* - 2\pi s_e T \quad \text{for } 0 \le T \le T_d. \tag{4.52}$$

From (4.37) and (4.52) we deduce that the de-pinning time T_d is given by

$$T_d = \frac{V_* - V_d}{2\pi s_e}, \quad V_d = \Phi_R\left(\frac{\mathcal{E}}{s_e^{1/2}}, n\right) s_e^3 \overline{V}\left(\mathrm{Bo}\, s_e^2, \frac{\mathrm{Ma}}{\Phi_R(\mathcal{E}/s_e^{1/2}, n)}\right), \qquad (4.53a, b)$$

where V_d is the volume at which the drop de-pins. We note that in regime II, where $s_e = 1$, we have $V_d = V_R$ and this expression simplifies to $T_d = (V_* - V_R)/2\pi$.

For $T > T_d$, the contact line recedes with the evolution of V_0 governed by the global conservation of mass equation (4.48), but with the initial condition (4.49) replaced by the condition

$$V_0(T_d) = V_d. \qquad (4.54)$$

Thus, the expression (4.50) is replaced by

$$T = T_d + \frac{1}{2\pi}\int_{V_0(T)}^{V_d} \frac{\mathrm{d}v}{\Sigma(v)} \quad \text{for } T_d < T \leq T_e, \qquad (4.55)$$

with T_d given by (4.53) and the extinction time T_e given by

$$T_e = T_d + \frac{1}{2\pi}\int_{0}^{V_d} \frac{\mathrm{d}v}{\Sigma(v)}. \qquad (4.56)$$

We determine numerically the evolution of the leading-order contact-set radius and drop volume on the timescale of mass loss as follows. For given values of $(\mathcal{E}, \mathrm{Bo}, \mathrm{Ma}, n)$, we create a lookup table for the function Σ by calculating the value of V_0 that satisfies (4.47) for several values of S_0 (using lookup tables for Φ_R and $\overline{V}$). We prescribe a range of values $V_0 \in (0, V_*]$. We then evaluate numerically the integral (4.50) in regime I, or (4.55) in regimes II and III to find the corresponding values of T (using the lookup table for Σ, spline interpolation and the function `integral` in MATLAB with sufficiently small error tolerances to resolve the integrable singularity at $v = 0$). Finally, the relationship $S_0 = \Sigma(V_0)$ is used to determine the corresponding values of S_0.

The evolution on the timescale of mass loss of the leading-order drop volume V_0, contact-set radius S_0, macroscopic contact angle Θ_0, and microscopic contact angle Ψ_0 is illustrated in figure 4.6(a–d) for $\mathrm{Bo} = 1$, $\mathrm{Ma} = 1$, $\mathcal{E} = 1$, $n = 1$, and $\Psi_H = 4$, for initial volumes $V_* = 1, 2, \ldots, 10$. We see that V_0 decreases linearly with time T in the pinned phase, and then continues to decrease monotonically, but at a slower rate, in the receding phase until the drop goes extinct. We see that S_0 is constant in the pinned phase and then decreases monotonically with time in the receding phase until the drop goes extinct. We see that Θ_0 decreases monotonically with time in

the pinned phase but then increases monotonically with time in the receding phase, blowing up close to extinction. We see that Ψ_0 decreases monotonically with time in the pinned phase until it is equal to 1 (the dimensionless receding microscopic contact angle) and then remains equal to 1 in the receding phase until the drop goes extinct.

In figure 4.6(e), we plot the dependence of the de-pinning time T_d and extinction time T_e on the initial volume V_* for the same example set of parameters as above. We shall investigate the dependence of T_d and T_e on the parameters in our model more thoroughly in §4.7. In figure 4.6(f), we plot the evolution of the contact-set radius S_0 at times close to extinction for the same example set of parameters. It appears that a $d^{13/7}$-law is valid close to extinction; we shall investigate this behaviour in §4.8.

4.6 Comparison to finite-element simulations

The full thin-film problem (2.18), (2.19), (2.21) and (2.24) may be solved numerically using a finite-element method, as described in appendix 2.A. In figure 4.7, we compare the results of our finite-element simulations to the leading-order asymptotic predictions for $\lambda = 10^{-4}$, $\alpha = (\lambda/2)^{1/2}$ (so that $\mathcal{E} = 1$), Bo $= 1$, Ma $= 1$, $\Psi_H = 4$, and $V_* = 1, 3, 6$ (in regimes I, II and III, respectively). In the initial condition for the finite-element method (see appendix 2.A), we take $\Psi_* = 3$.

In figure 4.7(a), we see very good agreement between the finite-element simulations and the leading-order asymptotic prediction for the drop volume V; the asymptotic prediction for V is the leading-order solution on the timescale of mass loss, namely V_0 (since the drop volume does not change on the earlier timescales). In figure 4.7(b), we see good agreement between the finite-element simulations and the leading-order asymptotic prediction for the contact-set radius s; the asymptotic prediction for s is a leading-order composite expansion of the solutions on the timescales of contact-line motion, $\widehat{s}_0$, and mass loss, S_0 (since the contact-set radius does not change on the timescale of capillary action). For $V_* = 1$, the agreement is less good on earlier timescales; this is consistent with the error in our asymptotic analysis being of size $\mathrm{O}(1/\log(1/\lambda))$. The agreement between the finite-element solution and the leading-order asymptotic predictions gives us confidence that our asymptotic results are correct.

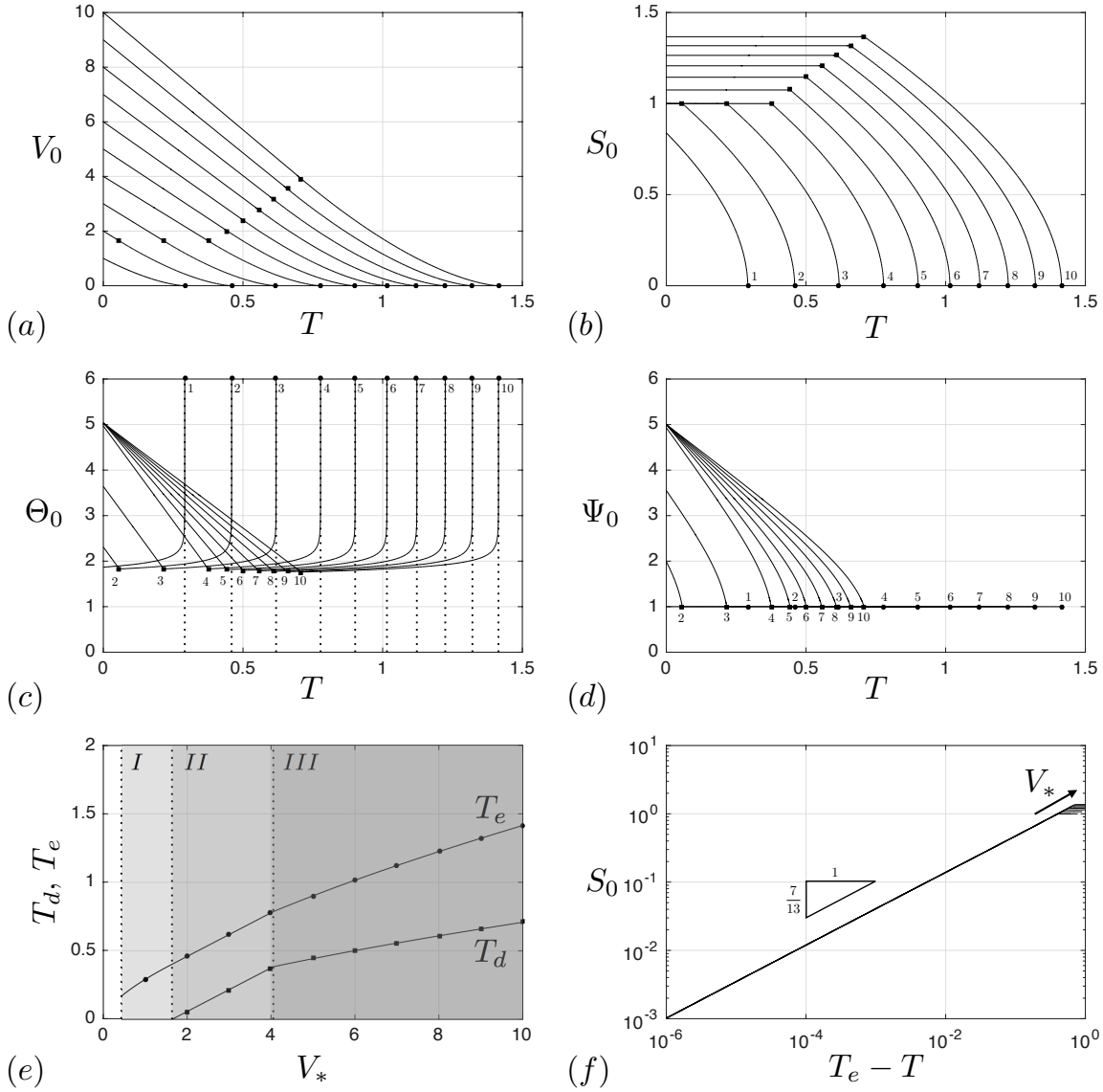

Figure 4.6: Evolution of the drop on the timescale of mass loss, determined numerically as described at the end of §4.5, for Bo = 1, Ma = 1, $\mathcal{E} = 1$, $n = 1$, $\Psi_H = 4$, and $V_* = 1, 2, \ldots, 10$. In (*a*–*d*), we plot the evolution of the leading-order drop volume V_0, leading-order contact-set radius S_0, leading-order macroscopic contact angle Θ_0, and leading-order microscopic contact angle Ψ_0. The solid squares correspond to the point at which the drop de-pins and enters the receding phase (in regimes II and III), while the solid circles correspond to the point at which the drop has fully evaporated. Where shown, numbers next to the squares and circles give the value of V_*. In (*e*), we plot the time T_d when the drop de-pins and the time T_e when the drop has fully evaporated as functions of the initial drop volume V_*. The squares and circles correspond to those in the other plots. In (*f*), we plot S_0 as a function of the time remaining until the drop has fully evaporated ($T_e - T$). For small values of ($T_e - T$), we see that the drop obeys a $d^{13/7}$-law in this parameter regime.

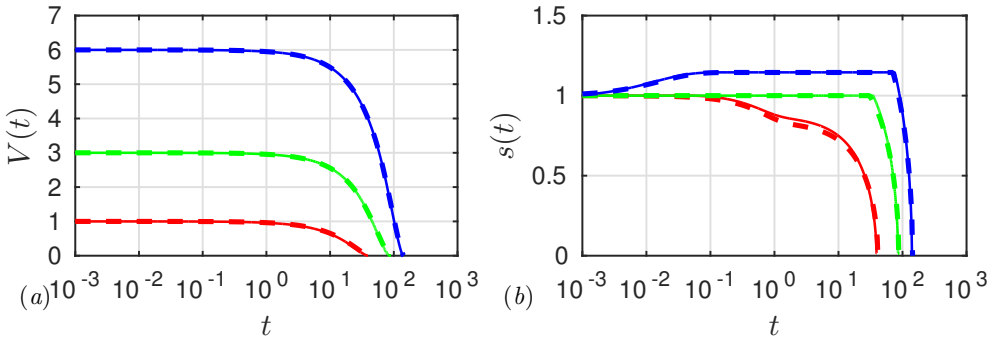

Figure 4.7: Comparison of the leading-order asymptotics with finite-element simulations for $\lambda = 10^{-4}$, α chosen such that $\mathcal{E} = 1$, Bo $= 1$, Ma $= 1$, $\Psi_H = 4$, and $V_* = 1, 3, 6$ (red, green, and blue curves, respectively, corresponding to regimes I, II, and III), with $\Psi_* = 3$. (a) Evolution of the drop volume V. (b) Evolution of the contact-set radius s. The solid curves are the finite-element solution, while the dashed curves are a leading-order composite expansion of the asymptotic solution over the three timescales. We see good agreement between the two solutions, especially for $V_* = 3, 6$.

4.7 Dependence of s_e, T_d, and T_e on parameters

Having validated our leading-order asymptotic predictions against numerical simulations, we now perform a parameter sweep to determine how the equilibrium contact-set radius s_e, de-pinning time T_d, and extinction time T_e depend on the Bond number Bo, Marangoni number Ma, evaporation rate $\mathcal{E}$, and hysteresis Ψ_H. We recall that the equilibrium contact-set radius s_e is given by (4.32) in regime I (in which the contact line recedes on the timescale of contact-line motion), $s_e = 1$ in regime II (in which the contact line is pinned on the timescale of contact-line motion), and s_e is given by (4.33) in regime III (in which the contact line advances on the timescale of contact-line motion). The de-pinning time T_d is given by (4.53) in regimes II and III; in regime I, the contact line begins to recede instantaneously at $T = 0$. The extinction time T_e is given by (4.51) in regime I and by (4.56) in regimes II and III.

In figure 4.8, we plot s_e, T_d, and T_e, as functions of the initial drop volume V_* (for $V_* \geq V_C$). The two solid squares on each of the T_d-curves mark the values $V_* = V_R, V_A$. The three solid circles on each of the T_e-curves mark the values $V_* = V_C, V_R, V_A$. In all plots we take Bo $= 1$, Ma $= 1$, $\mathcal{E} = 1$, $n = 1$ and $\Psi_H = 4$ (white dashed curves), except that in (i) we vary Bo, (ii) we vary Ma, (iii) we vary $\mathcal{E}$, and (iv) we vary Ψ_H (note that variations in Ψ_H will only affect regime III), with the varying parameter taking values $0, 1, \ldots, 10$. We note that this range of parameter values is only a subset

of the physically realistic ones (see table 2.3), but it is likely that the trends we find here continue for larger values of the parameters.

In regime I (in which the contact line recedes on the timescale of contact-line motion), varying Ψ_H does not affect any of the variables; varying Bo has a very small effect on s_e, T_d and T_e; varying $\mathcal{E}$ has a slightly larger effect; varying Ma has the largest effect, and we note that another significant effect of varying Ma is to vary V_C and thus the range of initial volumes that correspond to regime I. In regime II (in which the contact line is pinned on the timescale of contact-line motion), $s_e \equiv 1$ and is unaffected by varying any of the parameters; the sensitivity of T_d and T_e to parameter variations is similar to regime I. In regime III (in which the contact line advances on the timescale of contact-line motion), s_e varies only very slightly with $\mathcal{E}$, significantly with Bo and Ma, and very significantly with Ψ_H; T_d varies only very slightly with Bo, significantly with Ma and $\mathcal{E}$, and very significantly with Ψ_H; T_e varies slightly with Bo and $\mathcal{E}$, and significantly with Ma and Ψ_H.

The de-pinning time T_d in regime II is a decreasing function of the critical volume V_R, which is the volume at which the drop de-pins in regime II, and so the trends in T_d may be understood from the trends in V_R (see discussion at end of §4.3). In regime III, things are more complicated due to the dependence of T_d on the equilibrium contact-set radius s_e, which is the radius at which the drop is pinned in regime III. To explain the trends in T_d in regime III, it is necessary to consider how sensitively s_e depends on the parameters as well as how sensitive the function $\overline{V}$ is to variations in its argument; we do not investigate this point further here.

The dependence of the extinction time T_e on the parameters appears to be a direct consequence of how the equilibrium contact-set radius s_e achieved on the timescale of contact-line motion depends on the parameters. Since the total mass flux out of the drop per unit time is proportional to the contact-set radius, if s_e is larger for a given initial drop volume V_* then the drop initially evaporates more quickly and T_e is therefore smaller. As the Bond number Bo increases, the centre of the drop becomes flatter and thus s_e is greater for given V_*. Thus, T_e decreases with Bo. As the Marangoni number Ma increases, the Marangoni flow pulls liquid away from the contact line so that s_e decreases. Thus, T_e increases with Ma. As the evaporation rate $\mathcal{E}$ in the inner region increases, so does the effective microscopic contact angle (since, loosely speaking, the singularity in the mass flux pulls the contact line toward the liquid in a manner that increases with the evaporation rate), and consequently s_e decreases for given V_*. Thus, T_e increases with $\mathcal{E}$. As the contact-angle hysteresis Ψ_H increases, the initial volume required to enter regime III (in which the contact

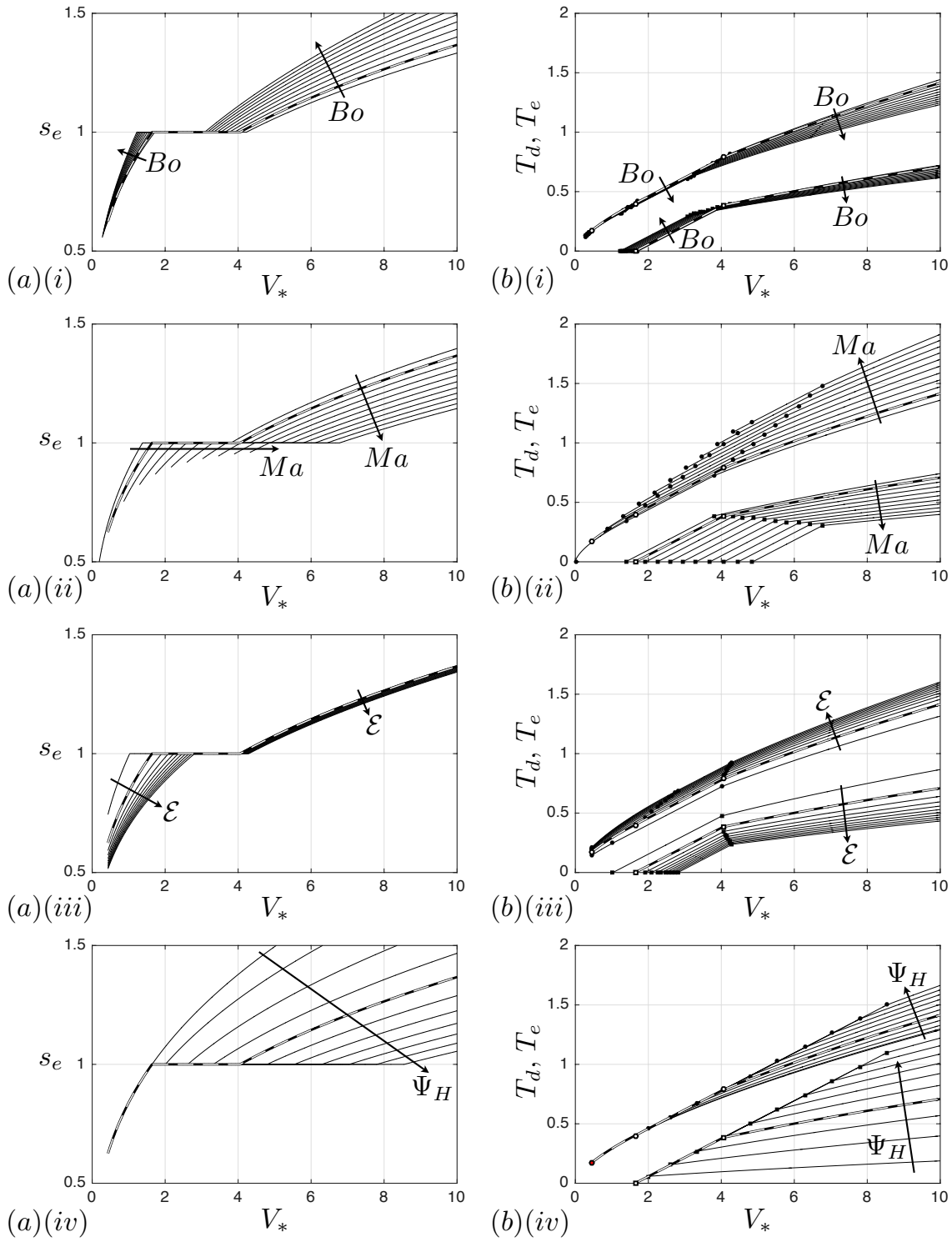

Figure 4.8: Dependence of the equilibrium contact-set radius s_e, de-pinning time T_d, and extinction time T_e ($T_d < T_e$) on the parameters in the model. Details in text (§4.7).

line advances) increases, so that s_e decreases. Thus, T_e increases with Ψ_H. We have therefore answered our key question of how the extinction time depends on the parameters in our model.

4.8 Behaviour close to extinction

4.8.1 $\mathrm{Bo}, \mathrm{Ma}, \mathcal{E} = \mathrm{O}(1)$

Let us first consider the case in which $\mathrm{Bo}, \mathrm{Ma}, \mathcal{E} = \mathrm{O}(1)$. Recall that once the drop has de-pinned, the leading-order drop volume V_0 is given by (4.47), which depends on the functions Φ_R and $\overline{V}$. Close to extinction, $S_0 \to 0^+$. Thus, the first argument of Φ_R, namely $\mathcal{E}/S_0^{1/2}$, is large and we may use the asymptote (4.21) for Φ_R. Also, the first argument of $\overline{V}$, namely $\mathrm{Bo}\, S_0^2$, is small. Since Φ_R is large according to (4.21), the second argument of $\overline{V}$, namely $\mathrm{Ma}/\Phi_R(\mathcal{E}/S_0^{1/2}, n)$, is also small; we may therefore use the asymptote (4.40) for $\overline{V}$. The asymptotes (4.21) and (4.40) tell us that

$$V_0 \sim \frac{\pi \Phi_\infty(n) \mathcal{E}^{2/7}}{4} S_0^{20/7} \quad \text{as } S_0 \to 0^+. \tag{4.57}$$

We then deduce from the global conservation of mass equation (4.45) that

$$S_0 \sim A(T_e - T)^{7/13} \quad \text{as } T \to T_e^-, \tag{4.58}$$

where the coefficient A is given in terms of $\Phi_\infty(n)$ and $\mathcal{E}$ by

$$A = \left(\frac{26}{5\Phi_\infty(n)} \right)^{7/13} \mathcal{E}^{-2/13}. \tag{4.59}$$

Equation (4.58) tells us that in this case, a $d^{13/7}$-law is appropriate close to extinction. This near-extinction behaviour is illustrated in figure 4.6(f). In chapter 3, we showed that a $d^{13/7}$-law was valid when $\mathcal{E} = \mathrm{O}(1)$ and $\mathrm{Bo} = \mathrm{Ma} = 0$. We have now shown that the criterion $\mathcal{E} = \mathrm{O}(1)$ is still the relevant one for this behaviour provided $\mathrm{Bo}, \mathrm{Ma} = \mathrm{O}(1)$.

We note that the asymptotes (4.21) and (4.40) are valid provided $S_0 \ll \mathcal{E}^2, \mathrm{Bo}^{-1/2}$. This means that $d^{13/7}$-behaviour still occurs in a temporal boundary layer close to extinction if any of Bo, Ma, and $\mathcal{E}$ are small.

4.8.2 $\mathrm{Bo}, \mathrm{Ma}, \mathcal{E} \ll 1$

Another case where we can progress is the situation in which $\mathrm{Bo}, \mathrm{Ma}, \mathcal{E} \ll 1$. From the start of the receding phase, while $S_0 \gg \mathcal{E}^2$, $\mathcal{E}/S_0^{1/2}$ is small and so we may use

the asymptote (4.20) for Φ_R. Throughout the receding phase, $\mathrm{Bo}\, S_0^2$ is small. At the start of the receding phase, (4.20) tells us that $\Phi_R = \mathrm{O}(1)$ and so $\mathrm{Ma}/\Phi_R(\mathcal{E}/S_0^{1/2}, n)$ is small; we may therefore use the asymptote (4.40) for $\overline{V}$. The asymptotes (4.20) and (4.40) tell us that

$$V_0 \sim \frac{\pi}{4} S_0^3 \quad \text{as } \mathrm{Bo}, \mathrm{Ma}, \mathcal{E} \to 0. \tag{4.60}$$

This implies that

$$S_0 \sim \frac{4}{\sqrt{3}} (T_e - T)^{1/2} \quad \text{as } \mathrm{Bo}, \mathrm{Ma}, \mathcal{E} \to 0. \tag{4.61}$$

Since (4.61) is valid from the start of the receding phase, we may use the condition $S_0(T_d) = s_e$ (where we define $T_d = 0$ if the contact line recedes instantaneously at $T = 0$) to deduce that

$$T_e \sim T_d + \frac{3}{16} s_e^2 \quad \text{as } \mathrm{Bo}, \mathrm{Ma}, \mathcal{E} \to 0. \tag{4.62}$$

Equation (4.61) tells us that in this distinguished limit, a d^2-law is appropriate from the start of the receding phase. We note that once $S_0 \ll \mathcal{E}^2$, the drop would transition to the $d^{13/7}$-behaviour (4.61). If Bo is not small, but $\mathrm{Bo} \ll \mathcal{E}^{-4}$, then the d^2-behaviour (4.61) holds in a temporal region where $\mathcal{E}^2 \ll S_0 \ll \mathrm{Bo}^{-1/2}$ (in which $\mathrm{Bo}\, S_0^2$ is small). In chapter 3, we showed that a d^2-law was valid, except in a temporal boundary layer close to extinction, when $\mathcal{E} \ll 1$ and $\mathrm{Bo} = \mathrm{Ma} = 0$. We have now shown that the criterion $\mathcal{E} \ll 1$ is still the relevant one for this behaviour provided $\mathrm{Bo} \ll \mathcal{E}^{-4}$ and $\mathrm{Ma} \ll 1$.

4.9 Summary

Our aim in this chapter was to analyse the dynamic evaporation of a liquid drop on a smooth, impermeable substrate. In particular, we considered the question of how the extinction time of the drop depends on evaporation, gravity, surface-tension gradients and contact-angle hysteresis. We exploited the smallness of the slip coefficient to perform a systematic asymptotic analysis. We considered the distinguished limit in which the effects of mass loss enter the inner region to leading order in the limit of small slip (but not the outer or intermediate regions), and the Bond and Marangoni numbers are of order-unity size. The temporal and spatial asymptotic structure of the problem was found to be the same as in chapter 3.

In §4.3, we considered the timescale of capillary action. On this timescale, mass is conserved and the contact line does not move to leading order in the slip coefficient λ. We found that there is a critical effective Marangoni number with a corresponding

critical value of the initial drop volume, $V_* = V_C$. For $V_* < V_C$, our numerical simulations suggested that the drop profile touches down in the interior of the contact set at some finite time. We did not investigate further what happens after the drop profile loses positivity. For $V_* \geq V_C$, the drop evolves to a steady-state profile that is different to the usual spherical cap shape due to the effects of gravity and surface-tension gradients (Tsoumpas *et al.*, 2015). We also found that the drop has an effective microscopic contact angle that depends on the evaporation rate in the inner region, as in chapter 3.

In §4.4, we considered the timescale of contact-line motion; we found that the contact line moves an order-unity distance on the same timescale as in chapter 3. On this timescale, mass is again conserved to leading order. We found that there are three distinct evolution regimes, depending on whether the contact line is initially receding, pinned or advancing. We identified critical initial drop volumes $V_* = V_R, V_A$ corresponding to the initial macroscopic contact angle being equal to the receding and advancing effective microscopic contact angles, respectively. For $V_C \leq V_* < V_R$, which we refer to as regime I, the contact line recedes according to Tanner's law, but with the microscopic contact angle replaced by the effective receding microscopic angle. The drop evolves to a steady state in which the macroscopic contact angle is equal to the effective microscopic contact angle. For $V_R \leq V_* \leq V_A$, which we refer to as regime II, the contact line is pinned to leading order throughout the timescale of contact-line motion. For $V_* > V_A$, which we refer to as regime III, the contact line advances according to Tanner's law, but with the microscopic contact angle replaced by the effective advancing microscopic angle. The drop evolves to a steady state in which the macroscopic contact angle is equal to the effective microscopic contact angle. Thus, in all three regimes, the leading-order contact-set radius reaches an equilibrium on this timescale.

In §4.5, we considered the timescale of mass loss, on which the drop begins to lose an order-unity amount of mass. In regime I, the contact line begins to recede instantaneously and the leading-order drop volume and contact-set radius both decrease monotonically to zero with the leading-order macroscopic contact angle equal to the effective receding microscopic contact angle. This is analogous to the 'constant contact angle' phase observed by, for example, Stauber *et al.* (2014), except that the effective receding microscopic contact angle depends on the contact-set radius. In regimes II and III, the drop initially loses mass in a pinned phase, with its radius equal to the equilibrium one reached on the timescale of contact-line motion. The leading-order macroscopic contact angle decreases monotonically from its initial value

to the effective receding microscopic contact angle. This is analogous to the 'constant contact radius' phase observed by, for example, Stauber *et al.* (2014). Once the macroscopic contact angle reaches the effective receding microscopic contact angle, the drop de-pins and evolves as in regime I.

In §4.6, we compared our leading-order asymptotic results with results generated by numerical solutions of the full thin-film problem, obtained using a finite-element method. Good agreement was found for a range of physically relevant parameter values, giving us confidence in our asymptotic predictions.

In §4.7, we analysed how the equilibrium contact-set radius, de-pinning time, and extinction time depend on the parameters in our model. We found that the equilibrium contact-set radius increases with the Bond number Bo, decreases with the Marangoni number Ma, decreases slightly with the evaporation rate $\mathcal{E}$, and decreases significantly with the hysteresis Ψ_H. We found that the de-pinning time increases slightly with Bo in regime II but decreases slightly with Bo in regime III, decreases with Ma, decreases with $\mathcal{E}$, and increases significantly with Ψ_H. We found that the extinction time decreases slightly with Bo, increases with Ma, increases slightly with $\mathcal{E}$, and increases with Ψ_H; this answers our key question for this chapter.

In §4.8, we analysed the behaviour of the contact-set radius close to extinction. We found that the classical d^2-law is achieved when $\mathcal{E} \ll 1$, provided that $\mathrm{Bo} \ll \mathcal{E}^{-4}$ and $\mathrm{Ma} \ll 1$, but that a $d^{13/7}$-law is appropriate instead when $\mathcal{E} = \mathrm{O}(1)$, provided that $\mathrm{Bo}, \mathrm{Ma} = \mathrm{O}(1)$. This generalizes the results of chapter 3, where we found that for $\mathrm{Bo} = \mathrm{Ma} = 0$, a d^2-law is valid when $\mathcal{E} \ll 1$ and a $d^{13/7}$-law is valid when $\mathcal{E} = \mathrm{O}(1)$.

The inverse-square-root singularity in the evaporative flux at the contact line was not regularized in chapters 2–4, since the resulting predictions for the drop volume and contact-set radius are well-behaved. However, we do obtain a singularity in the depth-averaged radial velocity at the contact line:

$$\overline{u} \sim \frac{2^{1/2}\alpha}{\Psi s^{1/2}(s-r)^{1/2}} \quad \text{as } r \to s(t)^{-}. \tag{4.63}$$

This is needed to supply the diverging evaporative flux at the contact line, but it is not physical. It would be informative to analyse a model in which this singularity is regularized and in particular to investigate what effect, if any, such a regularization has on the near-extinction behaviour. The aim of the next chapter will be to obtain an explicit expression for the evaporation rate of a kinetics-based model that does not have a mass-flux singularity at the contact line, and to investigate the way in which the singularity is regularized.

4.A Numerical solution of the boundary-value problems for $\overline{\theta}(\mathcal{B},\mathcal{M})$ and $\overline{V}(\mathcal{B},\mathcal{M})$

To solve the boundary-value problem (4.6) and (4.8*a–c*) numerically, and determine $\overline{\theta}(\mathcal{B},\mathcal{M})$ via (4.9), we may use the following regularization method. The corresponding code was written by Prof. James Oliver. We replace the thin-film equation (4.6) by

$$(\varepsilon+\eta)\frac{\mathrm{d}}{\mathrm{d}\xi}\left(\frac{\mathrm{d}^2\eta}{\mathrm{d}\xi^2}+\frac{1}{\xi}\frac{\mathrm{d}\eta}{\mathrm{d}\xi}-\mathcal{B}\eta\right)+\mathcal{M}\frac{\mathrm{d}}{\mathrm{d}\xi}\left(\frac{\varepsilon+\eta}{\sqrt{1+\varepsilon-\xi^2}}\right)=0 \quad \text{for } 0<\xi<1, \tag{4.64}$$

with $0<\varepsilon\ll 1$. The regularized problem is readily solved using the function `bvp5c` in MATLAB. We use the exact solution (4.10) for $\mathcal{M}=0$ as an initial guess and then decrease ε until the prediction for $\overline{\theta}$, obtained using (4.9), has converged ($\varepsilon=10^{-8}$ was sufficiently small for $\mathcal{B},\mathcal{M}\leq 100$). We then use continuation in $\mathcal{M}$, employing a non-uniform grid in $\mathcal{M}$ to resolve the rapid variation in $\overline{\theta}$ as it tends to zero. The dependence of $\overline{\theta}(\mathcal{B},\mathcal{M})$ on its arguments is illustrated in figure 4.1(*a,b*).

An alternative method of solution is the following truncation method. The corresponding code was written by Prof. James Oliver. We truncate the domain and solve for the degrees of freedom in the local expansions at $\xi=0^+$ and $\xi=1^-$. We find that a large number of terms in the local expansions are required to obtain accurate solutions using this method, especially for small values of $\overline{\theta}$ (this is because the local expansion at $\xi=1^-$ becomes non-uniform as $\overline{\theta}\to 0^+$). When the relaxation method and truncation method both converged, they were in excellent agreement with each other and with the exact solutions.

To solve the boundary-value problem (4.6), (4.8*a,b*) and (4.35) numerically, and determine $\overline{V}(\mathcal{B},\mathcal{M})$ via (4.36), we could again regularize the problem by replacing (4.6) with (4.64) and then use continuation in ε and $\mathcal{M}$ to solve (4.64), (4.8*a,b*) and (4.35) for $\mathcal{M}>0$. However, in this case we found that accurate solutions were obtained more rapidly by using the truncation method described above. Simulations suggest that the solution exists for all $\mathcal{M}>0$, in contrast to the timescale of contact-line motion — this is presumably because the volume may now adjust to satisfy the condition (4.35) on the macroscopic contact angle. The dependence of $\overline{V}(\mathcal{B},\mathcal{M})$ on its arguments is illustrated in figure 4.5(*a,b*).

The relaxation method for the $\overline{\theta}$-problem was used to produce figures 4.1(*a,b,e,f*) and 4.4(*a*), as well as for the rim/no-rim transition curves in figures 4.1(*c*) and 4.5(*d*). It was easier to produce the illustrative plots in figure 4.1 (which weren't used to

solve for the evolution on the timescale of contact-line motion) using the relaxation method as it works even for $\overline{\theta} = 0$: in fact, we prescribed $\overline{\theta}$ and solved for $\mathcal{M}$ in figures 4.1(a,b). The truncation method for the $\overline{V}$-problem was used for the remainder of the figures including the ones for the timescale of contact-line motion (via the relationship between (4.38) between $\overline{\theta}$ and $\overline{V}$). The critical Marangoni number curve was found as described in appendix 4.B, using Richardson extrapolation with $\mathcal{M} = 1000, 2000$ to fit $\overline{V}_0, \overline{V}_1$ for $\mathcal{B} = 0, 0.1, 0.2, \ldots, 100$. In figure 4.4($a$), the thin $\widehat{s}_0$-curves are from the relaxation method, while the wider lines with arrows showing the evolution are from the truncation method, illustrating excellent visual agreement between the two methods.

4.B Asymptotic analysis of the mass-loss boundary-value problem

In this appendix, we perform an asymptotic analysis of the boundary-value problem (4.6), (4.8a,b) and (4.35) that determines the function $\overline{V}(\mathcal{B}, \mathcal{M})$ via (4.36). We then use the relationship (4.38) to deduce asymptotes for the function $\overline{\theta}(\mathcal{B}, \mathcal{M})$.

4.B.1 $\mathcal{B} \to \infty$ with $\mathcal{M} = \mathrm{O}(1)$

In this parameter sub-limit, the asymptotic structure consists of an inner region in which capillarity balances gravity and an outer region where $\xi = \mathrm{O}(1)$ (Hocking, 1983). In the inner region, in order to impose a finite contact angle and balance the effects of capillarity and gravity, we set $\widehat{\xi} = \mathcal{B}^{1/2}(1-\xi)$ and expand $\eta \sim \mathcal{B}^{-1/2}\widehat{\eta}_0(\widehat{\xi})$ as $\mathcal{B} \to \infty$. We find that the leading-order-inner solution is simply given by $\widehat{\eta}_0 = 1 - e^{-\widehat{\xi}}$. In the outer region, we expand $\eta \sim \mathcal{B}^{-1/2}\eta_0(\xi)$ as $\mathcal{B} \to \infty$. Gravity dominates and we find that $\eta_0 \equiv 1$ to match with the inner region. We deduce that

$$\overline{V}(\mathcal{B}, \mathcal{M}) \sim \frac{\pi}{\mathcal{B}^{1/2}} \quad \text{as } \mathcal{B} \to \infty \text{ with } \mathcal{M} = \mathrm{O}(1). \tag{4.65}$$

4.B.2 $\mathcal{M} \to \infty$ with $\mathcal{B} = \mathrm{O}(1)$

In this parameter sub-limit, the asymptotic structure consists of an outer region where the effects of capillarity, gravity and surface-tension gradients all balance and an inner region where capillarity balances surface-tension gradients. In the outer region, we expand

$$\eta \sim \mathcal{M}\eta_0 + \mathcal{M}^{1-\beta}\eta_1, \quad \overline{V}(\mathcal{B}, \mathcal{M}) \sim \mathcal{M}\overline{V}_0(\mathcal{B}) + \mathcal{M}^{1-\beta}\overline{V}_1(\mathcal{B}), \tag{4.66a, b}$$

as $\mathcal{M} \to \infty$ with $\mathcal{B} = \mathrm{O}(1)$, with $\beta > 0$ to be determined. At $\mathrm{O}(\mathcal{M})$, we find that η_0 satisfies the same thin-film equation (4.6) as η, but with $\mathcal{M} = 1$. This is to be solved subject to the conditions

$$\frac{\mathrm{d}\eta_0}{\mathrm{d}\xi} = 0 \text{ at } \xi = 0; \quad \eta_0 = 0, \ \frac{\mathrm{d}\eta_0}{\mathrm{d}\xi} = 0 \quad \text{as } \xi \to 1^-. \tag{4.67a-c}$$

We note that scaling η_0 with $1/\mathcal{M}_c(\mathcal{B})$ in the leading-order-outer problem gives the problem for the critical Marangoni number. A local analysis near the contact line gives the matching condition

$$\eta_0 \sim \frac{2^{5/2}}{3}(1-\xi)^{3/2} \quad \text{as } \xi \to 1^-. \tag{4.68}$$

In the inner region, in order to impose a finite contact angle and match with the leading-order-outer problem, we set $\widehat{\xi} = \mathcal{M}^2(1-\xi)$ and expand $\eta \sim \mathcal{M}^{-2}\widehat{\eta}_0(\widehat{\xi})$ as $\mathcal{M} \to \infty$. Thus, the contribution to the volume of the drop from the inner region is smaller than that from the outer region. We deduce that

$$\overline{V}_0(\mathcal{B}) = 2\pi \int_0^1 \xi\eta_0(\xi)\,\mathrm{d}\xi = \frac{1}{\mathcal{M}_c(\mathcal{B})}. \tag{4.69}$$

To leading-order in the inner region, after integrating once with respect to $\widehat{\xi}$, we find that $\widehat{\eta}_0$ satisfies the thin-film equation given by

$$\widehat{\eta}_0\frac{\mathrm{d}^2\widehat{\eta}_0}{\mathrm{d}\widehat{\xi}^{\,2}} - \frac{1}{2}\left(\frac{\mathrm{d}\widehat{\eta}_0}{\mathrm{d}\widehat{\xi}}\right)^2 + \frac{\widehat{\eta}_0}{(2\widehat{\xi}\,)^{1/2}} = -\frac{1}{2} \quad \text{for } \widehat{\xi} > 0. \tag{4.70}$$

This is to be solved subject to the conditions

$$\widehat{\eta}_0 = 0, \ \frac{\mathrm{d}\widehat{\eta}_0}{\mathrm{d}\widehat{\xi}} = 1 \text{ at } \widehat{\xi} = 0^+; \quad \widehat{\eta}_0 \sim \frac{2^{5/2}}{3}\widehat{\xi}^{3/2} \text{ as } \widehat{\xi} \to \infty. \tag{4.71a-c}$$

A local and far-field analysis of (4.70) and (4.71) reveals that

$$\widehat{\eta}_0 \sim \begin{cases} \widehat{\xi} + \dfrac{2^{3/2}}{3}\widehat{\xi}^{3/2} - \dfrac{1}{6}\widehat{\xi}^2\log\widehat{\xi} + A_1\widehat{\xi}^2 & \text{as } \widehat{\xi} \to 0^+, \\ \dfrac{2^{5/2}}{3}\widehat{\xi}^{3/2} + A_2\widehat{\xi}^{(5-\sqrt{7})/4} & \text{as } \widehat{\xi} \to \infty, \end{cases} \tag{4.72}$$

where A_1 and A_2 are degrees of freedom. (The unusual exponent in the second term in the far-field expansion comes from seeking a power-law behaviour and solving the resulting quadratic equation for the power-law exponent.) Thus, the leading-order-inner problem is correctly specified.

At $\mathrm{O}(\mathcal{M}^{1-\beta})$ in the outer region we find that η_1 is determined by the thin-film equation

$$\eta_0\frac{\mathrm{d}}{\mathrm{d}\xi}\left(\frac{\mathrm{d}^2\eta_1}{\mathrm{d}\xi^2}+\frac{1}{\xi}\frac{\mathrm{d}\eta_1}{\mathrm{d}\xi}-\mathcal{B}\eta_1\right)+\frac{\mathrm{d}}{\mathrm{d}\xi}\left(\frac{\eta_1}{\sqrt{1-\xi^2}}\right)-\frac{\eta_1}{\eta_0}\frac{\mathrm{d}}{\mathrm{d}\xi}\left(\frac{\eta_0}{\sqrt{1-\xi^2}}\right)=0 \quad \text{for } 0<\xi<1, \tag{4.73}$$

subject to the conditions

$$\frac{\mathrm{d}\eta_1}{\mathrm{d}\xi}=0 \text{ at } \xi=0; \quad \eta_1\sim A_2(1-\xi)^{(5-\sqrt{7})/4} \quad \text{as } \xi\to 1^-, \tag{4.74a, b}$$

where matching with (4.72) requires $\beta=(1+\sqrt{7})/2$. We then output the function $\overline{V}_1(\mathcal{B})$, given by

$$\overline{V}_1(\mathcal{B})=2\pi\int_0^1 \xi\eta_1(\xi)\,\mathrm{d}\xi. \tag{4.75}$$

Overall, we have

$$\overline{V}(\mathcal{B},\mathcal{M})\sim\frac{\mathcal{M}}{\mathcal{M}_c(\mathcal{B})}+\mathcal{M}^{(1-\sqrt{7})/2}\overline{V}_1(\mathcal{B}) \quad \text{as } \mathcal{M}\to\infty \text{ with } \mathcal{B}=\mathrm{O}(1). \tag{4.76}$$

The first term in this asymptote is used to validate the numerical solution for $\overline{V}(\mathcal{B},\mathcal{M})$ in figure 4.9(a). To obtain accurate estimates of $\overline{V}_0(\mathcal{B})$ and $\overline{V}_1(\mathcal{B})$, we solve for $\overline{V}(\mathcal{B},\mathcal{M})$ for large $\mathcal{M}$ and use Richardson extrapolation; these solutions are plotted in figure 4.9(b). We see that $\overline{V}_1(\mathcal{B})>0$ at least for $0\leq\mathcal{B}\leq 100$.

4.B.3 $\mathcal{B},\mathcal{M}\to\infty$ with $\mathcal{M}/\mathcal{B}^{1/2}=\mathrm{O}(1)$

To reconcile the asymptotes (4.65) and (4.76), we now consider the distinguished limit in which $\mathcal{B},\mathcal{M}\to\infty$ with $\nu=\mathcal{M}/\mathcal{B}^{1/2}=\mathrm{O}(1)$. The asymptotic structure consists of an outer region where surface-tension gradients balance gravity, an inner region where surface-tension gradients balance capillarity and an intermediate region where all three effects are in balance.

We consider an integrated version of the thin-film equation (4.6), given by

$$\eta\frac{\mathrm{d}^2\eta}{\mathrm{d}\xi^2}-\frac{1}{2}\left(\frac{\mathrm{d}\eta}{\mathrm{d}\xi}\right)^2-\frac{\mathcal{B}\eta^2}{2}+\frac{\mathcal{M}\eta}{\sqrt{1-\xi^2}}=-\frac{1}{2}-\frac{\eta}{\xi}\frac{\mathrm{d}\eta}{\mathrm{d}\xi}-\int_\xi^1\frac{1}{\xi}\left(\frac{\mathrm{d}\eta}{\mathrm{d}\xi}\right)^2\mathrm{d}\xi. \tag{4.77}$$

In the outer region, we expand $\eta\sim\mathcal{B}^{-1/2}\eta_0$ as $\mathcal{B}\to\infty$ with $\nu=\mathrm{O}(1)$. To leading order, we obtain a quadratic equation for η_0, given by

$$\frac{\eta_0^2}{2}-\frac{\nu\eta_0}{\sqrt{1-\xi^2}}=\frac{1}{2} \quad \text{for } 0<\xi<1. \tag{4.78}$$

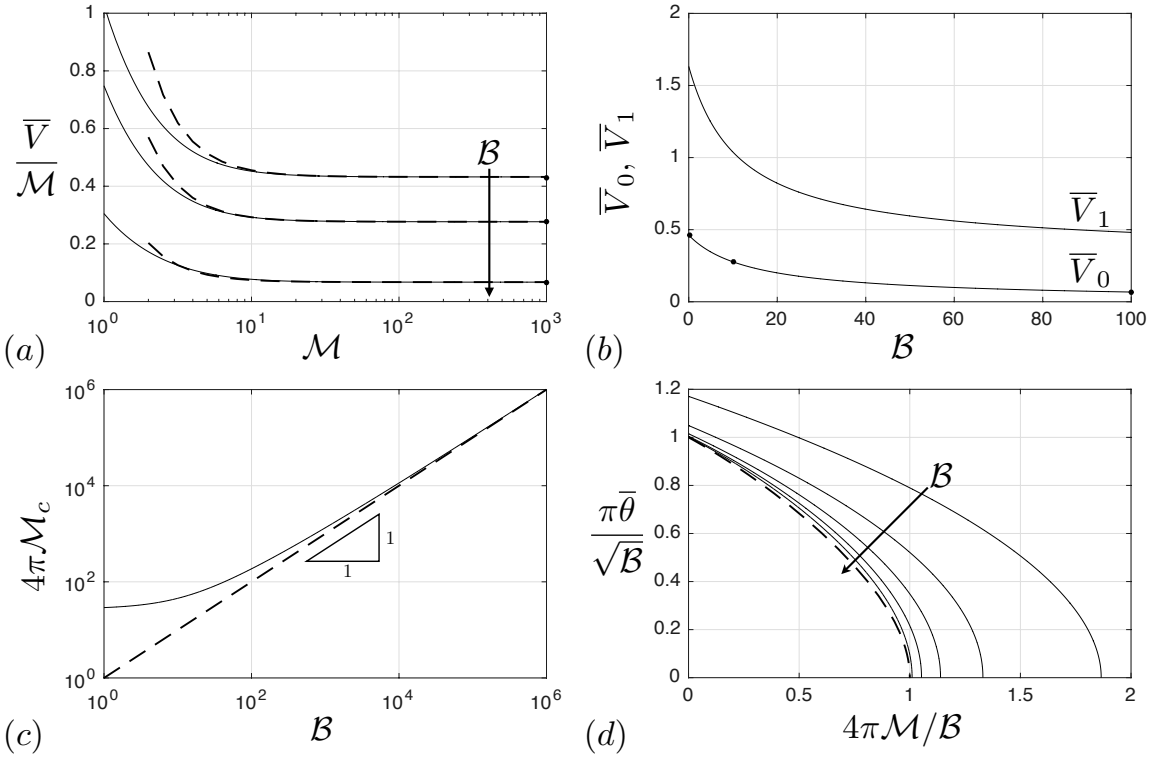

Figure 4.9: Validation of the numerical solution of the boundary-value problems on the timescales of contact-line motion and mass loss by comparison with leading-order asymptotic predictions. (*a*) $\overline{V}/\mathcal{M}$ as a function of $\mathcal{M}$ for $\mathcal{B} = 1, 10, 100$. The dashed curve is the asymptote (4.76), which we see agrees well with the numerical solution for large values of $\mathcal{M}$. (*b*) Plots of $\overline{V}_0$ and $\overline{V}_1$, for which $\overline{V} \sim \mathcal{M}\overline{V}_0 + \mathcal{M}^{(1-\sqrt{7})/2}\overline{V}_1$ as $\mathcal{B} \to \infty$, as functions of $\mathcal{B}$. (*c*) $4\pi\mathcal{M}_c$ as a function of $\mathcal{B}$. The dashed curve is the asymptote (4.86), which we see agrees well with the numerical solution for large values of $\mathcal{B}$. (*d*) $\pi\overline{\theta}/\sqrt{\mathcal{B}}$ as a function of $4\pi\mathcal{M}/\mathcal{B}$ for $\mathcal{B} = 10^2, 10^3, \ldots, 10^6$. The dashed curve is the asymptote (4.90), which we see agrees well with the numerical solution for large values of $\mathcal{B}$. The shape of the curves for small values of $\overline{\theta}$ implies the existence of a critical Marangoni number.

For η_0 to be positive for $0 < \xi < 1$, we find that we require the positive root of this quadratic, namely

$$\eta_0 = \frac{\nu + \sqrt{\nu^2 + 1 - \xi^2}}{\sqrt{1 - \xi^2}} \quad \text{for } 0 < \xi < 1. \tag{4.79}$$

In the inner region, we set $\widehat{\xi} = \mathcal{B}(1 - \xi)$ and expand $\eta \sim \nu \mathcal{B}^{-1} \widehat{\eta}_0(\widehat{\xi})$ as $\mathcal{B} \to \infty$ with $\nu = \mathrm{O}(1)$ and $\widehat{\xi} = \mathrm{O}(1)$. We find that $\widehat{\eta}_0$ satisfies the thin-film equation given by

$$\widehat{\eta}_0 \frac{\mathrm{d}^2 \widehat{\eta}_0}{\mathrm{d}\widehat{\xi}^{\,2}} - \frac{1}{2} \left(\frac{\mathrm{d}\widehat{\eta}_0}{\mathrm{d}\widehat{\xi}} \right)^2 + \frac{\widehat{\eta}_0}{(2\widehat{\xi})^2} = -\frac{1}{2\nu^2} \quad \text{for } \widehat{\xi} > 0. \tag{4.80}$$

This is to be solved subject to the conditions

$$\widehat{\eta}_0 = 0 \text{ at } \widehat{\xi} = 0^+; \quad \widehat{\eta}_0 \sim \frac{2^{5/2}}{3} \widehat{\xi}^{3/2} \text{ as } \widehat{\xi} \to \infty, \tag{4.81a, b}$$

the latter condition being required to match with the intermediate region. A degree-of-freedom count confirms that (4.80) and (4.81) is correctly specified.

In the intermediate region, we set $\widetilde{\xi} = \mathcal{B}^{1/2}(1 - \xi)$ and expand $\eta \sim \nu \mathcal{B}^{-1/4} \widetilde{\eta}_0(\widetilde{\xi})$ as $\mathcal{B} \to \infty$ with $\nu = \mathrm{O}(1)$ and $\widetilde{\xi} = \mathrm{O}(1)$. We find that $\widetilde{\eta}_0$ satisfies the thin-film equation given by

$$\widetilde{\eta}_0 \frac{\mathrm{d}^2 \widetilde{\eta}_0}{\mathrm{d}\widetilde{\xi}^{\,2}} - \frac{1}{2} \left(\frac{\mathrm{d}\widetilde{\eta}_0}{\mathrm{d}\widetilde{\xi}} \right)^2 - \frac{\widetilde{\eta}_0^2}{2} + \frac{\widetilde{\eta}_0}{(2\widetilde{\xi})^2} = 0 \quad \text{for } \widetilde{\xi} > 0. \tag{4.82}$$

This is to be solved subject to the matching conditions

$$\widetilde{\eta}_0 \sim \frac{2^{5/2}}{3} \widetilde{\xi}^{3/2} \text{ as } \widetilde{\xi} \to 0^+; \quad \widetilde{\eta}_0 \sim \left(\frac{2}{\widetilde{\xi}} \right)^{1/2} \text{ as } \widetilde{\xi} \to \infty. \tag{4.83a, b}$$

A degree-of-freedom count confirms that (4.82) and (4.83) is correctly specified.

We deduce that $\overline{V} \sim \mathcal{B}^{-1/2} \widetilde{V}_0(\nu)$ as $\mathcal{B} \to \infty$ with $\nu = \mathrm{O}(1)$, where $\widetilde{V}_0(\nu)$ is given by

$$\widetilde{V}_0(\nu) = 2\pi \int_0^1 \xi \eta_0 \, \mathrm{d}\xi = 2\pi\nu + \pi\sqrt{1 + \nu^2} + \pi\nu^2 \log \left(\frac{1 + \sqrt{1 + \nu^2}}{\nu} \right). \tag{4.84}$$

We observe that $\widetilde{V}_0(\nu)$ is a monotone-increasing function of ν, with

$$\widetilde{V}_0(\nu) \sim \begin{cases} \pi & \text{as } \nu \to 0^+, \\ 4\pi\nu & \text{as } \nu \to \infty. \end{cases} \tag{4.85}$$

We note that (4.85) is in agreement with the large-$\mathcal{B}$ asymptote (4.65). To show agreement with the large-$\mathcal{M}$ asymptote (4.76), we need to show that

$$\overline{V}_0(\mathcal{B}) = 1/\mathcal{M}_c(\mathcal{B}) \sim 4\pi/\mathcal{B} \quad \text{as } \mathcal{B} \to \infty. \tag{4.86}$$

We therefore return to the leading-order-outer problem in the limit $\mathcal{M} \to \infty$ with $\mathcal{B} = \mathrm{O}(1)$, namely the thin-film equation (4.6) with $\mathcal{M} = 1$ and the conditions (4.74). The function $\overline{V}_0(\mathcal{B})$ is given in terms of the solution of this problem by the expression (4.69). We will analyse this boundary-value problem in the limit $\mathcal{B} \to \infty$ to determine the large-$\mathcal{B}$ behaviour of $\overline{V}_0(\mathcal{B})$. The asymptotic structure consists of an outer region where gravity balances Marangoni forces and a "sub-outer" region where capillarity, gravity and Marangoni forces all balance, and the matching condition (4.74b) is satisfied.

In the outer region, where $1 - \xi = \mathrm{O}(1)$, we expand $\eta_0 \sim \eta_{00}$ as $\mathcal{B} \to \infty$. To leading order, after integrating once with respect to ξ, we find that η_{00} is given by

$$\eta_{00} = \frac{2}{\sqrt{1-\xi^2}}. \tag{4.87}$$

In the sub-outer region, we set $\widetilde{\xi} = \mathcal{B}^{1/2}(1-\xi) = \mathrm{O}(1)$ and expand $\eta_0 \sim \mathcal{B}^{-3/4}\widetilde{\eta}_0(\widetilde{\xi})$ as $\mathcal{B} \to \infty$ with $\widetilde{\xi} = \mathrm{O}(1)$. We find that $\widetilde{\eta}_0$ satisfies (4.82) and (4.83). We deduce that

$$\overline{V}_0(\mathcal{B}) \sim \frac{2\pi}{\mathcal{B}} \int_0^1 \frac{2\xi}{\sqrt{1-\xi^2}}\,\mathrm{d}\xi = \frac{4\pi}{\mathcal{B}} \quad \text{as } \mathcal{B} \to \infty, \tag{4.88}$$

so that (4.76) and (4.85) are in agreement. The asymptote (4.86) is used to validate the numerical solution in figure 4.9(c).

4.B.4 Implications for the timescale of contact-line motion

We recall that the functions $\overline{\theta}$ (from the boundary-value problem on the timescale of contact-line motion) and $\overline{V}$ (from the boundary-value problem on the timescale of mass loss) satisfy the implicit relationship (4.38). We may use this relationship along with the asymptotic results in this appendix to obtain asymptotes for the function $\overline{\theta}(\mathcal{B}, \mathcal{M})$ (note $\mathcal{B}$ and $\mathcal{M}$ are dummy variables); we use these asymptotes to validate our numerical results.

Using the asymptote (4.76), we deduce that

$$\overline{\theta}(\mathcal{B}, \mathcal{M}) \sim a(\mathcal{B})\,(\mathcal{M}_c(\mathcal{B}) - \mathcal{M})^{2/(1+\sqrt{7})} \quad \text{as } \mathcal{M} \to \mathcal{M}_c(\mathcal{B})^-, \tag{4.89}$$

where $a(\mathcal{B}) = \mathcal{M}_c(\mathcal{B})^{1-4/(1+\sqrt{7})}\overline{V}_1(\mathcal{B})^{-2/(1+\sqrt{7})}$. This tells us how the macroscopic contact angle approaches zero as the Marangoni number approaches its critical value. This asymptote is plotted for $\mathcal{B} = 0$ in figure 4.1(d) and shows good agreement with the numerical solution in the expected range of validity. We note that our numerical simulations suggest that $\overline{V}_0$ and $\overline{V}_1$ are positive so that $a(\mathcal{B})$ is positive (at least for

$0 \leq \mathcal{B} \leq 100$), meaning that $\overline{\theta}(\mathcal{B}, \mathcal{M})$ is a single-valued function of $\mathcal{M}$ in the vicinity of $\mathcal{M}_c$.

Using the asymptote (4.84), we deduce that

$$\overline{\theta}(\mathcal{B}, \mathcal{M}) \sim \frac{\mathcal{B}^{1/2}}{\widetilde{V}_0(\nu)} \quad \text{as } \mathcal{B} \to \infty \text{ with } \frac{\mathcal{M}}{\mathcal{B}} = \frac{\nu}{\widetilde{V}_0(\nu)} = \mathrm{O}(1), \tag{4.90}$$

with the function $\widetilde{V}_0(\nu)$ given by (4.84). This asymptote is used to validate the numerical solution in figure 4.9(d), although we note that the convergence of the numerical solution to the asymptote is slow. We note that for any $c \in [0, 1/4\pi)$, there is a unique solution $\nu \geq 0$ to the equation $\nu/\widetilde{V}_0(\nu) = c$, but there is no solution for $c > 1/4\pi$. This is due to the asymptotic solution breaking down as $\mathcal{M}/\mathcal{B} \to 1/4\pi^{-}$, which is consistent with the asymptote $\mathcal{M}_c(\mathcal{B}) \sim \mathcal{B}/4\pi$ as $\mathcal{B} \to \infty$.

Chapter 5

Kinetic effects regularize the mass-flux singularity

5.1 Motivation

The lens evaporation model that we used throughout chapters 2–4 has a singularity in the mass flux at the contact line. This leads to a singularity in the depth-averaged radial velocity at the contact line; such a divergent velocity is unphysical. In this chapter, we instead adopt a linear, kinetics-based constitutive law for the mass flux across the liquid–gas interface, inspired by the Hertz-Knudsen relation (1.4); we assume that the equilibrium vapour concentration is constant. We will have two main goals. The first is to investigate the way in which kinetic effects regularize the mass-flux singularity at the contact line. The second is to derive an explicit expression for the evaporation rate.

The content of this chapter is based heavily on Saxton *et al.* (2016a).

5.2 Formulation

The transport of vapour within the gas phase is governed by the steady version of (2.11), subject to the condition of no flux of vapour through the substrate (2.12b) and the far-field condition (2.13). However, the boundary condition on the free surface of the drop for the lens model (2.12a) is replaced by the boundary condition

$$-DM\frac{\partial c^*}{\partial z^*} = E^* \quad \text{on } z^* = 0,\ 0 \leq r^* < s^*, \tag{5.1}$$

which states that the mass flux across the liquid–gas interface is entirely accounted for the mass flux of liquid vapour. We assume that the mass flux out of the drop is

governed by a linear constitutive law, given by

$$E^* = Mv_k(c_e - c^*), \tag{5.2}$$

where the equilibrium vapour concentration c_e is a constant. The constitutive law (5.2) is inspired by the Hertz-Knudsen relation (Cercignani, 2000). As discussed in chapter 1, the Hertz-Knudsen relation is strictly only valid when the gas phase consists of pure vapour. However, there is experimental evidence that it may be valid for a vapour–inert gas mixture (Preston, 1933), and it has previously been used to model such situations (Sultan *et al.*, 2005). The constant v_k is a typical kinetic velocity, given by

$$v_k = \sigma_e \left(\frac{\overline{R} T_{\text{in}}}{2\pi M} \right)^{1/2}, \tag{5.3}$$

where $\overline{R}$ is the universal gas constant and T_{in} is the interfacial temperature. Values of v_k for hexane, isopropanol, and HFE-7100 are given in table 2.1. The (dimensionless) evaporation coefficient σ_e is the fraction of the maximum possible evaporating flow rate that actually occurs (Cercignani, 2000). One disadvantage of the constitutive law (5.2) is that the evaporation coefficient σ_e is difficult to estimate; although a value of unity has been reported for many standard liquids, smaller values (anywhere between about 10^{-4} and 1) have been reported in other cases.

We note that if the contact line is pinned (so that the contact-set radius s^* is constant) the mixed-boundary-value problem for the vapour concentration is independent of time — *i.e.* the problem is steady. If instead the contact line is allowed to move (so that s^* depends on time), then the problem is quasi-steady; the time dependence would become important if the expression that we ultimately derive for the mass flux were to be used as an input for a model for the evolution of the liquid drop. We shall therefore suppress the dependence of s^* on time in the case that the contact line is allowed to move, and use s^* as a typical lengthscale on which to non-dimensionalize. Thus, the expression that we shall ultimately derive for the evaporation rate will be valid for drops with either pinned or moving contact lines.

We non-dimensionalize by scaling $r^* = s^* \widehat{r}$, $z^* = s^* z$, $c^* = c_\infty + (c_e - c_\infty)c$, and $E^* = DM(c_e - c_\infty)E/s^*$ (thus $\widehat{r} = r/s$). We obtain thereby the following mixed-

	Hexane	Isopropanol	HFE-7100
$s^* = 5\text{mm}$	1.1×10^5	4.2×10^4	2.3×10^4
$s^* = 50\mu\text{m}$	1.1×10^3	420	230

Table 5.1: Values of the kinetic Péclet number $\text{Pe}_\text{k} = s^* v_k / D$ for drops of hexane, isopropanol, and HFE-7100 with contact-set radii of 5mm and 50μm.

boundary-value problem for the dimensionless vapour concentration $c(r, z)$:

$$\nabla^2 c = 0 \qquad \text{for } z > 0, \tag{5.4}$$

$$c \to 0 \qquad \text{as } \widehat{r}^2 + z^2 \to \infty,\ z > 0, \tag{5.5}$$

$$-\frac{\partial c}{\partial z} = \text{Pe}_\text{k}(1 - c) \quad \text{on } z = 0,\ 0 \leq \widehat{r} < 1, \tag{5.6}$$

$$\frac{\partial c}{\partial z} = 0 \qquad \text{on } z = 0,\ \widehat{r} > 1, \tag{5.7}$$

3 where non-dimensionalization has introduced a dimensionless parameter, namely the kinetic Péclet number,

$$\text{Pe}_\text{k} = \frac{s^* v_k}{D}. \tag{5.8}$$

The kinetic Péclet number is the ratio of the timescales of diffusive and kinetic effects (over the radius of the drop; s^{*2}/D and s^*/v_k, respectively) and is the only parameter remaining in the problem following non-dimensionalization. We note the physical significance of two extreme cases: $\text{Pe}_\text{k} = 0$ corresponds to the case of no mass transfer, while $\text{Pe}_\text{k} = \infty$ corresponds to the case in which the vapour immediately above the free surface is at thermodynamic equilibrium, so that $c = 1$ on $z = 0,\ 0 \leq \widehat{r} < 1$. Since this is the limit used in the lens model, we expect to obtain a diverging mass flux at the contact line as $\text{Pe}_\text{k} \to \infty$ (as will be discussed in §5.3.1). Values of Pe_k for drops of hexane, isopropanol, and hexane, with contact-set radii of 5mm and 50μm are given in table 5.1; we see that the kinetic Péclet number may take a wide range of values, but that it is at least moderately large for all but very small drops.

The key quantity of interest, the dimensionless evaporation rate $E(\widehat{r})$, is given by

$$E(\widehat{r}) = -\left.\frac{\partial c}{\partial z}\right|_{z=0} = \text{Pe}_\text{k}[1 - c(\widehat{r}, 0)] \quad \text{for } 0 \leq \widehat{r} < 1. \tag{5.9}$$

A related quantity of interest, and a useful proxy, is the evaporation rate at the contact line, $E(1^-)$; the liquid motion has a strong dependence upon the size of this quantity (Oliver *et al.*, 2015). We note that with $\text{Pe}_\text{k} = \infty$, $E(1^-)$ is not defined.

Non-dimensionalization implies that $Q^* = DM(c_e - c_\infty)s^*Q$, where the total (dimensionless) flux Q out of the drop per unit time is given by

$$Q = 2\pi \int_0^1 \widehat{r} E(\widehat{r}\,)\,\mathrm{d}\widehat{r}. \tag{5.10}$$

We emphasize that the three quantities $E(\widehat{r}\,)$, $E(1^-)$, and Q are all functions of the kinetic Péclet number $\mathrm{Pe_k}$.

5.3 Local analysis near the contact line

In this section, we perform a local analysis near the contact line of both the lens model and the kinetics-based model (considering the former puts the latter into context). This will demonstrate explicitly that the lens model has a mass-flux singularity at the contact line, while the kinetics-based model does not. Comparing the local expansions for the two models should also give us some insight into the way in which the kinetics-based model regularizes the mass-flux singularity.

5.3.1 Lens model

For the lens model, the boundary condition (5.6) is replaced by

$$c = 1 \quad \text{on } z = 0,\ 0 \le \widehat{r} < 1. \tag{5.11}$$

As noted earlier, this may be viewed as a special case of (5.6) with $\mathrm{Pe_k} = \infty$. Recall that the lens model (5.4), (5.5), (5.7), and (5.11) is mathematically equivalent to the problem of finding the electric potential around a disc charged to a uniform potential (Weber, 1873). Assuming continuity at $\widehat{r} = 1$, this electrostatic problem has an exact solution (see, for example Duffy, 2008; Wiley and Webster, 1982), given by

$$c(\widehat{r}, z) = \frac{2}{\pi} \sin^{-1}\left(\frac{2}{((\widehat{r}-1)^2 + z^2)^{1/2} + ((\widehat{r}+1)^2 + z^2)^{1/2}} \right). \tag{5.12}$$

We deduce from (5.12) that the evaporation rate is given by

$$E(\widehat{r}\,) = \frac{2}{\pi(1-\widehat{r}^{\,2})^{1/2}} \quad \text{for } 0 \le \widehat{r} < 1. \tag{5.13}$$

We note from (5.13) that the total flux, $Q = 4$, is finite.

From the exact solution (5.12), we deduce that the local expansion of the solution near the contact line is given by

$$c(\widehat{r}, z) \sim 1 - \frac{2^{3/2}}{\pi} \rho^{1/2} \cos\left(\frac{\theta}{2}\right), \tag{5.14}$$

as $\rho \to 0^+$, $0 \leq \theta < \pi$, where (ρ, θ) are local polar coordinates defined by $\widehat{r} = 1 + \rho\cos\theta$, $z = \rho\sin\theta$ (we note that these definitions of ρ and θ are different to those used throughout chapters 2–4). The corresponding evaporation rate near the contact line has the local expansion

$$E(\widehat{r}) \sim \frac{2^{1/2}}{\pi(1-\widehat{r})^{1/2}} \quad \text{as } \widehat{r} \to 1^-. \tag{5.15}$$

Thus, we see clearly that there is an inverse-square-root singularity in the evaporation rate at the contact line, $\widehat{r} = 1$. We note that (5.14) and (5.15) could alternatively have been derived directly via a local analysis of (5.4), (5.7), and (5.11) (assuming c to be continuous at the contact line).

5.3.2 Kinetics-based model

We now return to the mixed-boundary-value problem (5.4)–(5.7) for finite $\mathrm{Pe_k}$. We assume that c is continuous at the contact line and takes the value $c_L(\mathrm{Pe_k})$ there, with $c_L(\mathrm{Pe_k})$ not equal to 0 or 1. Under these assumptions, a local analysis near the contact line implies that

$$c(\widehat{r}, z) \sim c_L(\mathrm{Pe_k}) + \frac{\mathrm{Pe_k}[1 - c_L(\mathrm{Pe_k})]}{\pi}\rho[(\cos\theta)(\log\rho) - \theta\sin\theta], \tag{5.16}$$

as $\rho \to 0^+$ for $0 \leq \theta \leq \pi$, where $c_L(\mathrm{Pe_k})$ is a degree of freedom. We then use (5.9) to find that the local expansion for the evaporation rate $E(\widehat{r})$ near the contact line is given by

$$E(\widehat{r}) \sim \mathrm{Pe_k}[1 - c_L(\mathrm{Pe_k})]\left[1 + \frac{\mathrm{Pe_k}}{\pi}(1-\widehat{r})\log(1-\widehat{r})\right] \quad \text{as } \widehat{r} \to 1^-. \tag{5.17}$$

In particular, this implies that the evaporation rate at the contact line $E(1^-)$ is given by

$$E(1^-) = \mathrm{Pe_k}[1 - c_L(\mathrm{Pe_k})]. \tag{5.18}$$

We recall that the lens model is a special case of the kinetics-based model with $\mathrm{Pe_k} = \infty$. Thus, for the local expansions (5.14) and (5.16) to be in agreement, it must be the case that

$$c_L(\mathrm{Pe_k}) \to 1 \quad \text{as } \mathrm{Pe_k} \to \infty, \tag{5.19}$$

but with $c_L \neq 1$ for finite $\mathrm{Pe_k}$. Hence, we will be interested in determining the degree of freedom $c_L(\mathrm{Pe_k})$ by solving the mixed-boundary-value problem (5.4)–(5.7).

5.3.3 Thick drops

The analysis presented in this chapter pertains to thin drops, with a small microscopic contact angle Ψ. Our analysis is only valid to leading order in the thin-film limit. Since we linearized the boundary condition on the free surface of the drop onto the substrate, the corrections to our analysis are of size $\mathrm{O}(\Psi)$. While the leading-order prediction is independent of the drop profile, the $\mathrm{O}(\Psi)$-corrections account for the shape of the drop. Dependence on the drop profile is an ingredient in different mass-transfer models, such as those utilizing the Kelvin effect (Eggers and Pismen, 2010; Rednikov and Colinet, 2013).

The expression (1.4) for the mass flux suggests that the inclusion of kinetic effects also ensures a finite mass flux for thick drops (where the aspect ratio is of order unity). A local analysis of the lens model near the contact line for $0 < \Psi < \pi$ (see, for example, Cazabat and Guéna, 2010; Jackson, 1975), assuming c to be continuous at the contact line, implies that, as $\widehat{r} \to 1^-$,

$$E(\widehat{r}) \propto (1-\widehat{r})^{-a}, \quad a = \frac{\pi - 2\Psi}{2(\pi - \Psi)}. \tag{5.20}$$

Thus, there is a mass-flux singularity at the contact line for $0 < \Psi < \pi/2$. The expression (5.20) is consistent with the corresponding expression for a thin drop (5.15) in the limit $\Psi \to 0^+$. On the other hand, a local analysis of the kinetics-based model near the contact line for $0 < \Psi < \pi$ reveals that, as $\widehat{r} \to 1^-$,

$$\begin{aligned} E(\widehat{r}) \sim \mathrm{Pe_k}(1-c_L)\left[1 - \frac{\mathrm{Pe_k}}{\sin(\pi-\Psi)}(1-\widehat{r})\right] + \ldots \\ -\beta(1-\widehat{r})^{\pi/(\pi-\Psi)} \cos\left(\frac{\pi^2}{\pi-\Psi}\right), \end{aligned} \tag{5.21}$$

where $c_L(\Psi, \mathrm{Pe_k})$ and $\beta(\Psi, \mathrm{Pe_k})$ are degrees of freedom (the '...' indicating that other terms may impinge between those given). Thus the mass flux at the contact line is finite for $0 < \Psi < \pi$. The expression (5.21) is consistent with the corresponding expression for a thin drop (5.17) in the limit $\Psi \to 0^+$, provided that

$$\beta \sim \frac{{\mathrm{Pe_k}}^2(1-c_L)}{\Psi} \quad \text{as } \Psi \to 0^+. \tag{5.22}$$

The remainder of this thesis will be concerned with thin drops, but an interesting direction for future work would be to investigate more thoroughly how the mass-flux singularity for $0 < \Psi < \pi/2$, $\Psi = \mathrm{O}(1)$ is regularized by kinetic effects.

5.4 Explicit expression for the evaporation rate

We shall now solve the mixed-boundary-value problem (5.4)–(5.7). An important aim of this calculation is to determine the degree of freedom $c_L(\mathrm{Pe_k})$, appearing in (5.16), which will put the results of §5.3 in context. We will also obtain an explicit expression for the evaporation rate; this expression would be a key ingredient in investigations of the evolution of the drop.

5.4.1 Solution of the mixed-boundary-value problem

We note that the mixed-boundary-value problem (5.4)–(5.7) is mathematically equivalent to that of finding the temperature around a partially thermally insulated disc whose exterior is completely insulated; this problem was solved by Gladwell *et al.* (1983) using Hankel, Fourier cosine, and Abel transforms, as well as properties of Legendre polynomials. The solution is given by

$$c(\widehat{r}, z) = \int_0^\infty \int_0^1 f(x) \cos(kx) e^{-kz} J_0(k\widehat{r}) \, \mathrm{d}x \, \mathrm{d}k, \tag{5.23}$$

where $J_0(k\widehat{r})$ is the Bessel function of first kind of order zero, and the function $f(x)$ satisfies the Abel integral equation given by

$$-\frac{1}{\mathrm{Pe_k}} \frac{1}{\widehat{r}} \frac{\mathrm{d}}{\mathrm{d}\widehat{r}} \int_{\widehat{r}}^1 \frac{x f(x)}{(x^2 - \widehat{r}^2)^{1/2}} \, \mathrm{d}x + \int_0^{\widehat{r}} \frac{f(x)}{(\widehat{r}^2 - x^2)^{1/2}} \, \mathrm{d}x = 1 \quad \text{for } 0 < \widehat{r} < 1. \tag{5.24}$$

By writing $f(x) = \sum_{n=0}^\infty a_n \sin[(2n+1)\cos^{-1}(x)]$ and expanding (5.24) in Legendre polynomials (Gladwell *et al.*, 1983), we obtain

$$c(\widehat{r}, z) = \sum_{n=0}^\infty a_n(\mathrm{Pe_k}) \int_0^\infty \int_0^1 \sin[(2n+1)\cos^{-1} x] \cos(kx) e^{-kz} J_0(k\widehat{r}) \, \mathrm{d}x \, \mathrm{d}k, \tag{5.25}$$

where the coefficients $a_n(\mathrm{Pe_k})$ satisfy a system of infinitely many linear algebraic equations, given by

$$\frac{(2n+1)\pi}{2\mathrm{Pe_k}} a_n(\mathrm{Pe_k}) + \sum_{m=0}^\infty b_{mn} a_m(\mathrm{Pe_k}) = \delta_{0n} \quad \text{for } n = 0, 1, 2, \ldots, \tag{5.26}$$

where

$$b_{mn} = \frac{1}{2} \left(\frac{1}{2m+2n+1} + \frac{1}{2m-2n+1} - \frac{1}{2m+2n+3} - \frac{1}{2m-2n-1} \right), \tag{5.27}$$

and δ_{0n} is the Kronecker delta.

Using (5.9) we deduce that, for $0 \leq \widehat{r} < 1$, the evaporation rate is given by

$$E(\widehat{r}) = \sum_{n=0}^{\infty} a_n(\mathrm{Pe_k}) \int_0^{\infty} \int_0^1 \sin[(2n+1)\cos^{-1}(x)] k \cos(kx) J_0(k\widehat{r})\, \mathrm{d}x\, \mathrm{d}k. \tag{5.28}$$

We integrate by parts once with respect to x and then change the order of integration. The resulting integral with respect to k may be evaluated explicitly, yielding

$$E(\widehat{r}) = \sum_{n=0}^{\infty} (2n+1) a_n(\mathrm{Pe_k}) \int_{\widehat{r}}^1 \frac{\cos[(2n+1)\cos^{-1}(x)]}{(x^2-\widehat{r}^2)^{1/2}(1-x^2)^{1/2}}\, \mathrm{d}x, \tag{5.29}$$

for $0 \leq \widehat{r} < 1$. From this expression it is not clear, without further analysis, how E behaves as the contact line is approached, *i.e.* as $\widehat{r} \to 1^-$.

In appendix 5.A, we analyse (5.29) as $r \to 1^-$ to find that the evaporation rate at the contact line $E(1^-)$ is given by

$$E(1^-) = \frac{\pi}{2} \sum_{n=0}^{\infty} (2n+1) a_n(\mathrm{Pe_k}). \tag{5.30}$$

By comparing the expression (5.30) for the evaporation rate at the contact line to the earlier expression (5.18) for the same quantity in terms of the concentration $c_L(\mathrm{Pe_k})$ at the contact line, we deduce that

$$c_L(\mathrm{Pe_k}) = 1 - \frac{E(1^-)}{\mathrm{Pe_k}} = 1 - \frac{\pi}{2\mathrm{Pe_k}} \sum_{n=0}^{\infty} (2n+1) a_n(\mathrm{Pe_k}). \tag{5.31}$$

In practical applications, we may be interested in the total flux out of the drop, Q, given by

$$Q = 2\pi \sum_{n=0}^{\infty} (2n+1) a_n(\mathrm{Pe_k}) \int_0^1 \int_{\widehat{r}}^1 \frac{\widehat{r}\cos[(2n+1)\cos^{-1}(x)]}{(x^2-\widehat{r}^2)^{1/2}(1-x^2)^{1/2}}\, \mathrm{d}x\, \mathrm{d}\widehat{r}. \tag{5.32}$$

We switch the order of integration since the integral with respect to $\widehat{r}$ can be evaluated analytically. We then evaluate the remaining integral via the substitution $x = \cos(\theta)$ to obtain

$$Q = \frac{\pi^2 a_0(\mathrm{Pe_k})}{2}, \tag{5.33}$$

which is finite (as is also the case for infinite kinetic Péclet number).

5.4.2 Computing the evaporation rate

We have now deduced expressions for the evaporation rate $E(\widehat{r})$ for $0 \leq \widehat{r} < 1$, the concentration $c_L(\mathrm{Pe_k})$ at the contact line, the evaporation rate at the contact line

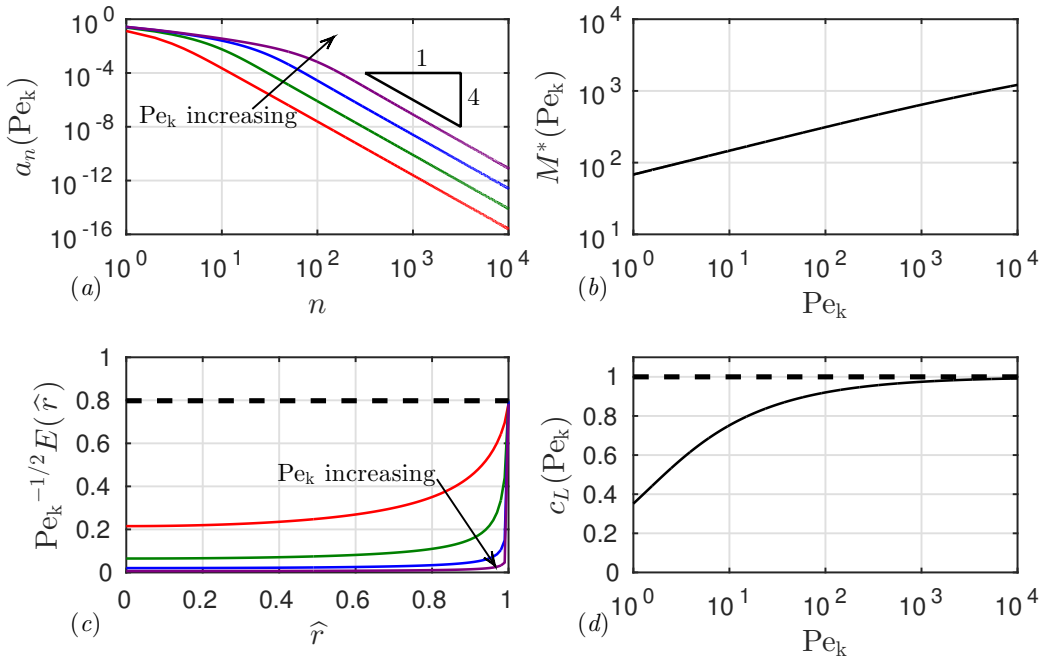

Figure 5.1: (a) The coefficients $a_n(\mathrm{Pe_k})$ that solve the algebraic system (5.26) truncated at $n = 10^4$, as a function of n for $\mathrm{Pe_k} = 10^1, 10^2, 10^3, 10^4$ (red, green, blue, and purple curves, respectively). (b) The value $n = M^*(\mathrm{Pe_k})$ at which the algebraic system (5.26) should be truncated so that the truncation error (5.34) is below 10^{-4}. (c) Scaled evaporation rate $\mathrm{Pe_k}^{-1/2}E(\widehat{r}\,)$ as a function of $\widehat{r}$ for $\mathrm{Pe_k} = 10^1, 10^2, 10^3, 10^4$ (red, green, blue, and purple curves, respectively). The black dashed line shows the apparent large-$\mathrm{Pe_k}$ asymptote (5.35) for the evaporation rate at the contact line (details in text). (d) The degree of freedom c_L that appears in the local expansion (5.17) of the evaporation rate at the contact line, as a function of $\mathrm{Pe_k}$. The black dashed line shows the large-$\mathrm{Pe_k}$ asymptote (5.19) that is predicted by our local analysis.

$E(1^-)$, and the total flux out of the drop Q. These expressions are in terms of a set of coefficients $a_n(\mathrm{Pe_k})$ that satisfy a system of infinitely many linear algebraic equations (5.26). We shall now describe how to solve numerically this algebraic system and thus how to compute the evaporation rate in practice.

Gladwell (1980) showed that the system is regular (in the sense that $a_{n+1} \ll a_n$ as $n \to \infty$) and may therefore be solved by truncation. In figure 5.1(a), we plot $a_n(\mathrm{Pe_k})$ as a function of n for several values of $\mathrm{Pe_k}$. We observe that $a_n = \mathrm{O}(n^{-4})$ as $n \to \infty$; this rapid decay confirms that truncating the system (at a suitably large value of n) is appropriate.

It remains to determine a suitable value of n at which to truncate the system (5.26). We define the truncation error $T_M(\mathrm{Pe_k})$ in the evaporation rate at the contact

line by

$$T_M(\mathrm{Pe_k}) = \frac{E_{2M}(\mathrm{Pe_k}) - E_M(\mathrm{Pe_k})}{E_{2M}(\mathrm{Pe_k})}, \quad E_M(\mathrm{Pe_k}) = \sum_{n=0}^{M} (2n+1) a_n(\mathrm{Pe_k}), \tag{5.34}$$

where the coefficients a_n satisfy the system (5.26) truncated at $n = M$. We define $M^*(\mathrm{Pe_k})$ to be the smallest value of M for which $T_M(\mathrm{Pe_k}) < 10^{-4}$. We calculate M^* for a range of values of $\mathrm{Pe_k}$ to create a lookup table, and then the value of M^* for general $\mathrm{Pe_k}$ is determined by spline interpolation (rounding up to the nearest integer). We plot M^* as a function of $\mathrm{Pe_k}$ in figure 5.1(b). Thus, to compute the coefficients $a_n(\mathrm{Pe_k})$ in practice, we first use a lookup table and spline interpolation to determine a suitable value $n = M^*(\mathrm{Pe_k})$ at which to truncate the system (5.26). The resulting finite linear algebraic system is then solved using MATLAB's backslash command (since the system is symmetric positive definite, this uses Cholesky factorization).

Once the coefficients $a_n(\mathrm{Pe_k})$ have been determined numerically, the evaporation rate $E(\widehat{r}\,)$ is approximated by (5.29) with the sum truncated at $n = M^*(\mathrm{Pe_k})$. The integral in (5.29) is evaluated numerically using the `integral` command in MATLAB. We check convergence in the usual way by reducing the error tolerances. We plot a scaled evaporation rate $\mathrm{Pe_k}^{-1/2} E(\widehat{r}\,)$ as a function of $\widehat{r}$ for several values of $\mathrm{Pe_k}$ in figure 5.1(c). We see that the evaporation rate is everywhere finite for the values of $\mathrm{Pe_k}$ plotted (which we note from table 5.1 covers a range of physically realistic values).

We note from figure 5.1(c) that for large values of $\mathrm{Pe_k}$ there appears to be a boundary layer near to the contact line in which the evaporation rate is much larger. We also observe from figure 5.1(c) that there appears to be a large-$\mathrm{Pe_k}$ asymptote for the evaporation rate at the contact line of the form

$$E(1^-) \sim \alpha \mathrm{Pe_k}^{1/2} \quad \text{as } \mathrm{Pe_k} \to \infty, \tag{5.35}$$

for some constant $\alpha \approx 0.798$ (with this asymptote, presented as the dashed line in figure 5.1(c), apparently being valid to within about 5% for $\mathrm{Pe_k} > 10$).

We plot the numerical solution for the degree of freedom c_L that appears in the local expansion (5.17) of the evaporation rate at the contact line as a function of $\mathrm{Pe_k}$ in figure 5.1(d). Our numerics predict that $c_L(\mathrm{Pe_k}) < 1$ for finite $\mathrm{Pe_k}$ and $c_L \to 1^-$ as $\mathrm{Pe_k} \to \infty$, which is in agreement with both our local analysis and the expression (5.31) (assuming that $a_n = \mathrm{O}(1)$ as $\mathrm{Pe_k} \to \infty$).

From table 5.1, we see that $\mathrm{Pe_k}$ is typically large in practice. This, together with the numerical result (5.35), motivates us to undertake an asymptotic analysis of the

limit $\mathrm{Pe_k} \to \infty$. It is not obvious how to find the coefficients $a_n(\mathrm{Pe_k})$ as $\mathrm{Pe_k} \to \infty$ in the algebraic system (5.26), nor is it obvious how to analyse (5.24) as $\mathrm{Pe_k} \to \infty$, so we instead proceed by analysing the mixed-boundary-value problem (5.4)–(5.7) rather than the exact solution (5.29).

5.5 Asymptotic analysis in the limit of large kinetic Péclet number

In this section we perform a matched-asymptotic analysis of the limit $\mathrm{Pe_k} \to \infty$ to gain further insight into the way in which kinetic effects regularize the mass-flux singularity at the contact line. This is a singular perturbation problem; the asymptotic structure consists of an outer region in which $|1 - \widehat{r}\,|,\ z = \mathrm{O}(1)$ as $\mathrm{Pe_k} \to \infty$ and an inner region near the contact line in which there is a full balance of terms in the boundary condition (5.6) on the free surface of the drop. We see that this happens when $z = \mathrm{O}(\mathrm{Pe_k}^{-1})$ and that to keep a full balance of terms in Laplace's equation (5.4) we require $|1 - \widehat{r}\,| = \mathrm{O}(\mathrm{Pe_k}^{-1})$ as $\mathrm{Pe_k} \to \infty$.

5.5.1 Outer region

We expand $c \sim c_0$ as $\mathrm{Pe_k} \to \infty$. We find that the leading-order vapour concentration $c_0(\widehat{r}, z)$ satisfies Laplace's equation (5.4), the far-field condition (5.5), and the no-flux boundary condition (5.7) on the solid substrate, but the boundary condition (5.6) on the free surface of the drop is replaced by

$$c_0 = 1 \quad \text{on } z = 0,\ 0 \leq \widehat{r} < 1. \tag{5.36}$$

The leading-order vapour concentration therefore satisfies the mixed-boundary-value problem considered in §5.3.1 and we deduce that as $\mathrm{Pe_k} \to \infty$ with $(1 - \widehat{r}\,) = \mathrm{O}(1)$,

$$E(\widehat{r}\,) \sim -\left.\frac{\partial c_0}{\partial z}\right|_{z=0} = \frac{2}{\pi(1 - \widehat{r}^{\,2})^{1/2}} \quad \text{for } 0 \leq \widehat{r} < 1. \tag{5.37}$$

We see that this outer evaporation rate has an inverse-square-root singularity as $\widehat{r} \to 1^-$; we expect this singularity to be regularized in an inner region close to $\widehat{r} = 1$.

5.5.2 Inner region

5.5.2.1 The leading-order-inner problem

In an inner region near the contact line we set $\widehat{r} = 1 + \mathrm{Pe_k}^{-1}X$, $z = \mathrm{Pe_k}^{-1}Y$, and expand $c(\widehat{r}, z) \sim 1 - \mathrm{Pe_k}^{-1/2}C(X, Y)$ as $\mathrm{Pe_k} \to \infty$. To leading order, the vapour

transport equation (5.4) and the mixed boundary conditions (5.6) and (5.7) become

$$\frac{\partial^2 C}{\partial X^2} + \frac{\partial^2 C}{\partial Y^2} = 0 \quad \text{for } Y > 0, \tag{5.38}$$

$$\frac{\partial C}{\partial Y} = C \quad \text{on } Y = 0,\ X < 0, \tag{5.39}$$

$$\frac{\partial C}{\partial Y} = 0 \quad \text{on } Y = 0,\ X > 0. \tag{5.40}$$

Finally, matching with the leading-order-outer solution (5.12) gives the conditions

$$C \sim \begin{cases} \dfrac{2^{3/2}}{\pi}\rho^{1/2}\cos\dfrac{\theta}{2} & \text{for } 0 \le \theta < \pi, \\ \dfrac{2^{1/2}}{\pi}\rho^{-1/2} & \text{for } \theta = \pi, \end{cases} \tag{5.41}$$

as $\rho \to \infty$, where (ρ, θ) are now plane polar coordinates related to (X, Y) by $X = \rho\cos\theta$, $Y = \rho\sin\theta$.

A local analysis of (5.38) subject to (5.39) and (5.40), assuming C to be continuous and non-zero at the contact line, implies that

$$C(X, Y) \sim C_O\left\{1 - \frac{\rho[(\log\rho)(\cos\theta) - \theta\sin\theta]}{\pi}\right\} \quad \text{as } \rho \to 0^+,\ 0 \le \theta \le \pi. \tag{5.42}$$

The value of the leading-order-inner solution at the contact line, $C_O := C(0, 0)$, is a degree of freedom in this expansion and we note that it is related to the degree of freedom $c_L(\mathrm{Pe_k})$ in the local expansion (5.17) of the full problem by

$$c_L(\mathrm{Pe_k}) \sim 1 - C_O{\mathrm{Pe_k}}^{-1/2} \quad \text{as } \mathrm{Pe_k} \to \infty. \tag{5.43}$$

The expression (5.18) for the evaporation rate at the contact line in terms of $c_L(\mathrm{Pe_k})$ then tells us that

$$E(1^-) \sim C_O{\mathrm{Pe_k}}^{1/2} \quad \text{as } \mathrm{Pe_k} \to \infty. \tag{5.44}$$

We shall solve the mixed-boundary-value problem (5.38)–(5.41) using the Wiener-Hopf method. The methodology employed is analogous to that used by Thompson (2012) to solve a similar problem (known as the 'dock problem') consisting of (5.38) and (5.40), but with a sign change to the right-hand side of (5.39) and with different far-field behaviour.

5.5.2.2 Regularized inner problem

We begin by defining the functions

$$C_+(X) = \begin{cases} 0 & \text{for } X < 0, \\ C(X, 0) & \text{for } X \ge 0, \end{cases} \quad C_-(X) = \begin{cases} C(X, 0) & \text{for } X < 0, \\ 0 & \text{for } X \ge 0, \end{cases} \tag{5.45}$$

with corresponding one-sided Fourier transforms $\overline{C}_{\pm}(k)$ given by

$$\overline{C}_{+}(k) = \int_0^{\infty} C_{+}(X) e^{ikX} \, \mathrm{d}X, \quad \overline{C}_{-}(k) = \int_{-\infty}^{0} C_{-}(X) e^{ikX} \, \mathrm{d}X. \tag{5.46}$$

We shall assume that $C(X, 0)$ is infinitely differentiable on $(-\infty, 0)$ and $(0, \infty)$. Then, using the far-field behaviour (5.41) and the local expansion (5.42), the Abelian Theorem in appendix 5.B.1 tells us that $\overline{C}_{+}(k)$ is holomorphic in $\Im(k) > 0$, where $\Im$ denotes the imaginary part, with

$$\overline{C}_{+}(k) \sim \frac{iC_O}{k} \quad \text{as } k \to \infty, \ \Im(k) > 0, \tag{5.47}$$

and $\overline{C}_{-}(k)$ is holomorphic in $\Im(k) < 0$, with

$$\overline{C}_{-}(k) \sim -\frac{iC_O}{k} \quad \text{as } k \to \infty, \ \Im(k) < 0. \tag{5.48}$$

Moreover, a standard asymptotic analysis implies that the behaviour of $\overline{C}_{\pm}(k)$ as $k \to 0$ is dominated by the behaviour of $C(X, 0)$ as $X \to \pm\infty$, with

$$\overline{C}_{+}(k) \sim \int_0^{\infty} \frac{2^{3/2}}{\pi} X^{1/2} e^{ikX} \, \mathrm{d}X = \frac{2^{1/2} e^{3\pi i/4}}{\pi^{1/2} k_{+}^{3/2}} \ \text{as } k \to 0, \ \Im(k) > 0, \tag{5.49}$$

$$\overline{C}_{-}(k) \sim \int_{-\infty}^{0} \frac{2^{1/2}}{\pi} (-X)^{-1/2} e^{ikX} \, \mathrm{d}X = \frac{2^{1/2} e^{-i\pi/4}}{\pi^{1/2} k_{-}^{1/2}} \ \text{as } k \to 0, \ \Im(k) < 0, \tag{5.50}$$

where $k_{+}^{3/2}$ and $k_{-}^{1/2}$ are defined as follows:

$$k_{+}^{3/2} = |k|^{3/2} e^{3i \arg(k)/2}, \ \text{for } -\frac{\pi}{2} \leq \arg(k) < \frac{3\pi}{2}, \tag{5.51}$$

$$k_{-}^{1/2} = |k|^{1/2} e^{i \arg(k)/2}, \ \text{for } -\frac{3\pi}{2} \leq \arg(k) < \frac{\pi}{2}. \tag{5.52}$$

Here, $k_{+}^{3/2}$ has a branch cut along the negative imaginary axis, while $k_{-}^{1/2}$ has a branch cut along the positive imaginary axis. The choice of branch is such that both $k_{+}^{3/2}$ and $k_{-}^{1/2}$ are real and positive when k is real and positive, so that $\overline{C}_{+}(k)$ is real and positive on the positive imaginary axis and $\overline{C}_{-}(k)$ is real and positive on the negative imaginary axis.

The Abelian Theorem in appendix 5.B.1 tells us that there is no value of k for which both $\overline{C}_{+}(k)$ and $\overline{C}_{-}(k)$ exist, so we are unable to apply the Wiener-Hopf method to the problem as it stands. Instead, we consider in the usual way (Carrier *et al.*, 2005; Noble, 1958) the regularized problem for the function $C^{\varepsilon}(X, Y)$, given by

$$\frac{\partial^2 C^{\varepsilon}}{\partial X^2} + \frac{\partial^2 C^{\varepsilon}}{\partial Y^2} = \varepsilon^2 C^{\varepsilon} \quad \text{for } Y > 0, \tag{5.53}$$

$$\frac{\partial C^{\varepsilon}}{\partial Y} = C^{\varepsilon} \qquad \text{on } Y = 0, \ X < 0, \tag{5.54}$$

$$\frac{\partial C^{\varepsilon}}{\partial Y} = 0 \qquad \text{on } Y = 0, \ X > 0. \tag{5.55}$$

We shall subsequently take the limit $\varepsilon \to 0^+$ to recover the leading-order-inner solution $C(X,Y) = \lim_{\varepsilon\to 0^+} C^\varepsilon(X,Y)$.

A local analysis of (5.53) subject to (5.54) and (5.55), assuming C^ε to be continuous and non-zero at the contact line, implies that $C^\varepsilon(X,Y)$ has the same local expansion (5.42) at the origin as $C(X,Y)$, but with C_O replaced by $C_O^\varepsilon := C^\varepsilon(0,0)$. A far-field analysis, admitting only exponentially decaying separable solutions, implies that we require

$$\frac{\partial C^\varepsilon}{\partial X} \sim \begin{cases} \dfrac{A^\varepsilon e^{-\varepsilon\rho}}{\rho^{1/2}} \cos\dfrac{\theta}{2} & \text{for } 0 \le \theta < \pi, \\ \dfrac{A^\varepsilon e^{-\varepsilon\rho}}{2\rho^{3/2}} & \text{for } \theta = \pi, \end{cases} \tag{5.56}$$

as $\rho \to \infty$, where in order to recover (5.41) in the limit $\varepsilon \to 0^+$, it is necessary for the constant A^ε to satisfy the condition

$$\lim_{\varepsilon\to 0^+} A^\varepsilon = \frac{2^{1/2}}{\pi}. \tag{5.57}$$

We now define $F^\varepsilon(X) = \partial C^\varepsilon/\partial X(X,0)$. Using (5.56), we deduce from the Abelian Theorem in appendix 5.B.1 that $\overline{F}^\varepsilon_+(k)$ is holomorphic in $\Im(k) > -\varepsilon$, while $\overline{F}^\varepsilon_-(k)$ is holomorphic in $\Im(k) < \varepsilon$. Moreover, we have

$$\overline{F}^\varepsilon_+(k) = -ik\overline{C}^\varepsilon_+(k) - C_O^\varepsilon \quad \text{for } \Im(k) > 0, \tag{5.58}$$

$$\overline{F}^\varepsilon_-(k) = -ik\overline{C}^\varepsilon_-(k) + C_O^\varepsilon \quad \text{for } \Im(k) < 0, \tag{5.59}$$

where the functions $C^\varepsilon_\pm(X)$ and their Fourier transforms $\overline{C}^\varepsilon_\pm(k)$ are defined analogously to (5.45) and (5.46). By applying analytic continuation, we deduce that $\overline{C}^\varepsilon_+(k)$ is holomorphic in $\Im(k) > -\varepsilon$ except for a simple pole at $k = 0$ and $\overline{C}^\varepsilon_-(k)$ is holomorphic in $\Im(k) < \varepsilon$ except for a simple pole at $k = 0$. The presence of a simple pole at the origin in both $\overline{C}^\varepsilon_+(k)$ and $\overline{C}^\varepsilon_-(k)$ is consistent with the constants $a_\pm$ in the far-field expansion

$$C^\varepsilon(X,0) \sim \begin{cases} a_- - \dfrac{A^\varepsilon e^{\varepsilon X}}{2\varepsilon(-X)^{3/2}} & \text{as } X \to -\infty, \\ a_+ - \dfrac{A^\varepsilon e^{-\varepsilon X}}{\varepsilon X^{1/2}} & \text{as } X \to +\infty, \end{cases} \tag{5.60}$$

(which follows from (5.56)) being non-zero. We shall therefore apply the Wiener-Hopf method to the functions $\overline{F}^\varepsilon_\pm(k)$. Since $\overline{F}^\varepsilon_+(k)$ is holomorphic in $\Im(k) > -\varepsilon$ and $\overline{F}^\varepsilon_-(k)$ is holomorphic in $\Im(k) < \varepsilon$, (5.58) and (5.59) imply that the functions $k\overline{C}_\pm(k)$ are both holomorphic in the overlap strip $-\varepsilon < \Im(k) < \varepsilon$. It is therefore equivalent to apply the Wiener-Hopf method to the functions $k\overline{C}_\pm(k)$. Before proceeding with

the Wiener-Hopf method in the next section, we note that the Abelian Theorem in appendix 5.B.1, together with the identities (5.58) and (5.59) (extended to $\Im(k) > -\varepsilon$ and $\Im(k) < \varepsilon$, respectively), gives the far-field behaviour

$$k\overline{C}^{\varepsilon}_{+}(k) \sim iC^{\varepsilon}_{O}, \qquad \overline{F}^{\varepsilon}_{+}(k) \to 0, \quad \text{as } k \to \infty,\ \Im(k) > -\varepsilon, \tag{5.61}$$

$$k\overline{C}^{\varepsilon}_{-}(k) \sim -iC^{\varepsilon}_{O}, \quad \overline{F}^{\varepsilon}_{-}(k) \to 0, \quad \text{as } k \to \infty,\ \Im(k) < \varepsilon. \tag{5.62}$$

5.5.2.3 Wiener-Hopf method

We begin by defining branches of the square roots $(k \pm i\varepsilon)^{1/2}$:

$$(k+i\varepsilon)^{1/2} = |k+i\varepsilon|^{1/2} e^{i\arg(k+i\varepsilon)/2},\ \text{for } -\frac{\pi}{2} \le \arg(k+i\varepsilon) < \frac{3\pi}{2}, \tag{5.63}$$

$$(k-i\varepsilon)^{1/2} = |k-i\varepsilon|^{1/2} e^{i\arg(k-i\varepsilon)/2},\ \text{for } -\frac{3\pi}{2} \le \arg(k-i\varepsilon) < \frac{\pi}{2}. \tag{5.64}$$

Thus, the square root $(k+i\varepsilon)^{1/2}$ has branch cut $S_- = \{k \in \mathbb{C} : \Re(k) = 0,\ \Im(k) \le -\varepsilon\}$, where $\Re$ denotes the real part, while $(k-i\varepsilon)^{1/2}$ has branch cut $S_+ = \{k \in \mathbb{C} : \Re(k) = 0,\ \Im(k) \ge \varepsilon\}$. We then define

$$(k^2+\varepsilon^2)^{1/2} = (k+i\varepsilon)^{1/2}(k-i\varepsilon)^{1/2}, \tag{5.65}$$

which has positive real part everywhere on the cut plane $\mathbb{C} \setminus (S_+ \cup S_-)$.

Now we define the Fourier transform in X of $C^{\varepsilon}(X,Y)$ by

$$\overline{C}^{\varepsilon}(k,Y) = \int_{-\infty}^{\infty} C^{\varepsilon}(X,Y) e^{ikX}\,\mathrm{d}X. \tag{5.66}$$

Taking a Fourier transform in X of (5.53), we find that

$$\overline{C}^{\varepsilon}(k,Y) = B(k) e^{-(k^2+\varepsilon^2)^{1/2}Y}, \quad B(k) = \overline{C}^{\varepsilon}_{+}(k) + \overline{C}^{\varepsilon}_{-}(k). \tag{5.67}$$

We therefore expect $\overline{C}^{\varepsilon}(k,Y)$ to be holomorphic in the strip $-\varepsilon < \Im(k) < \varepsilon$ except for a simple pole at the origin. The boundary conditions (5.54) and (5.55) imply that

$$-(k^2+\varepsilon^2)^{1/2} B(k) = \overline{C}^{\varepsilon}_{-}(k), \tag{5.68}$$

so that eliminating $B(k)$ between (5.67) and (5.68), and using (5.58) and (5.59) gives the following Wiener-Hopf equation for the functions $\overline{F}^{\varepsilon}_{\pm}(k)$:

$$[1 + (k^2+\varepsilon^2)^{-1/2}][\,\overline{F}^{\varepsilon}_{-}(k) - C^{\varepsilon}_{O}] + [\,\overline{F}^{\varepsilon}_{+}(k) + C^{\varepsilon}_{O}] = 0 \quad \text{for } -\varepsilon < \Im(k) < \varepsilon. \tag{5.69}$$

In order to apply the Wiener-Hopf method to (5.69), we must find a product factorization of the function $1 + (k^2+\varepsilon^2)^{-1/2}$, namely

$$1 + (k^2+\varepsilon^2)^{-1/2} = \frac{P^{\varepsilon}_{+}(k)}{P^{\varepsilon}_{-}(k)}, \tag{5.70}$$

where $P_+^\varepsilon(k)$ is holomorphic in some upper half-plane $\Im(k) > \gamma_+$ and $P_-^\varepsilon(k)$ is holomorphic in some lower half-plane $\Im(k) < \gamma_-$, with $-\varepsilon \leq \gamma_+ < \gamma_- \leq \varepsilon$. The details of this standard factorization are given in appendix 5.B.2 and reveal that suitable $P_\pm^\varepsilon(k)$ may be found with $P_+^\varepsilon(k)$ holomorphic in $\mathbb{C} \setminus S_-$ and $P_-^\varepsilon(k)$ holomorphic in $\mathbb{C} \setminus S_+$. Given the product factorization (5.70), we may rewrite the Wiener-Hopf equation (5.69) as

$$-\frac{\overline{F}_-^\varepsilon(k) - C_O^\varepsilon}{P_-^\varepsilon(k)} = \frac{\overline{F}_+^\varepsilon(k) + C_O^\varepsilon}{P_+^\varepsilon(k)} \quad \text{for } -\varepsilon < \Im(k) < \varepsilon. \tag{5.71}$$

Since both sides of (5.71) are equal in the overlap strip $-\varepsilon < \Im(k) < \varepsilon$, we deduce from the identity theorem that the right-hand side is the analytic continuation of the left-hand side into the upper half-plane. In the usual way, this allows us to define an entire $G(k)$, given by

$$G(k) = \begin{cases} -\dfrac{\overline{F}_-^\varepsilon(k) - C_O^\varepsilon}{P_-^\varepsilon(k)} & \text{for } \Im(k) < \varepsilon, \\ \dfrac{\overline{F}_+^\varepsilon(k) + C_O^\varepsilon}{P_+^\varepsilon(k)} & \text{for } \Im(k) > -\varepsilon. \end{cases} \tag{5.72}$$

Using the large-k behaviour (5.61) and (5.62) of $\overline{F}_\pm^\varepsilon(k)$ and the fact that, by construction, $P_\pm^\varepsilon(k) \to 1$ as $k \to \infty$ (see appendix 5.B.2), we deduce that the large-k behaviour of $G(k)$ is given by $G(k) \sim C_O^\varepsilon$ as $k \to \infty$. Then applying Liouville's theorem — that a bounded, entire function is constant — to $G(k)$ tells us that $G(k) \equiv C_O^\varepsilon$ and we deduce that

$$\overline{F}_+^\varepsilon(k) = C_O^\varepsilon[P_+^\varepsilon(k) - 1], \quad \overline{F}_-^\varepsilon(k) = C_O^\varepsilon[1 - P_-^\varepsilon(k)]. \tag{5.73}$$

Solving for $\overline{C}_\pm^\varepsilon(k)$ using (5.58) and (5.59), and taking the limit $\varepsilon \to 0^+$, we obtain

$$\overline{C}_+(k) = \frac{iC_O P_+(k)}{k} \text{ for } \Im(k) > 0, \quad \overline{C}_-(k) = -\frac{iC_O P_-(k)}{k} \text{ for } \Im(k) < 0, \tag{5.74}$$

where $P_\pm(k) := \lim_{\varepsilon \to 0^+} P_\pm^\varepsilon(k)$ and $C_O = \lim_{\varepsilon \to 0^+} C_O^\varepsilon$.

We use the behaviour (5.109) and (5.110) of $P_\pm(k)$ near the origin that we derive in appendix 5.B.2 to deduce the behaviour of $\overline{C}_\pm(k)$ near the origin is given by

$$\overline{C}_+(k) \sim \frac{e^{3\pi i/4} C_O}{k_+^{3/2}} \quad \text{as } k \to 0,\ \Im(k) > 0, \tag{5.75}$$

$$\overline{C}_-(k) \sim \frac{e^{-i\pi/4} C_O}{k_-^{1/2}} \quad \text{as } k \to 0,\ \Im(k) < 0, \tag{5.76}$$

with $k_+^{3/2}$ and $k_-^{1/2}$ as defined in (5.51) and (5.52). We compare (5.75) and (5.76) to the asymptotic results (5.49) and (5.50) to deduce that the degree of freedom C_O is given by

$$C_O = \left(\frac{2}{\pi}\right)^{1/2}. \tag{5.77}$$

We note that (5.77) may also be derived by, for example, inverting $\overline{F}_+^\varepsilon(k)$ to find $F_+^\varepsilon(X)$ for $X > 0$ (cf. §5.5.2.4) and then using Laplace's method to deduce that

$$F_+^\varepsilon(X) \sim \frac{\pi^{1/2} C_O^\varepsilon P_-^\varepsilon(-i\varepsilon) e^{-\varepsilon X}}{(2\varepsilon X)^{1/2}} \quad \text{as } X \to \infty. \tag{5.78}$$

We may then apply (5.56) and (5.57), together with the fact that $P_-^\varepsilon(-i\varepsilon) \sim (2\varepsilon)^{1/2}$ as $\varepsilon \to 0^+$, to deduce that

$$C_O^\varepsilon = \frac{A^\varepsilon (2\varepsilon)^{1/2}}{\pi^{1/2} P_-^\varepsilon(-i\varepsilon)} \sim \left(\frac{2}{\pi}\right)^{1/2} \quad \text{as } \varepsilon \to 0^+. \tag{5.79}$$

5.5.2.4 Inversion to find the inner evaporation rate

To find the evaporation rate in the inner region, we see from (5.54) that it is sufficient to find $C(X, 0)$ for $X < 0$. (The full solution $C(X, Y)$ of the leading-order-inner problem is given for completeness in appendix 5.B.3.) Since $C(X, 0) = C_-(X)$ for $X < 0$, we will invert $\overline{C}_-^\varepsilon(k)$ to find $C_-^\varepsilon(X)$ and take the limit $\varepsilon \to 0^+$. We have

$$C_-^\varepsilon(X) = -\frac{iC_O^\varepsilon}{2\pi} \int_\Gamma \frac{P_-^\varepsilon(k) e^{-ikX}}{k} \, \mathrm{d}k. \tag{5.80}$$

The inversion contour Γ lies below the singularities of $\overline{C}_-^\varepsilon(k)$ (namely, the branch cut S_+ and the pole at $k = 0$), so that for $X > 0$ we may close Γ in the lower half-plane, where $\Re(-ikX) < 0$, and use Cauchy's Theorem to obtain

$$C_-^\varepsilon(X) = 0 \quad \text{for } X > 0. \tag{5.81}$$

For $X < 0$, we deform Γ into the upper half-plane, where $\Re(-ikX) < 0$, with a 'keyhole' incision around S_+, writing $P_-^\varepsilon(k) = P_+^\varepsilon(k)/[1 + (k^2 + \varepsilon^2)^{-1/2}]$ since P_+ is continuous across S_+. We note that this encloses the pole at $k = 0$. We obtain thereby, for $X < 0$,

$$C_-^\varepsilon(X) = \frac{C_O^\varepsilon P_+^\varepsilon(0)}{1 + 1/\varepsilon} + \frac{C_O^\varepsilon}{\pi} \int_\varepsilon^\infty \frac{P_+^\varepsilon(it)(t^2 - \varepsilon^2)^{1/2} e^{tX}}{t(t^2 - \varepsilon^2 + 1)} \, \mathrm{d}t. \tag{5.82}$$

We take the limit $\varepsilon \to 0^+$ and use the expression (5.108) for $P_+(it)$ derived in appendix 5.B.2, as well as the fact that $P_+^\varepsilon(0) \sim \varepsilon^{1/2}$ as $\varepsilon \to 0^+$, to deduce that

$$C(X,0) = \frac{2^{1/2}}{\pi^{3/2}} \int_0^\infty \frac{I(t) e^{tX}}{t^{1/2}(1+t^2)} \, \mathrm{d}t \quad \text{for } X < 0, \tag{5.83}$$

where the function $I(t)$ is given by

$$I(t) = (1+t^2)^{1/4} \exp\left[-\frac{1}{\pi} \int_0^t \frac{\log(s)\, \mathrm{d}s}{1+s^2} \right] \quad \text{for } t > 0. \tag{5.84}$$

Thus, as $\mathrm{Pe_k} \to \infty$ with $X = \mathrm{Pe_k}(\widehat{r} - 1) = \mathrm{O}(1)$, $X < 0$, the evaporation rate in the inner region is given by

$$E(1 + {\mathrm{Pe_k}}^{-1} X) \sim {\mathrm{Pe_k}}^{1/2} C(X,0). \tag{5.85}$$

5.5.3 Conclusions from the matched-asymptotic analysis

The evaporation rate (5.37) is of order-unity size in the outer region of order-unity width away from the contact line, while the evaporation rate (5.85) is of size $\mathrm{O}({\mathrm{Pe_k}}^{1/2})$ in the inner region of width $\mathrm{O}({\mathrm{Pe_k}}^{-1})$ at the contact line. We therefore expect from (5.10) that the dominant contribution to the total flux out of the drop Q comes from the outer region, with

$$Q = 4 \int_0^1 \frac{\widehat{r}\, \mathrm{d}\widehat{r}}{(1-\widehat{r}^2)^{1/2}} + \mathrm{O}({\mathrm{Pe_k}}^{-1/2}) = 4 + \mathrm{O}({\mathrm{Pe_k}}^{-1/2}) \quad \text{as } \mathrm{Pe_k} \to \infty. \tag{5.86}$$

(We shall present numerical evidence in §5.5.4 that the error term in (5.86) is in fact of size $\mathrm{O}(\log(\mathrm{Pe_k})/\mathrm{Pe_k})$ as $\mathrm{Pe_k} \to \infty$.)

We recall that the degree of freedom $c_L(\mathrm{Pe_k})$ belonging to the finite-$\mathrm{Pe_k}$ mixed-boundary-value problem (5.4)–(5.7) is related to the degree of freedom C_O of the leading-order-inner problem (5.38)–(5.41) by the expression (5.43). Using the expression (5.77) for C_O, obtained from our matched-asymptotic analysis, we find that

$$c_L(\mathrm{Pe_k}) \sim 1 - \left(\frac{2}{\pi \mathrm{Pe_k}} \right)^{1/2} \quad \text{as } \mathrm{Pe_k} \to \infty. \tag{5.87}$$

This result is agreement with the conclusion (5.19) (which we made after performing a local analysis of the lens and kinetics-based models) about the way in which kinetic effects regularize the mass-flux singularity. In particular, this tells us, via (5.44), that the evaporation rate at the contact line $E(1^-)$ is given by

$$E(1^-) \sim C_O {\mathrm{Pe_k}}^{1/2} = \left(\frac{2\mathrm{Pe_k}}{\pi} \right)^{1/2} \quad \text{as } \mathrm{Pe_k} \to \infty. \tag{5.88}$$

Thus our matched-asymptotic expansion is in agreement with the numerics for the exact solution; in our prediction (5.35) for the large-$\mathrm{Pe_k}$ behaviour of $E(1^-)$, we have $\alpha = (2/\pi)^{1/2} \approx 0.798$, which is presented as the horizontal dashed line in figure 5.1(c).

From the expressions (5.37) and (5.85) for the evaporation rate in the outer and inner regions, respectively, we deduce that a leading-order additive composite expansion for the evaporation rate $E(\widehat{r}\,)$, uniformly valid for $0 \leq \widehat{r} < 1$ as $\mathrm{Pe_k} \to \infty$, is given by

$$E(\widehat{r}\,) \sim \frac{2}{\pi(1-\widehat{r}^{\,2})^{1/2}} + \frac{(2\mathrm{Pe_k})^{1/2}}{\pi^{3/2}} \int_0^\infty \frac{I(t) e^{-\mathrm{Pe_k}(1-\widehat{r}\,)t}}{t^{1/2}(1+t^2)}\,\mathrm{d}t - \frac{2^{1/2}}{\pi(1-\widehat{r}\,)^{1/2}}. \tag{5.89}$$

5.5.4 Validation of asymptotic results

We shall now validate our leading-order asymptotic predictions against the finite-$\mathrm{Pe_k}$ solutions that we obtained in §5.4. We shall consider the predictions for the total flux out of the drop Q, the evaporation rate at the contact line $E(1^-)$, and the evaporation rate $E(\widehat{r}\,)$ as a function of $\widehat{r}$.

In figure 5.2(a), we take the finite-$\mathrm{Pe_k}$ solution for the total flux Q and plot $\mathrm{Pe_k}(4-Q)$ as a function of $\log_{10}(\mathrm{Pe_k})$. For large values of $\mathrm{Pe_k}$ (between 10^2 and 10^4) we fit a linear relationship, which we plot on the same axes. We see that for the physically realistic values of $\mathrm{Pe_k}$ (40 and higher; see table 5.1), there is very good agreement between the fit and the data. This gives us confidence that the leading-order asymptotic prediction (5.86) is correct, with

$$Q \sim 4 - \frac{A\log(\mathrm{Pe_k}) + B}{\mathrm{Pe_k}} \quad \text{as } \mathrm{Pe_k} \to \infty, \tag{5.90}$$

where log now denotes the logarithm of base e as usual, and we find numerically that $A \approx 1.28$ and $B \approx 2.85$. We do not investigate further such higher-order terms.

We plot the finite-$\mathrm{Pe_k}$ solution for the evaporation rate at the contact line $E(1^-)$, given by (5.30), as a function of $\mathrm{Pe_k}$ in figure 5.2(b). On the same axes we plot the leading-order asymptotic prediction (5.88). We see that there is good agreement between the solutions even for moderately large values of $\mathrm{Pe_k}$. We note that both the form of the asymptote (5.88) and its validity for moderately large kinetic Péclet numbers are consistent with the observations that we made about the finite-$\mathrm{Pe_k}$ solution following figure 5.1(c).

To evaluate numerically the leading-order composite expansion for the evaporation rate (5.89), we first write the function $I(t)$, given by (5.84), as

$$I(t) = (1+t^2)^{1/4} \exp\left[\frac{1}{\pi}\int_t^\infty \frac{\log(s)\,\mathrm{d}s}{1+s^2}\right], \tag{5.91}$$

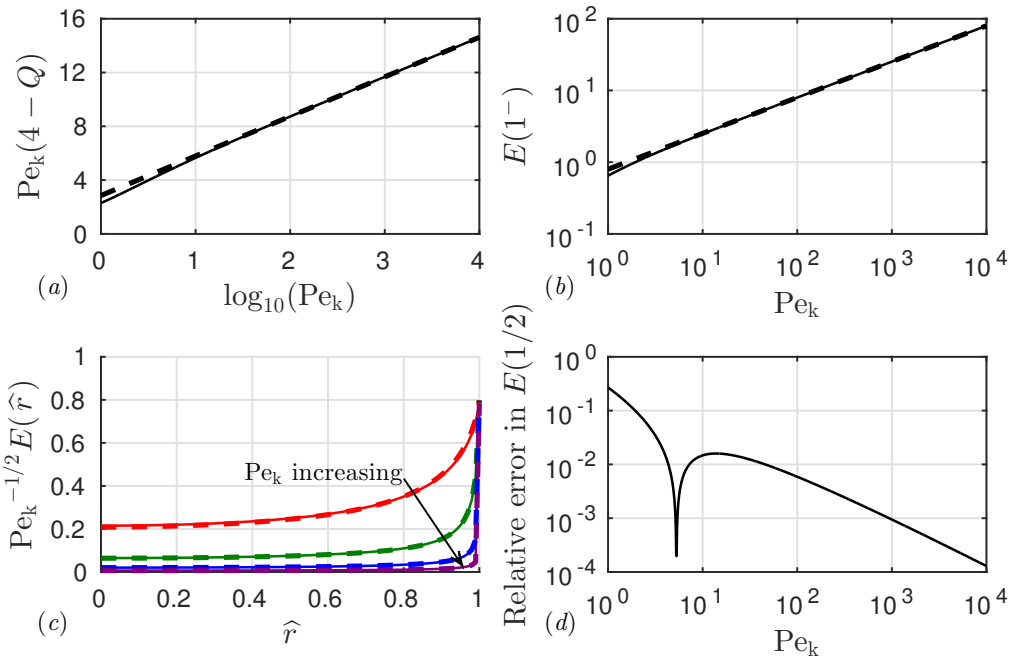

Figure 5.2: Validation of the leading-order asymptotic results (5.86), (5.88), and (5.89) against the finite-$\mathrm{Pe_k}$ solutions. In (a), we plot $\mathrm{Pe_k}(4-Q)$ as a function of $\log_{10}(\mathrm{Pe_k})$. The solid curve is the finite-$\mathrm{Pe_k}$ solution (5.33), while the dashed line is a linear fit for large values of $\mathrm{Pe_k}$ (between 10^2 and 10^4). In (b) we plot the evaporation rate at the contact line $E(1^-)$ as a function of $\mathrm{Pe_k}$. The solid curve is the finite-$\mathrm{Pe_k}$ solution (5.30), while the dashed line is the large-$\mathrm{Pe_k}$ asymptote (5.88). (c) Scaled evaporation rate $\mathrm{Pe_k}^{-1/2}E(\widehat{r})$ as a function of $\widehat{r}$ for $\mathrm{Pe_k} = 10^1, 10^2, 10^3, 10^4$ (red, green, blue, and purple, respectively). The solid curves are the finite-$\mathrm{Pe_k}$ solution (5.29) and the dashed curves show the leading-order asymptotic prediction (5.92). (d) The relative error in $E(1/2)$ between the finite-$\mathrm{Pe_k}$ solution (5.29) and the leading-order asymptotic prediction (5.92).

so that the integrand in (5.91) is bounded at the endpoints of the integration range. We then make the substitution $t = \tau^2$ in order to remove the integrable singularity in the integrand of the second term in (5.89); we obtain, as $\mathrm{Pe_k} \to \infty$,

$$E(\widehat{r}\,) \sim \frac{2^{1/2}[2^{1/2} - (1+\widehat{r}\,)^{1/2}]}{\pi(1-\widehat{r}^{\,2})^{1/2}} + \frac{2^{3/2}{\mathrm{Pe_k}}^{1/2}}{\pi^{3/2}} \int_0^\infty \frac{U(\tau;\widehat{r},\mathrm{Pe_k})}{(1+\tau^4)^{3/4}}\,\mathrm{d}\tau,$$
$$\text{with } U(\tau;\widehat{r},\mathrm{Pe_k}) = \exp\left[-\mathrm{Pe_k}(1-\widehat{r}\,)\tau^2 + \frac{1}{\pi}\int_{\tau^2}^\infty \frac{\log(s)\,\mathrm{d}s}{1+s^2}\right]. \tag{5.92}$$

The integrals in (5.92) are computed in MATLAB with the same methods used in the evaluation of (5.29). We plot the composite evaporation rate (5.92) as a function of $\widehat{r}$ for $\mathrm{Pe_k} = 10^1, 10^2, 10^3, 10^4$ in figure 5.2(*c*). On the same axes we plot the finite-$\mathrm{Pe_k}$ solutions (5.29); we see good agreement between the two solutions even for only moderately large values of $\mathrm{Pe_k}$. In figure 5.2(*d*), we plot the relative error in $E(1/2)$ between the finite-$\mathrm{Pe_k}$ solution (5.29) and the leading-order asymptotic prediction (5.92). The sharp dip in figure 5.2(*d*) is because for $\mathrm{Pe_k} = \mathrm{O}(1)$, the asymptotic prediction is an overestimate, while for large $\mathrm{Pe_k}$, it is an underestimate (*i.e.* the correction changes sign). For physically realistic values of the kinetic Péclet number (see table 5.1), the relative error in $E(1/2)$ is below 2% and is a decreasing function of $\mathrm{Pe_k}$, illustrating very good agreement between the two solutions (5.29) and (5.92).

5.6 Summary

Our first aim in this chapter was to investigate how the mass-flux singularity at the contact line of a thin, evaporating drop is regularized by applying a linear constitutive law on the liquid–gas interface that takes kinetic effects into account. Our second aim was to derive an explicit expression for the evaporation rate.

In §2, we formulated a model for the transport of liquid vapour within the gas phase, assuming that the vapour concentration is steady, there is no flux of vapour through the solid substrate, the mass flux through the liquid–gas interface is governed by a linear, kinetics-based constitutive law, and the diffusion coefficient and the equilibrium and far-field vapour concentrations are all constant. The model was non-dimensionalized, leaving us with a single dimensionless parameter, the kinetic Péclet number $\mathrm{Pe_k}$ (the ratio of the timescales of diffusive and kinetic effects). We tabulated values of the physical parameters for hexane, isopropanol and HFE-7100 and saw that $\mathrm{Pe_k}$ was typically large for all but the smallest drops.

In §5.3, we performed a local analysis in the vicinity of the contact line on the kinetics-based model and also on the more standard lens evaporation model (which

leads to a mass-flux singularity at the contact line). This demonstrated the vapour concentration at the contact line $c_L(\mathrm{Pe_k})$ in the kinetics-based model was key to how the mass-flux singularity is regularized, with $c_L \to 1^-$ as $\mathrm{Pe_k} \to \infty$, but with $c_L < 1$ for finite $\mathrm{Pe_k}$. This motivated the need to solve the mixed-boundary-value problem formulated in §2 and determine the degree of freedom c_L.

In §5.4, we solved the mixed-boundary-value problem and deduced an expression for the mass flux in terms of a set of coefficients that satisfy a system of infinitely many linear algebraic equations. This accomplishes one of the two aims of this chapter. Analysis of the expression for the mass flux confirmed the hypotheses made in §5.3 about the degree of freedom c_L and how the mass-flux singularity is regularized by kinetic effects. Our numerical simulations suggested that there was a boundary layer close to the contact line in which the evaporation rate was of size $\mathrm{O}(\mathrm{Pe_k}^{1/2})$ as $\mathrm{Pe_k} \to \infty$. This motivated us to further analyze the physically relevant limit of large kinetic Péclet number.

In §5.5, we performed a matched-asymptotic analysis of our model in the physically relevant regime of large kinetic Péclet number. We found that the asymptotic structure of the problem consists of an outer region away from the contact line, in which the vapour immediately above the liquid–gas interface is at equilibrium to leading order (as is assumed in the lens model). However, there is also an inner region near the contact line, in which kinetic effects enter at leading order. The leading-order-outer problem is equivalent to the lens model, while the leading-order-inner problem was solved readily using the Wiener-Hopf method. We found that the assumption that the vapour immediately above the drop surface is at thermodynamic equilibrium is valid in the outer region, with the mass-flux singularity being regularized in the inner region. We deduced from our leading-order asymptotic solution that $c_L \sim 1 - (2/\pi)^{1/2}\mathrm{Pe_k}^{-1/2}$ as $\mathrm{Pe_k} \to \infty$, quantifying the way in which kinetic effects regularize the mass-flux singularity. This accomplishes the other of the two aims for this chapter. We also constructed a leading-order additive composite expansion and validated this asymptotic prediction by comparison with the solution found in §5.4; we found good agreement for physically realistic values of the kinetic Péclet number. Thus, for such values of the kinetic Péclet number, either solution for the mass flux may be used as an input to a model for the evolution of a liquid drop.

5.7 The liquid phase

In this section, we give some brief details about the typical mathematical model for the liquid phase. We use this model to show explicitly that the lens model leads to a singularity in the liquid velocity, while no such singularity is present for the kinetics-based model. We then move on to briefly discuss our predictions for the evolution of the drop.

5.7.1 Formulation

In chapter 2, we derived the thin-film equation (2.4) for the evolution of the drop profile $h^*(r^*, t^*)$. The problem for the liquid phase is not quasi-steady, so we use the initial contact-set radius $R = s^*(0)$ as a typical lengthscale for non-dimensionalization, as in chapter 2. We non-dimensionalize as in chapter 2, and also set $E^* = DM(c_e - c_\infty)\widehat{E}/R$ (so that $\widehat{E} = E/s$), where the typical timescale of capillary action τ_C is defined as in chapter 2. We obtain the dimensionless thin-film equation

$$\frac{\partial h}{\partial t} + \frac{1}{r}\frac{\partial}{\partial r}(rh\overline{u}) = -\widehat{\alpha}\widehat{E} \quad \text{for } 0 < r < s, \tag{5.93}$$

where $\widehat{\alpha} = \pi\alpha/2$, with α as defined in chapter 2. Assuming that there is no flux of liquid through the contact line, appropriate boundary conditions subject to which to solve the thin-film equation (5.93) are given by (2.21).

We deduce from the thin-film equation (5.93) and the no-flux boundary conditions ($2.21b, e$) that the expression representing global conservation of mass of the drop is given by

$$\frac{\mathrm{d}V}{\mathrm{d}t} = -\widehat{Q}; \quad V = 2\pi\int_0^s rh\,\mathrm{d}r,\ \widehat{Q} = 2\pi\int_0^s r\widehat{E}\,\mathrm{d}r, \tag{5.94}$$

where V is the (dimensionless) volume of the drop and $\widehat{Q} = sQ$ is the total (dimensionless) mass flux out of the drop per unit time.

5.7.2 Local analysis

To put our analysis of the lens and kinetics-based models into context, let us first consider the case of no evaporation ($\widehat{E} = 0$). A local analysis of the thin-film equation (5.93) subject to the boundary conditions ($2.21c - e$) reveals that

$$\overline{u} \sim \dot{s} \quad \text{as } r \to s^-, \tag{5.95}$$

where $\dot{s} = \mathrm{d}s/\mathrm{d}t$. It has previously been shown that implies that there is a stress singularity at a moving contact line (Huh and Scriven, 1971).

Let us next consider the lens evaporation model. We write the local expansion (5.15) for the evaporation rate near the contact line in terms of liquid variables:

$$\widehat{E} \sim \frac{2^{1/2}}{\pi(s-r)^{1/2}} \quad \text{as } r \to s^-. \tag{5.96}$$

A local analysis of the thin-film equation (5.93) subject to the boundary conditions $(2.21c-e)$ therefore reveals that

$$\overline{u} \sim \frac{2^{1/2}\widehat{\alpha}}{s^{1/2}(s-r)^{1/2}} \quad \text{as } r \to s^-; \tag{5.97}$$

there is an inverse-square-root singularity in the depth-averaged radial velocity at the contact line. Thus, the local expansion (5.97) for $\overline{u}$ implies that there is a stress singularity at the contact line, stronger than the classical one for a moving contact line in the absence of evaporation, and that this singularity is present even when the contact line is pinned.

Let us now consider the kinetics-based evaporation model. We write the local expansion (5.17) for the evaporation rate near the contact line in terms of liquid variables:

$$\widehat{E} \sim E_L := \frac{\mathrm{Pe_k}[1 - c_L(\mathrm{Pe_k})]}{s} \quad \text{as } r \to s^-. \tag{5.98}$$

A local analysis of the thin-film equation (5.93) subject to the boundary conditions $(2.21c-e)$ therefore reveals that

$$\overline{u} \sim \dot{s} + \widehat{\alpha}E_L \quad \text{as } r \to s^-. \tag{5.99}$$

Thus, for the kinetics-based model, there is no singularity in the depth-averaged radial velocity at the contact line. We note that the local expansion (5.99) for $\overline{u}$ implies that the stress singularity at the contact line has the same strength as the one for moving contact lines in the absence of mass transfer (Huh and Scriven, 1971). Moreover, it is present for both moving and pinned contact lines (with a different coefficient in each of the two cases).

5.7.3 Evolution of the drop

We now give predictions for the evolution of both pinned drops and drops with moving contact lines. For a pinned drop, the evolution of the drop volume is fully described by the global conservation of mass equation (5.94). We have seen that, in the physically relevant limit when kinetic effects are weak compared to diffusive effects, the leading-order total flux out of the drop per unit time is the same for the kinetics-based model and the lens model.

For a drop with a moving contact line, we expect an important factor in determining the effect of kinetics to be the relative widths of the inner region in which kinetic effects come into play and the region in which the force singularity at a moving contact line is regularized. If the kinetic region is smaller, presumably the only noticeable effect of kinetics is to regularize the mass-flux singularity, while the remainder of the drop dynamics is the same as the lens model (which we have shown is the leading-order approximation to the lens model away from the contact line when kinetic effects are weak compared to diffusive effects). On the other hand, if the kinetic region is at least as large as the region in which the force singularity is regularized, we expect that kinetics will have a more significant effect on the drop dynamics. Analysis of the drop dynamics for the lens model (see chapters 3 and 4) suggests that this effect may be through an effective microscopic contact angle (different to both the true microscopic contact angle and the effective one for the lens model) that appears in the contact-line law.

5.A Evaporation rate at the contact line

To determine the evaporation rate at the contact line $E(1^-)$, we set $x = \cos(\delta X)$ and $\widehat{r} = \cos(\delta)$ in (5.29) to obtain

$$E(\cos(\delta)) = \sum_{n=0}^{\infty}(2n+1)a_n(\mathrm{Pe_k})I_n(\delta), \quad I_n(\delta) = \delta\int_0^1 \frac{\cos[(2n+1)\delta X]}{[\cos^2(\delta X)-\cos^2(\delta)]^{1/2}}\,\mathrm{d}X. \tag{5.100}$$

We now take the limit $\delta \to 0^+$ (corresponding to $\widehat{r} \to 1^-$) of (5.100). We use the small-argument expansion for the cosine terms in the denominator (but not the numerator) to obtain, as $\delta \to 0^+$,

$$I_n(\delta) = \int_0^1 \frac{\cos[(2n+1)\delta X]}{(1-X^2)^{1/2}} + \mathrm{O}(\delta^2) = \frac{\pi}{2}J_0[(2n+1)\delta] + \mathrm{O}(\delta^2), \tag{5.101}$$

where J_0 is the Bessel function of first kind of order zero. Truncating the infinite sum in (5.100) at $n = N(\delta)$, where $N(\delta)$ is an integer chosen such that $1 \ll N(\delta) \ll \delta^{-2/3}$ as $\delta \to 0^+$ (for reasons that will become apparent shortly), we obtain

$$E(\cos(\delta)) = \frac{\pi}{2}\sum_{n=0}^{N(\delta)}(2n+1)a_n(\mathrm{Pe_k})J_0[(2n+1)\delta] + \mathcal{E}(\delta) \quad \text{as } \delta \to 0^+, \tag{5.102}$$

where $\mathcal{E}(\delta)$ is an error term that we estimate below. Since $\delta N(\delta) \ll 1$ as $\delta \to 0^+$ with $N(\delta)$ chosen as described above, we apply the small-argument expansion of the

Bessel function, truncated to its first term, and absorb the associated error into $\mathcal{E}(\delta)$. We then extend the sum to an infinite number of terms and absorb into $\mathcal{E}(\delta)$ the error thus introduced; we obtain

$$E(\cos(\delta)) = \frac{\pi}{2}\sum_{n=0}^{\infty}(2n+1)a_n(\mathrm{Pe_k}) + \mathcal{E}(\delta) \quad \text{as } \delta \to 0^+, \tag{5.103}$$

since $J_0(0) = 1$. The first term on the right-hand side of (5.103) is of order-unity size as $\delta \to 0^+$. Therefore, provided that the error term $\mathcal{E}(\delta) = \mathrm{o}(1)$ as $\delta \to 0^+$, the evaporation rate at the contact line $E(1^-)$ is given by (5.30).

It remains to estimate the error term $\mathcal{E}(\delta)$. The first contribution comes from truncating the infinite sum at $n = N(\delta)$. In §5.4.2, we present numerical evidence that $a_n = \mathrm{O}(n^{-4})$ as $n \to \infty$ (see figure 5.1*a*). Assuming this to be the case, we deduce from the Euler-Maclaurin formula and the boundedness of the Bessel function J_0 that the truncation error is no larger than $\mathrm{O}(N^{-2})$ as $N \to \infty$. Since $N(\delta) \gg 1$ as $\delta \to 0^+$, this contribution is of size $\mathrm{o}(1)$, as required. The second contribution comes from using only the leading term in the expansion (5.101) for $I_n(\delta)$. The error term is of size $\mathrm{O}(\delta^2)$ as $\delta \to 0^+$ and there are $N+1$ terms in the sum, so the contribution is of size $\mathrm{O}(\delta^2 N)$. Since $\delta^2 N(\delta) \ll 1$ as $\delta \to 0$ with $N(\delta)$ chosen as described above, the second contribution is of size $\mathrm{o}(1)$, as required. The third contribution comes from truncating the small-argument expansion of the Bessel function at its first term. This introduces into the n^{th} term in the sum an error of size $\mathrm{O}(n^2\delta^2)$ as $\delta \to 0^+$. The contribution from all $(N+1)$ terms is therefore no larger than $\mathrm{O}(N^3\delta^2)$ as $\delta \to 0^+$. Since $N(\delta) \ll \delta^{-2/3}$ as $\delta \to 0^+$ (by assumption), the third contribution is of size $\mathrm{o}(1)$, as required. The final contribution comes from extending the sum to an infinite number of terms. This contribution is no larger than $\mathrm{O}(N^{-2})$ as $N \to \infty$, for the same reasons as for the first contribution, and is therefore of size $\mathrm{o}(1)$ as $\delta \to 0^+$. We therefore conclude that $\mathcal{E}(\delta) = \mathrm{o}(1)$ as $\delta \to 0^+$, as required.

5.B Details of the Wiener-Hopf calculation

5.B.1 An Abelian Theorem

We are often interested in the domains of holomorphy of the one-sided Fourier transforms of a function $f(x)$ (5.46), as well as their behaviour as $k \to \infty$. This behaviour is dominated by the behaviour of $f(x)$ as $x \to 0$, as described by the following two results (Crighton *et al.*, 1992).

(i) Suppose $f(x) = 0$ for $x < 0$, $|f(x)| < Ae^{ax}$ as $x \to \infty$, for some constants A and a, f is infinitely differentiable for $x > 0$, and $f(x) \sim x^\lambda$ as $x \to 0^+$, for some $\lambda > -1$. Then $\overline{f}_+(k)$ is holomorphic in $\Im(k) > a$, with

$$\overline{f}_+(k) \sim \int_0^\infty x^\lambda e^{ikx}\,\mathrm{d}x = \frac{\lambda!}{(-ik)^{\lambda+1}} \quad \text{as } k \to \infty \text{ in } \Im(k) > a. \tag{5.104}$$

(ii) Suppose $f(x) = 0$ for $x > 0$, $|f(x)| < Be^{bx}$ as $x \to -\infty$, for some constants B and b, f is infinitely differentiable for $x < 0$, and $f(x) \sim (-x)^\mu$ as $x \to 0^-$, for some $\mu > -1$. Then $\overline{f}_-(k)$ is holomorphic in $\Im(k) < b$, with

$$\overline{f}_-(k) \sim \int_{-\infty}^0 (-x)^\mu e^{ikx}\,\mathrm{d}x = \frac{\mu!}{(ik)^{\mu+1}} \quad \text{as } k \to \infty \text{ in } \Im(k) < b. \tag{5.105}$$

5.B.2 Wiener-Hopf product factorization

We now outline the details of the Wiener-Hopf product factorization (5.70). With our choice of branch for $(k^2+\varepsilon^2)^{1/2}$, defined by (5.63)–(5.65), the left-hand side of (5.70) is holomorphic and non-zero in the strip $-\varepsilon < \Im(k) < \varepsilon$, and tends to unity as $k \to \infty$ in this strip. Moreover, the image of the strip under log, the principal branch of the logarithm, does not encircle the branch point at the origin. We therefore apply the general method of Carrier *et al.* (2005) and take logarithms to change the problem from a product decomposition to an additive decomposition. We find that

$$\log P_\pm^\varepsilon(k) = \frac{1}{2\pi i}\int_{\Gamma_\pm} \frac{\log[1+(\zeta^2+\varepsilon^2)^{-1/2}]}{\zeta - k}\,\mathrm{d}\zeta \quad \text{for } \gamma_+ < \Im(k) < \gamma_-, \tag{5.106}$$

where $\Gamma_\pm = \{\zeta \in \mathbb{C} : \zeta = x + i\gamma_\pm,\ x \in \mathbb{R}\}$, with the real numbers $\gamma_\pm$ chosen such that $-\varepsilon < \gamma_+ < \gamma_- < \varepsilon$. We note that, by construction, $P_\pm^\varepsilon(k) \to 1$ as $k \to \infty$. Following Duffy (2008), we deform Γ_+ into the lower half-plane with a 'keyhole' incision around the branch cut S_- and Γ_- into the upper half-plane with an incision around the branch cut S_+. We deduce thereby that $P_\pm^\varepsilon(k)$ is holomorphic for $k \in \mathbb{C} \setminus S_\mp$, with

$$P_\pm^\varepsilon(k) = \exp\left(\pm\frac{1}{2\pi}\int_\varepsilon^\infty \frac{1}{i\sigma \pm k}\log\left[\frac{1+i(\sigma^2-\varepsilon^2)^{-1/2}}{1-i(\sigma^2-\varepsilon^2)^{-1/2}}\right]\mathrm{d}\sigma\right) \quad \text{for } k \in \mathbb{C}\setminus S_\mp. \tag{5.107}$$

It follows from (5.107) that

$$P_\pm(\pm it) = t^{\mp 1/2}(1+t^2)^{\pm 1/4}\exp\left(\mp\frac{1}{\pi}\int_0^t \frac{\log(s)}{1+s^2}\,\mathrm{d}s\right) \quad \text{for } t > 0. \tag{5.108}$$

By analytic continuation off the imaginary axis, we deduce that

$$P_+(k) \sim e^{i\pi/4}k_+^{-1/2} \quad \text{as } k \to 0,\ \Im(k) > 0, \tag{5.109}$$

$$P_-(k) \sim e^{i\pi/4}k_-^{1/2} \quad \text{as } k \to 0,\ \Im(k) < 0, \tag{5.110}$$

where $k_+^{-1/2} = k_+^{3/2}/k^2$, with $k_+^{3/2}$ as defined in (5.51), and $k_-^{1/2}$ is defined in (5.52).

5.B.3 Inversion to find $C(X,Y)$

In this appendix, we shall invert the Fourier transform in X of $\partial C^\varepsilon/\partial X(X,Y)$, which by (5.73) is given by

$$\overline{F}^\varepsilon(k,Y) = C_O^\varepsilon[P_+^\varepsilon(k) - P_-^\varepsilon(k)]e^{-(k^2+\varepsilon^2)^{1/2}Y}, \tag{5.111}$$

Applying the inversion theorem gives

$$F^\varepsilon(X,Y) = \frac{C_O^\varepsilon}{2\pi}\int_\Gamma [P_+^\varepsilon(k) - P_-^\varepsilon(k)]e^{-(k^2+\varepsilon^2)^{1/2}Y - ikX}\,\mathrm{d}k, \tag{5.112}$$

where the inversion contour Γ runs along the real axis.

For $X < 0$, we deform Γ into the upper half-plane, where $\Re[-(k^2+\varepsilon^2)^{1/2}Y - ikX] < 0$, around the branch cut S_+ and write $P_+^\varepsilon(k) + P_-^\varepsilon(k) = P_+^\varepsilon(k)/[1 + (k^2+\varepsilon^2)^{1/2}]$, since $P_+^\varepsilon(k)$ is continuous across S_+. After taking the limit $\varepsilon \to 0^+$, we obtain

$$\frac{\partial C}{\partial X}(X,Y) = \frac{2^{1/2}}{\pi^{3/2}}\int_0^\infty \frac{I(t)[\sin(tY) + t\cos(tY)]e^{tX}}{t^{1/2}(1+t^2)}\,\mathrm{d}t \quad \text{for } X < 0, \tag{5.113}$$

with $I(t)$ as defined in (5.84). We then integrate (5.113) with respect to X and use the far-field condition (5.41) to deduce that

$$C(X,Y) = \frac{2^{1/2}}{\pi^{3/2}}\int_0^\infty \frac{I(t)[\sin(tY) + t\cos(tY)]e^{tX}}{t^{3/2}(1+t^2)}\,\mathrm{d}t \quad \text{for } X < 0. \tag{5.114}$$

We note that it is readily shown that (5.114) is in agreement with (5.83) when $Y = 0$.

For $X > 0$, we deform Γ into the lower half-plane, where $\Re[-(k^2+\varepsilon^2)^{1/2}Y - ikX] < 0$, around the branch cut S_- and write $P_+^\varepsilon(k) + P_-^\varepsilon(k) = P_-^\varepsilon(k)/(k^2+\varepsilon^2)^{1/2}$, since $P_-^\varepsilon(k)$ is continuous across S_-. After taking the limit $\varepsilon \to 0^+$, we obtain

$$\frac{\partial C}{\partial X}(X,Y) = \frac{2^{1/2}}{\pi^{3/2}}\int_0^\infty \frac{\cos(tY)e^{-tX}}{t^{1/2}I(t)}\,\mathrm{d}t \quad \text{for } X > 0. \tag{5.115}$$

We then integrate (5.115) with respect to X from $X = 0$, demanding continuity of C for $X = 0$, $Y \geq 0$, using (5.114), to deduce that

$$C(X,Y) = C(0^-,Y) + \frac{2^{1/2}}{\pi^{3/2}}\int_0^\infty \frac{\cos(tY)(1-e^{-tX})}{t^{3/2}I(t)}\,\mathrm{d}t \quad \text{for } X \geq 0. \tag{5.116}$$

We note that direct differentiation of (5.114) shows that it satisfies Laplace's equation (5.38) for $X < 0$, $Y > 0$ and the boundary condition (5.39). Although we have

constructed a solution that is continuous across $X = 0, Y \geq 0$, we have been unable to verify that $C(X, Y)$ satisfies Laplace's equation everywhere in $Y > 0$ by a method other than the constructive one presented above. We note that, given the expression (5.83) for $C(X, 0)$ for $X < 0$, the inner problem (5.38)–(5.41) becomes a Neumann problem, so that the solution may be obtained using standard Green's function or Fourier Transform methods (Ockendon *et al.*, 2003); however, the resulting form of the solution will inevitably involve a triple integral and therefore be less amenable to quadrature than the solution presented above. Finally, Laplace's method may be used to show that $C(X, Y)$ satisfies the far-field condition (5.41) for $\theta = 0$ and $\theta = \pi$, and it is readily checked that $C(X, 0)$ is infinitely differentiable on $(-\infty, 0) \cup (0, \infty)$ (as postulated in §5.5.2.2) and continuous and non-zero at $X = 0$ (as postulated in §5.5.2.1).

Chapter 6

Discussion

6.1 Summary

In chapter 2 we derived a thin-film model for an axisymmetric evaporating drop that takes into account the effects of viscous dissipation, capillarity, slip, diffusion-dominated vapour transport, gravity, surface-tension gradients, and contact-angle hysteresis. We non-dimensionalized this model and listed typical values of the dimensionless parameters in order to identify the physically relevant parameter limits.

In chapter 3, we considered the question of when the d^2-law — that, close to extinction, the time remaining until the drop goes extinct is proportional to the square of the drop's diameter, d — is valid. To answer this question, we considered a simplified version of the model derived in chapter 2 (in which gravity, surface-tension gradients, and contact-angle hysteresis are neglected) and analysed this simplified model in the limit of small slip. We found that a key parameter is

$$\mathcal{E} = \frac{2^{1/2}\alpha}{\lambda^{1/2}}, \tag{6.1}$$

where α is the ratio of the timescales of capillary action and mass loss, and λ is the slip coefficient (the ratio of the typical slip length to the typical drop thickness). The parameter $\mathcal{E}$ may be viewed as a capillary number based on the liquid velocity induced by the evaporative flux in the inner region. When $\mathcal{E} = \mathrm{O}(1)$, a $d^{13/7}$-law replaces the d^2-law close to extinction. Moreover, when $\mathcal{E} \ll 1$ the d^2-law is valid for the entire timescale of mass loss except for a small temporal boundary layer close to extinction, where a $d^{13/7}$-law holds.

In chapter 4, we aimed to gain an understanding of what physical effects most influence the extinction time. We generalized the analysis of chapter 3 to consider the full version of the model derived in chapter 2 (taking gravity, surface-tension

gradients, and contact-angle hysteresis into account). We found that the extinction time increases slightly with $\mathcal{E}$, decreases slightly with the Bond number Bo, increases with the Marangoni number Ma, and increases with the contact-angle hysteresis Ψ_H. We presented the following physical reasoning to explain these trends. Increasing $\mathcal{E}$ or Ma pulls liquid away from the contact line so that the far-field (effective) microscopic contact angle increases. Increasing Bo causes gravity to flatten the centre of the drop; this pushes liquid towards the contact line and decreases the effective microscopic contact angle. Increasing Ψ_H increases the true microscopic contact angle, which in turn increases the effective microscopic contact angle. For a given drop volume, increasing the effective microscopic contact angle decreases the equilibrium contact-set radius that the drop attains on the timescale of contact-line motion, before it begins to lose mass. Since the total mass flux out of the drop is proportional to its radius, having a smaller radius (for a given volume) means that the drop takes longer to evaporate and thus has a larger extinction time.

In chapter 5, we replaced the diffusion-dominated evaporation model used in chapters 2–4 with a kinetics-based linear constitutive law, since the latter does not have a singularity in the evaporation rate at the contact line. Our first aim was to understand how kinetic effects regularize the mass-flux singularity at the contact line. In the physically relevant limit, in which the timescale of vapour diffusion is much longer than the timescale of kinetic effects, we found that there is a small boundary layer in the vicinity of the contact line in which kinetics have a leading-order effect and the mass-flux singularity is regularized. Our second aim was to derive an explicit expression for the evaporation rate associated with the kinetics-based model. By drawing an analogy with a thermal mixed-boundary-value problem, we obtained such an expression in terms of a set of coefficients that satisfy an infinite system of linear algebraic equations; we solved this system numerically.

6.2 Future work

6.2.1 Major questions

We noted in chapter 1 that near-extinction behaviour differing slightly from the d^2-law has been observed experimentally. However, it is not clear whether this behaviour is systematic or an artefact of experiments. In particular, Shahidzadeh-Bonn *et al.* (2006) saw power-law behaviour of the form $s(t) \sim A(t_e - t)^\beta$ as $t \to t_e^-$, with $\beta \approx 0.47$ for hexane and $\beta \approx 0.6$ for water (for comparison, $7/13 \approx 0.54$). For hexane, we find that the physically relevant regime has $\mathcal{E} \ll 1$, so that the d^2-law

should be valid, while we have already noted that our model is not expected to apply to water drops. We have therefore not been able to answer the question of whether these results are artefacts of experiment. However, we have predicted that systematic behaviour slightly different to a d^2-law is possible. To our knowledge, this is the first suggestion that the exponent may be modified by hydrodynamics, and so comparison with experimental data is an important direction for future research.

We note that it would be extremely difficult to directly differentiate experimentally between a d^2-law and a $d^{13/7}$-law since the latter is only expected to be valid near to extinction; during this small period of time, the difference in predicted contact-set radii for two similar power-law exponents is expected to be too small to be measured. Fitting the power-law coefficient, given by (3.35), is not a solution to this problem, since it has only a weak dependence on $\mathcal{E}$. However, it would be worthwhile to compare the predictions of our model for the contact-set radius and drop volume over the timescale of mass loss, as well as for the extinction time, with experimental data; our model predicts that these three quantities differ appreciably with $\mathcal{E}$. Another avenue for future work would be the use of molecular dynamics simulations to study independently the evaporation rate at times close to extinction.

A second key direction for future work is to incorporate the explicit expression for the kinetics-based mass flux into a model for the evolution of the liquid drop. This would allow us to obtain predictions for the extinction time, the evolution of the drop volume (or, equivalently, the dynamic contact angle or drop thickness), and, in the case of a moving contact line, the evolution of the contact-set radius within this model. Previous theoretical work has obtained such predictions for the lens evaporation model (Dunn *et al.*, 2008; Murisic and Kondic, 2011; Poulard *et al.*, 2005) and for other evaporation models (Ajaev, 2005; Anderson and Davis, 1995; Dunn *et al.*, 2009b,c; Hocking, 1995; Murisic and Kondic, 2008, 2011; Sáenz *et al.*, 2015; Semenov *et al.*, 2014; Sodtke *et al.*, 2007). In particular, it would be informative to compare the predictions of this previous work to the corresponding predictions for our model. This comparison would give us some indication of what net result the inclusion of kinetic effects has beyond regularizing the mass-flux singularity.

6.2.2 Additional questions

Throughout this thesis, we assumed that the problem is axisymmetric. In the non-axisymmetric case, provided that the contact line is smooth, we expect that the details of the inner region would be the same in each plane perpendicular to the contact line.

It would be interesting to investigate this point further and compare the results to previous work on non-axisymmetric drops (Sáenz *et al.*, 2015).

We regularized the force singularity at the contact line by replacing the usual no-slip boundary condition with a generalized Navier slip law. Another popular regularization is to assume that there is a precursor film that wets the substrate ahead of the drop. An area of interest for future work would be to see what aspects of the analysis in this thesis carry over to a model with a precursor regularization and to examine the near-extinction behaviour that may be extracted from such a model.

Both the lens model used in chapters 2–4 and the kinetics-based model used in chapter 5 require the diffusion of vapour in the gas phase to be quasi-steady; this assumption is valid if the typical timescale of diffusion τ_D is smaller than the timescale of capillary action τ_C. Since $\tau_D/\tau_C \propto R$, this places an upper bound on the initial contact-set radius R. From tables 2.2 and 2.3, we see that drops with a radius below this critical value tend to have a small Bond number (there is no restriction on the Marangoni number Ma, since it is independent of R). A model valid when $\tau_D \sim \tau_C$ would therefore be valuable so that drops with $\mathrm{Bo} = \mathrm{O}(1)$ can be considered. If $\tau_D \sim \tau_C$, Laplace's equation must be replaced by the unsteady diffusion equation. The resulting problem for the vapour concentration has been solved analytically by Abdelrazaq (2006); we expect the solution to converge in the long-time limit to the solution of the steady problem. Consequently, provided $\tau_D \ll \tau_M$ (an assumption that is generally true in practice), the conclusions regarding the $d^{13/7}$-law should still hold, although the details of the earlier evolution would be different. A more thorough study of vapour transport would be an interesting direction for future work. Such further study is particularly relevant for water, where it is possible that convection in the gas phase is important (Carrier *et al.*, 2016; Sefiane *et al.*, 2009; Shahidzadeh-Bonn *et al.*, 2006).

In both models, we also made the assumption that the equilibrium vapour concentration is constant; this is reasonable in the isothermal case, but a temperature-dependent equilibrium vapour concentration would be more appropriate in many experimentally relevant scenarios. In this case, the appropriate modification of the kinetics-based constitutive law for a thin liquid phase (in which case the interfacial temperature variation may be assumed to be small) (Sultan *et al.*, 2005) is not independent of the drop thickness. If temperature is assumed to vary, previous work has shown that the conductivity of the solid substrate may be an important factor (Dunn *et al.*, 2009c,a). A more thorough investigation of the temperature-dependence of the mass flux would therefore be of interest.

The correction terms in our asymptotic analysis in chapters 3 and 4 are of size $O(1/\log(1/\lambda))$: they are only logarithmically smaller than the leading-order terms. It would therefore be useful to undertake an error analysis to determine the accuracy of our asymptotic predictions for the contact-set radius, drop volume, and extinction time as $\lambda \to 0$. We observed that the slip exponent n affects the leading-order asymptotic predictions, but considered only the cases $n = 1$ and $n = 2$ and did not predict a general trend for how the contact-set radius, drop volume, and extinction time depend on n. This would also be an interesting direction for future analysis.

Finally, our analysis in chapter 4 assumed that the Bond and Marangoni numbers were not large. We saw from table 2.3 that this is a physically realistic assumption. However, it would still be interesting to see how our analysis changes when the effects of either gravity or surface-tension gradients dominate capillarity. In particular, it would be interesting to compare our results to those for gravity-driven spreading in the absence of evaporation (Hocking, 1983), in which the asymptotic structure is different to that presented here.

References

Abdelrazaq, N. (2006). The solution of heat conduction equation with mixed boundary conditions. *J. Math. Stat*, **2**, 346–350.

Ajaev, V. S. (2005). Spreading of thin volatile liquid droplets on uniformly heated surfaces. *J. Fluid Mech.*, **528**, 279–296.

Ajaev, V. S. and Homsy, G. M. (2001). Three-dimensional steady vapor bubbles in rectangular microchannels. *J. Colloid Interface Sci.*, **244**, 180–189.

Anderson, D. M. and Davis, S. H. (1995). The spreading of volatile liquid droplets on heated surfaces. *Phys. Fluids*, **7**, 248–265.

Bascom, W. D., Cottington, R. L., and Singleterry, C. R. (1963). Dynamic surface phenomena in the spontaneous spreading of oils on solids. Technical report, DTIC Document.

Bonn, D., Eggers, J., Indekeu, J., Meunier, J., and Rolley, E. (2009). Wetting and spreading. *Rev. Mod. Phys.*, **81**, 739–805.

Brochard-Wyart, F., di Meglio, J.-M., Quére, D., and de Gennes, P.-G. (1991). Spreading of nonvolatile liquids in a continuum picture. *Langmuir*, **7**, 335–338.

Burelbach, J. P., Bankoff, S. G., and Davis, S. H. (1988). Nonlinear stability of evaporating/condensing liquid films. *J. Fluid Mech.*, **195**, 463–494.

Cachile, M., Bénichou, O., Poulard, C., and Cazabat, A.-M. (2002). Evaporating droplets. *Langmuir*, **18**, 8070–8078.

Carrier, G. F., Krook, M., and Pearson, C. E. (2005). *Functions of a Complex Variable: Theory and Technique*. SIAM.

Carrier, O., Shahidzadeh-Bonn, N., Zargar, R., Aytouna, M., Habibi, M., Eggers, J., and Bonn, D. (2016). Evaporation of water: evaporation rate and collective effects. *J. Fluid Mech.*, **798**, 774–786.

Cazabat, A.-M. and Guéna, G. (2010). Evaporation of macroscopic sessile droplets. *Soft Matter*, **6**, 2591–2612.

Cercignani, C. (2000). *Rarefied gas dynamics: from basic concepts to actual calculations*. Cambridge University Press.

Colinet, P. and Rednikov, A. (2011). On integrable singularities and apparent contact angles within a classical paradigm. *Eur. Phys. J. Special Topics*, **197**, 89–113.

Crighton, D. G., Dowling, A. P., Ffowcs Williams, J. E., Heckl, M., and Leppington, F. G. (1992). *Modern Methods in Analytical Acoustics*. Springer–Verlag.

de Gennes, P.-G. (1985). Wetting: statics and dynamics. *Rev. Mod. Phys.*, **57**, 827–863.

Deegan, R. D., Bakajin, O., Dupont, T. F., Huber, G., Nagel, S. R., and Witten, T. A. (1997). Capillary flow as the cause of ring stains from dried liquid drops. *Nature*, **389**, 827–829.

Deegan, R. D., Bakajin, O., Dupont, T. F., Huber, G., Nagel, S. R., and Witten, T. A. (2000). Contact line deposits in an evaporating drop. *Phys. Rev. E*, **62**, 756–765.

Dondlinger, M., Margerit, J., and Dauby, P. C. (2005). Weakly nonlinear study of Marangoni instabilities in an evaporating liquid layer. *J. Colloid Interface Sci.*, **283**, 522–532.

Duffy, D. G. (2008). *Mixed boundary value problems*. CRC Press.

Dunn, G. J., Wilson, S. K., Duffy, B. R., David, S., and Sefiane, K. (2008). A mathematical model for the evaporation of a thin sessile liquid droplet: Comparison between experiment and theory. *Colloids Surf. A*, **323**, 50–55.

Dunn, G. J., Wilson, S. K., Duffy, B. R., and Sefiane, K. (2009a). Evaporation of a thin droplet on a thin substrate with a high thermal resistance. *Phys. Fluids*, **21**, 052101.

Dunn, G. J., Duffy, B. R., Wilson, S. K., and Holland, D. (2009b). Quasi-steady spreading of a thin ridge of fluid with temperature-dependent surface tension on a heated or cooled substrate. *Q. Jl. Mech. Appl. Math.*, **62**, 365–402.

Dunn, G. J., Wilson, S. K., Duffy, B. R., David, S., and Sefiane, K. (2009c). The strong influence of substrate conductivity on droplet evaporation. *J. Fluid Mech.*, **623**, 329–351.

Eggers, J. and Pismen, L. M. (2010). Nonlocal description of evaporating drops. *Phys. Fluids*, **22**, 112101.

Erbil, H. Y. (2012). Evaporation of pure liquid sessile and spherical suspended drops: A review. *Adv. Colloid Interf.*, **170**, 67–86.

Erbil, H. Y., McHale, G., and Newton, M. I. (2002). Drop evaporation on solid surfaces: constant contact angle mode. *Langmuir*, **18**, 2636–2641.

Fried, E. and Jabbour, M. (2012). Dynamical equations for the contact line of an evaporating or condensing sessile drop. *J. Fluid Mech.*, **703**, 204–237.

Gelderblom, H., Bloemen, O., and Snoeijer, J. H. (2012). Stokes flow near the contact line of an evaporating drop. *J. Fluid Mech.*, **709**, 69–84.

Gladwell, G. M. L. (1980). *Contact problems in the classical theory of elasticity*. Springer Science & Business Media.

Gladwell, G. M. L., Barber, J. R., and Olesiak, Z. (1983). Thermal problems with radiation boundary conditions. *Q. Jl Mech. Appl. Math.*, **36**, 387–401.

Guéna, G., Allançon, P., and Cazabat, A.-M. (2007). Receding contact angle in the situation of complete wetting: Experimental check of a model used for evaporating droplets. *Colloids Surf. A*, **300**, 307–314.

Haut, B. and Colinet, P. (2005). Surface-tension-driven instabilities of a pure liquid layer evaporating into an inert gas. *J. Colloid Interface Sci.*, **285**, 296–305.

Hervet, H. and de Gennes, P.-G. (1984). Dynamique du mouillage: films précurseurs sur solide sec. *C. R. Acad. Sci. Paris*, **299**, 499–503.

Hocking, L. M. (1976). A moving fluid interface on a rough surface. *J. Fluid Mech.*, **76**, 801–817.

Hocking, L. M. (1981). Sliding and spreading of thin two-dimensional drops. *Q. Jl Mech. Appl. Math.*, **34**, 37–55.

Hocking, L. M. (1983). The spreading of a thin drop by gravity and capillarity. *Q. Jl Mech. Appl. Math.*, **36**, 55–69.

Hocking, L. M. (1995). On contact angles in evaporating liquids. *Phys. Fluids*, **7**, 2950–2955.

Hocking, L. M. and Rivers, A. D. (1982). The spreading of a drop by capillary action. *J. Fluid Mech.*, **121**, 425–442.

Hu, H. and Larson, R. G. (2002). Evaporation of a sessile droplet on a substrate. *J. Phys. Chem. B*, **106**, 1334–1344.

Huh, C. and Scriven, L. E. (1971). Hydrodynamic model of steady movement of a solid/liquid/fluid contact line. *J. Colloid Interface Sci.*, **35**, 85–101.

Iwamoto, C. and Tanaka, S.-I. (2002). Atomic morphology and chemical reactions of the reactive wetting front. *Acta Mater.*, **50**, 749–755.

Jackson, J. D. (1975). *Classical Electrodynamics*. Wiley, New York, 2nd edition edition.

Janeček, V., Andreotti, B., Pražák, D., Bárta, T., and Nikolayev, V. S. (2013). Moving contact line of a volatile fluid. *Phys. Rev. E*, **88**, 060404.

Janeček, V., Doumenc, F., Guerrier, B., and Nikolayev, V. S. (2015). Can hydrodynamic contact line paradox be solved by evaporation–condensation? *J. Colloid Interface Sci.*, **460**, 329–338.

King, J. R. (2001). Thin-film flows and high-order degenerate parabolic equations. In *IUTAM Symposium on Free Surface Flows*, pages 7–18. Springer.

Lacey, A. A. (1982). The motion with slip of a thin viscous droplet over a solid surface. *Stud. Appl. Math.*, **67**, 217–230.

Ledesma-Aguilar, R., Vella, D., and Yeomans, J. M. (2014). Lattice-Boltzmann simulations of droplet evaporation. *Soft Matter*, **10**, 8267–8275.

Lide, D. R. (2004). *CRC handbook of chemistry and physics*. CRC press, 85th edition edition.

Margerit, J., Dondlinger, M., and Dauby, P. C. (2005). Improved 1.5-sided model for the weakly nonlinear study of Bénard–Marangoni instabilities in an evaporating liquid layer. *J. Colloid Interface Sci.*, **290**, 220–230.

Morris, S. J. S. (2001). Contact angles for evaporating liquids predicted and compared with existing experiments. *J. Fluid Mech.*, **432**, 1–30.

Murisic, N. and Kondic, L. (2008). Modeling evaporation of sessile drops with moving contact lines. *Phys. Rev. E*, **78**, 065301.

Murisic, N. and Kondic, L. (2011). On evaporation of sessile drops with moving contact lines. *J. Fluid Mech.*, **679**, 219–246.

Myers, T. G. (1998). Thin films with high surface tension. *SIAM Rev.*, **40**, 441–462.

Noble, B. (1958). *Methods based on the Wiener-Hopf technique for the solution of PDEs*. Pergamon Press.

Ockendon, J., Howison, S., Lacey, A., and Movchan, A. (2003). *Applied Partial Differential Equations*. Oxford University Press.

Oliver, J. M., Whiteley, J. P., Saxton, M. A., Vella, D., Zubkov, V. S., and King, J. R. (2015). On contact-line dynamics with mass transfer. *Euro. Jnl of Applied Mathematics*, **26**, 671–719.

Oron, A., Davis, S. H., and Bankoff, S. G. (1997). Long-scale evolution of thin liquid films. *Rev. Mod. Phys.*, **69**, 931–980.

Picknett, R. G. and Bexon, R. (1977). The evaporation of sessile or pendant drops in still air. *J. Colloid Interface Sci.*, **61**, 336–350.

Plawsky, J. L., Ojha, M., Chatterjee, A., and Wayner Jr, P. C. (2008). Review of the effects of surface topography, surface chemistry, and fluid physics on evaporation at the contact line. *Chem. Eng. Comm.*, **196**, 658–696.

Popov, Y. O. (2005). Evaporative deposition patterns: spatial dimensions of the deposit. *Phys. Rev. E*, **71**, 036313.

Poulard, C., Bénichou, O., and Cazabat, A.-M. (2003). Freely receding evaporating droplets. *Langmuir*, **19**, 8828–8834.

Poulard, C., Guéna, G., Cazabat, A.-M., Boudaoud, A., and Ben Amar, M. (2005). Rescaling the dynamics of evaporating drops. *Langmuir*, **21**, 8226–8233.

Preston, E. (1933). On the evaporation and diffusion of volatile materials into an inert gas stream. *Trans. Faraday Soc.*, **29**, 1188–1198.

Prosperetti, A. and Plesset, M. S. (1984). The stability of an evaporating liquid surface. *Phys. Fluids*, **27**, 1590–1602.

Rednikov, A. and Colinet, P. (2013). Singularity-free description of moving contact lines for volatile liquids. *Phys. Rev. E*, **87**, 010401.

Sáenz, P. J., Sefiane, K., Kim, J., Matar, O. K., and Valluri, P. (2015). Evaporation of sessile drops: a three-dimensional approach. *J. Fluid Mech.*, **772**, 705–739.

Savva, N., Rednikov, A., and Colinet, P. (2014). Asymptotic analysis of evaporating droplets. *http://bura.brunel.ac.uk/handle/2438/9469*.

Saxton, M. A., Whiteley, J. P., Vella, D., and Oliver, J. M. (2016c). On thin evaporating drops: when is the d^2-law valid? *J. Fluid Mech.*, **792**, 134–167.

Saxton, M. A., Whiteley, J. P., Vella, D., and Oliver, J. M. (in preparation, 2016b). On the evolution and lifetime of a thin evaporating drop.

Saxton, M. A., Vella, D., Whiteley, J. P., and Oliver, J. M. (under revision, 2016a). Kinetic effects regularize the mass-flux singularity at the contact line of a thin evaporating drop. *J. Engng Maths*.

Sefiane, K., David, S., and Shanahan, M. E. R. (2008). Wetting and evaporation of binary mixture drops. *J. Phys. Chem. B*, **112**, 11317–11323.

Sefiane, K., Wilson, S. K., David, S., Dunn, G. J., and Duffy, B. R. (2009). On the effect of the atmosphere on the evaporation of sessile droplets of water. *Phys. Fluids*, **21**, 062101.

Semenov, S., Trybala, A., Rubio, R. G., Kovalchuk, N., Starov, V., and Velarde, M. G. (2014). Simultaneous spreading and evaporation: Recent developments. *Adv. Colloid Interface Sci.*, **206**, 382–398.

Shahidzadeh-Bonn, N., Rafaï, S., Azouni, A., and Bonn, D. (2006). Evaporating droplets. *J. Fluid Mech.*, **549**, 307–313.

Skinner, L. M. and Sambles, J. R. (1972). The Kelvin equation — a review. *Aerosol Science*, **3**, 199–210.

Snoeijer, J. H. and Andreotti, B. (2013). Moving contact lines: scales, regimes, and dynamical transitions. *Annu. Rev. Fluid Mech.*, **45**, 269–292.

Sodtke, C., Ajaev, V. S., and Stephan, P. (2007). Evaporation of thin liquid droplets on heated surfaces. *Heat Mass Transfer*, **43**, 649–657.

Stauber, J. M., Wilson, S. K., Duffy, B. R., and Sefiane, K. (2014). On the lifetimes of evaporating droplets. *J. Fluid Mech.*, **744**, R2.

Stauber, J. M., Wilson, S. K., Duffy, B. R., and Sefiane, K. (2015). On the lifetimes of evaporating droplets with related initial and receding contact angles. *Phys. Fluids*, **27**, 122101.

Sultan, E., Boudaoud, A., and Ben Amar, M. (2005). Evaporation of a thin film: diffusion of the vapour and Marangoni instabilities. *J. Fluid Mech.*, **543**, 183–202.

Thompson, A. B. (2012). *Surface-tension-driven coalescence*. Ph.d. thesis, University of Nottingham.

Tsoumpas, Y., Dehaeck, S., Rednikov, A., and Colinet, P. (2015). Effect of Marangoni flows on the shape of thin sessile droplets evaporating into air. *Langmuir*, **31**, 13334–13340.

Voinov, O. V. (1976). Hydrodynamics of wetting. *Fluid Dyn.*, **11**, 714–721.

Weber, H. (1873). Ueber die besselschen functionen und ihre anwendung auf die theorie der elektrischen ströme. *J. Reine Angew. Math.*, **75**, 75–105.

Wiley, J. D. and Webster, J. G. (1982). Analysis and control of the current distribution under circular dispersive electrodes. *Biomedical Engineering, IEEE Transactions on*, pages 381–385.